Beam-Helicity Azimuthal Asymmetry measured with the Recoil Detector in Exclusive Electroproduction of Real Photons at HERMES

Inaugural-Dissertation
zur Erlangung des Doktorgrades der Naturwissenschaften
der Justus-Liebig-Universität Gießen
Fachbereich 07
(Mathematik und Informatik, Physik, Geographie)

vorgelegt von

Weilin Yu

aus Shanghai, China

II.Physikalisches Institut der Justus-Liebig-Universität Gießen
July 2009

Dekan: Prof. Dr. Bernd Baumann

1. Berichterstatter: Prof. Dr. M. Düren

2. Berichterstatter: Prof. Dr. A. Müller

Zusammenfassung

Die experimentelle Erforschung der Nukleonstruktur spielt eine wichtige Rolle beim Test der Quantenchromodynamik (QCD). QCD hat sich als erfolgreiche Theorie erwiesen, um die subatomare Welt zu beschreiben, welche aus unterschiedlichen Blickwinkeln von verschiedenen Experimenten betrachtet wird. Die Experimente am HERA Speicherring bei DESY leisteten einen großen Beitrag zum Verständnis der Nukleonstruktur. Sie benutzten dafür die tiefinelastische Streuung (DIS) in der Kollision vom Elektronen/Positronen und Protonen.

Das HERMES Experiment am DESY verwendete den longitudinal polarisierten Elektronen- oder Positronenstrahl mit einer Energie von 27.6 GeV zusammen mit einem polarisierten oder unpolarisierten Gastarget, um die Spinstruktur des Nukleons zu untersuchen. Mitte der 80er Jahre wurde vom EMC Experiment am CERN festgestellt, dass sich nur ein kleiner Teil des Spins des Protons durch die Beiträge der Spins der Quarks erklären lässt. Dies wurde im Allgemeinen als die Spinkrise bezeichnet. Das HERMES Experiment wurde aufgebaut, um dieses Mysterium zu lösen.

Durch die Messung tief-virtueller Comptonstreuung (DVCS) lassen sich die generalisierten Partonverteilungen (GPDs) bestimmen. Diese erlauben eine vereinheitlichte Beschreibung der Nukleonstruktur. Darüber hinaus geben sie im Prinzip einen experimentellen Zugang zu den Bahndrehimpulsen der Quarks. Jedoch ist der DVCS Prozess nicht unterscheidbar vom Bethe-Heitler (BH) Prozess, bei dem das gestreute Elektron durch Bremsstrahlungsprozesse ein reelles Photon erzeugt. Es stellt sich aber heraus, dass die durch diese Ununterscheidbarkeit verursachte Interferenz vom BH und DVCS den Zugang zu DVCS Amplitude bietet. Dies geschieht durch die Messung von Asymmetrien des BH-DVCS-Wirkungsquerschnittes bezüglich der Strahlladung, der Strahlpolarisation, oder der Targetpolarisation.

Das HERMES Spektrometer wurde aufgebaut, um semi-inklusive und inklusive DIS Prozesse zu messen. Deshalb kann das rückgestoßene Proton in exklusiven Prozessen nicht nachgewiesen werden. Bis 2005 wurden indirekte Methoden angewendet, um die Rückstoßprotonen vom Untergrund zu separieren. Allerdings lassen sich mit diesen indirekten Methoden nicht alle Untergrundbeiträge eliminieren, insbesondere nicht der Beitrag von Δ^+-Resonanzen. Um die Verbesserung der Selektion von DVCS-Ereignissen zu erzielen, wurde der HERMES Rückstoßdetektor aufgebaut und 2006 im HERMES Experiment installiert. Das HERMES Vorwärtsspektrometer, zusammen mit dem Rückstoßdetektor, nahm in der Zeit zwischen Mai 2006 und dem Ende des HERA Betriebs im Juni 2007 Daten. Der Detektor besteht aus drei Teildetektoren: einem Silizium-Zähler innerhalb der Streukammer, einem Detektor aus szintillierenden Fasern und einem Photondetektor. Er befand sich im 1 T starken Magnetfeld eines supraleitenden Magneten. Während der Datenaufnahme wurden eine große Anzahl DIS Ereignisse mit dem unpolarisierten Wasserstoff- und Deuterium-Target von HERMES genommen. Die erste Kalibrierung und Rekonstruktion dieser Daten ist erfolgreich abgeschlossen worden.

Die Extraktion der azimutalen Asymmetrien bezüglich der Strahlhelizität aus den Daten von 2007 am Wasserstoff-Target wurden in dieser Arbeit durchgeführt. Die extrahierten Asymmetrieamplituden vom elastischen BH/DVCS Prozess stimmen gut mit den früheren Messungen von HERMES überein. Außerdem wurde zum ersten Mal die Asymmetrie von Δ^+-Resonanzen extrahiert, jedoch sind die Ereignisse aufgrund der geringen Statistik mit großen Unsicherheiten behaftet.

Contents

Chapter 1

Introduction

The experimental exploration of the nucleon structure plays a very important role to test the quantum chromodynamics (QCD). From different angles through various types of experiments [1] the QCD has been proven to well describe the subatomic world. The experiments from HERA collider at DESY have made significant contributions to understand the nucleon structure by using its e^+/e^- and proton beams to perform the Deeply Inelastic Scattering (DIS) experiments [2].

As one of the experiments from HERA, the HERMES experiment [3, 4] used the longitudinally polarized lepton (electron or positron) beam together with the polarized or unpolarized gas targets to study the nucleon spin structure. It was found in the EMC experiment at CERN in the middle of 1980s that only a small part of the proton spin is carried by the quarks, which was called the "spin-crisis" [5, 6]. The HERMES experiment was established to resolve this problem.

The nucleon spin can be decomposed into different contributions as [7, 8, 9, 10]

$$\frac{1}{2} = \frac{1}{2}\Delta\Sigma + L_z^q + \Delta G + L_z^g, \tag{1.1}$$

where $\Delta\Sigma$ (ΔG) denotes the contribution from quarks (gluons), L_z^q (L_z^g) indicates the contribution from the orbital angular momenta of quarks (gluons).

In the HERMES and the other experiments, the $\Delta\Sigma$ and ΔG have been well studied through the inclusive and semi-inclusive DIS measurements [11, 12, 13, 14, 15, 16, 17, 18, 19, 20, 21, 22]. It was found that a large fraction of the nucleon spin can not be explained by these two parts. Meanwhile the Generalized Parton Distributions (GPDs) can also be measured [21] through the exclusive hard processes. GPDs offer a possibility to determine the orbital angular momenta of quarks, and can be accessed by studying the Deeply Virtual Compton Scattering (DVCS) [23]. In the exclusive reaction $ep \rightarrow e^{'}\gamma p$, the DVCS process interferes with the Bethe-Heitler (BH) process where the incoming or outgoing electron/positron radiates a hard real photon in the coulomb field of the nucleon. This interference leads to measurable cross-section azimuthal asymmetries with respect to

beam helicity, beam charge, and target polarization. These different types of the azimuthal asymmetries give access to the different terms of the GPDs.

At HERMES DVCS processes were measured [24,25,26] previously by its forward spectrometer, however, the recoil protons could not be directly detected due to the acceptance of the spectrometer. Thus, the missing mass method was used to select the exclusive reactions. This method is limited by the resolutions of the detectors and the incapability to clean up the background from the semi-inclusive DIS process and the associated BH process $ep \rightarrow e^{'}\gamma\Delta^{+}$. The associated BH process has a contribution of around 12% to the final exclusive data sample, and its effect to the azimuthal asymmetries is unknown.

A Recoil Detector [27,28,29] was built and installed at the beginning of 2006 to upgrade the HERMES forward spectrometer to measure the recoil protons. The Recoil Detector consists of three main sub-detectors: a silicon strip detector surrounding the target cell inside the beam vacuum in a scattering chamber, a scintillating fibre tracker, and a photon detector consisting of three layers of tungsten and scintillator bars. A large amount of data was collected with the Recoil Detector on unpolarized proton and deuteron targets in the years 2006-2007 by using the high intensity e^{+}/e^{-} beams from HERA. The detectors have been commissioned over the last years, the first detector calibrations, the tracking reconstructions have also been accomplished for a first physics analysis.

The azimuthal asymmetries with respect to the beam helicity were extracted on the proton target from the data taken with the positron beam in 2007. The asymmetries from the elastic BH/DVCS process have been extracted with and without using the detected recoil proton information by the Recoil Detector. In addition, a small sample of associated BH process was collected via detecting the π^{+} as a tag particle of the decay channel $\Delta^{+} \rightarrow n\pi^{+}$. A first beam helicity asymmetry has been extracted based on this data sample.

Chapter 2

GPDs and DVCS

Generalized Parton Distributions (GPDs), also called Off-Forward Parton Distributions [23] or Nonforward Parton Distributions [30], provide a way to access the total angular momenta of partons in the nucleon and have been intensively studied over the last years [31,32,33,34]. Deeply Virtual Compton Scattering (DVCS) is the most direct exclusive process to access GPDs [23] via the experimental measurements of the different azimuthal cross-section asymmetries of the DVCS and Bethe-Heitler (BH) interference term. In this chapter, we will first give a brief introduction of the definitions, properties and parameterizations of the GPDs. In the second part, we will focus on the DVCS and its experimental observable - azimuthal asymmetries.

2.1 The Definitions of GPDs

Figure 2.1 shows the diagram of the hard exclusive processes

$$\gamma^*(q) + T(p) \rightarrow \gamma(q^{'}) + T^{'}(p^{'}), \quad \gamma^*(q) + T(p) \rightarrow M(q^{'}) + T^{'}(p^{'}), \tag{2.1}$$

in which a virtual photon γ^* scatters off the hadronic target T and produces a real photon γ or a meson M, and a recoil state $T^{'}$. It has been proven that such kind of reactions at high energy and large virtuality can be factorized into a perturbative and a non-perturbative parts [35, 36, 37, 38]. The perturbative part (upper part in Fig. 2.1), corresponding to the interaction of a parton with a virtual photon, can be well calculated in perturbative QCD. The non-perturbative part (lower part in Fig. 2.1), corresponding to the interaction of the scattered parton and the target nucleon, can not yet be calculated from first principles. It has been found that GPDs can be used to describe this part of the reactions.

To maintain gauge invariance, the GPDs as described in the following parts are built based on the light-cone framework where the target nucleon moves towards the positive z-direction and the virtual photon moves towards the negative z-direction. The non-perturbative part of the exclusive amplitude can be parameterized by unpolarized GPDs

$H(x,\xi,t)$ and $E(x,\xi,t)$, polarized GPDs $\tilde{H}(x,\xi,t)$ and $\tilde{E}(x,\xi,t)$ when the partons do not flip helicity, and by $H_T(x,\xi,t)$, $E_T(x,\xi,t)$, $\tilde{H}_T(x,\xi,t)$ and $\tilde{E}_T(x,\xi,t)$ when the parton helicity flips [33]. They are defined through the off-forward matrix elements, as distinguished from the forward ones in inclusive reactions, of certain non-local quark and gluon composite operators. The momentum fraction x is defined in the light-cone coordinate by $k^+ = x\bar{P}^+$, where k is the quark loop momentum and $\bar{P}^+$ is the component of the average nucleon four-momentum from the initial p and final p' along the light-cone, $\bar{P}$ can be defined via $\bar{P} = (p+p')/2$. The skewedness variable ξ is defined from $\Delta^+ = -2\xi\bar{P}^+$, where $\Delta = p' - p$ is the overall momentum transfer to the target nucleon. The Mandelstam invariant t is defined as the total squared momentum transfer $t = \Delta^2$.

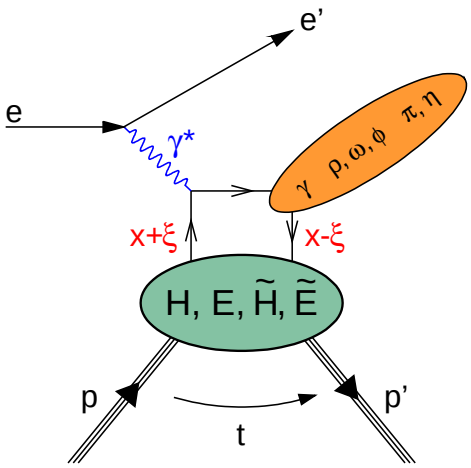

Figure 2.1: The "handbag" diagrams for hard exclusive processes with a real photon or a meson in the final state.

The variables x and ξ can not be directly measured from the experiments. The variable x is restricted from -1 to 1 and has a different meaning from the normal Bjorken variable x_B, however in the limit of $|t| << Q^2$ the skewedness variable ξ becomes close to $\frac{x_B}{2-x_B}$. When $x > \xi$ ($x < -\xi$) the lower part of Fig. 2.1 can be interpreted as the amplitude for taking a parton of longitudinal momentum fraction $x+\xi$ out of the nucleon, changing the fraction to $x-\xi$ and then putting the parton back to the nucleon. When $-\xi < x < \xi$ it indicates the amplitude for taking out a quark-antiquark pair with four-momentum $-\Delta$.

2.2 The Properties of GPDs

GPDs have been proven to access the angular momentum of the quarks by the second Mellin moments [23]:

$$\lim_{t\to 0}\int_{-1}^{1} dx\ x(H^q(x,\xi)+E^q(x,\xi)) \ = \ 2J^q, \tag{2.2}$$

where J^q is the fraction of the nucleon angular momentum carried by a quark. This relation is also called Ji relation and holds for both types of partons, quarks and gluons. The Ji relation reveals the possibility to understand the composition of the nucleon spin from the quarks. As the total angular momenta of a certain quark flavor can be decomposed into its intrinsic spin and orbital angular momentum, while the intrinsic quark spin have been well measured through the inclusive semi-inclusive DIS processes [22], measuring the total angular momenta then provides a way to understand the contribution of the orbital angular momenta of quarks to the nucleon spin.

The correlation between the Ji relation and the nucleon spin structure has inspired a lot of interest to study GPDs and their properties. In the forward direction ($\Delta \to 0$), GPDs H reduces to the ordinary spin independent quark distribution $q(x)$ and $\tilde{H}$ reduces to the spin dependent density $\Delta q(x)$,

$$\begin{aligned} H^q(x,0,0) &= q(x), & \tilde{H}^q(x,0,0) &= \Delta q(x), & for\ x>0;\\ H^q(x,0,0) &= -\bar{q}(-x), & \tilde{H}^q(x,0,0) &= \Delta\bar{q}(-x), & for\ x<0. \end{aligned} \tag{2.3}$$

The GPDs also have an interesting link to the nucleon form factors: by integrating the quark GPDs over x, i.e. calculating the first moments of the GPDs, the form factors are obtained [23],

$$\begin{aligned} \int_{-1}^{1} dx H^q(x,\xi,t) &= F_1^q(t), & \int_{-1}^{1} dx E^q(x,\xi,t) &= F_2^q(t),\\ \int_{-1}^{1} dx \tilde{H}^q(x,\xi,t) &= g_A^q(t), & \int_{-1}^{1} dx \tilde{E}^q(x,\xi,t) &= g_P^q(t), \end{aligned} \tag{2.4}$$

where $F_1^q(t)$ and $F_2^q(t)$ are the Dirac and Pauli form factors, $g_A^q(t)$ and $g_P^q(t)$ are the axial and pseudo-scalar ones. They are defined for each separate quark flavor separately. The conventional nucleon form factors $F_1(t)$, $F_2(t)$, $g_A(t)$ and $g_P(t)$ are composed from the sum of the flavor dependent form factors.

One of the non-trivial properties of the GPDs is the polynomiality of their Mellin moments which follows the Lorentz invariance of nucleon matrix elements [23].

$$\begin{aligned} \int_{-1}^{1} dx x^N H^q(x,\xi) &= h_0^{q(N)} + h_2^{q(N)}\xi^2 + ... + h_{N+1}^{q(N)}\xi^{N+1},\\ \int_{-1}^{1} dx x^N E^q(x,\xi) &= e_0^{q(N)} + e_2^{q(N)}\xi^2 + ... + e_{N+1}^{q(N)}\xi^{N+1}. \end{aligned} \tag{2.5}$$

The coefficients in front of the highest power of ξ for the singlet functions H^q and E^q are found to be related to each other

$$e^{q(N)}_{N+1} = -h^{q(N)}_{N+1}. \tag{2.6}$$

2.3 The Parameterizations of GPDs

As mentioned before, the GPDs can not be calculated from the first principles in QCD yet, they can only be parameterized by certain models with the constraints from the properties listed previously. These model dependent predictions provide an important testing ground for the experimental explorations, the results of the experimental tests in reverse will then help to understand the models and their physical meaning. Calculations of GPDs have been performed in the bag model [39], chiral soliton model [40], constituent quark model [41] and the lattice QCD [42, 43]. In this section we will introduce a popular parameterization for GPDs based on the chiral soliton model, which has been widely tested in experiments [32, 44, 45].

To satisfy the polynomial conditions the GPDs were parameterized with so-called double distributions [46], while the functions $F^q(\beta,\alpha)$ and $K^q(\beta,\alpha)$ have been used to construct $H^q(x,\xi)$ and $E^q(x,\xi)$ separately [32, 47, 48],

$$\begin{aligned} H^q_{DD}(x,\xi) &= \int_{-1}^{1} d\beta \int_{-1+|\beta|}^{1-|\beta|} d\alpha \delta(x-\beta-\alpha\xi) F^q(\beta,\alpha), \\ E^q_{DD}(x,\xi) &= \int_{-1}^{1} d\beta \int_{-1+|\beta|}^{1-|\beta|} d\alpha \delta(x-\beta-\alpha\xi) K^q(\beta,\alpha). \end{aligned} \tag{2.7}$$

$F^q(\beta,\alpha)$ and $K^q(\beta,\alpha)$ can be further parameterized as [49]

$$F^q(\beta,\alpha) = h(\beta,\alpha) q(\beta), \tag{2.8}$$

and

$$K^q(\beta,\alpha) = h(\beta,\alpha) e^q(\beta), \tag{2.9}$$

where $h(\beta,\alpha)$ denotes a profile function and can be described through the following one-parameter ansatz:

$$h(\beta,\alpha) = \frac{(2b+2)!}{2^{2b+1}((b+1)!)^2} \frac{[(1-|\beta|)^2-\alpha^2]^b}{(1-|\beta|)^{2b+1}}, \tag{2.10}$$

where the parameter b characterizes the strength of the ξ dependence of the GPD. The GPDs are independent of ξ in the limit of $t \to \infty$. b is a free parameter for the valance quarks and the sea quarks and can be used as a fit parameter for the extraction of GPDs from a hard electro-production observable.

In Eq. (2.8), $q(\beta)$ is the ordinary quark distribution for the quark flavor q which meets the forward limit requirement in Eq. (2.3), i.e. $H^u(x,0) = u(x), H^d(x,0) = d(x), H^s(x,0) = s(x)$. While in Eq. (2.9), $e^q(\beta)$ denotes spin-flip quark distributions which are unknown from the inclusive DIS data, and can be parameterized in the chiral quark-soliton model as [32]

$$e^q(x) = A^q \cdot q_{val}(x) + B^q \cdot \delta(x), \tag{2.11}$$

where the $e^q(x)$ represents the contribution by a sum of valence ($q_{val}(x)$ term) and sea quarks ($\delta(x)$ term). The δ function is used here as the sea quark component of $e(x)$ being a very narrowly peaked function around $x = 0$. The coefficients A^q and B^q are related to the total angular momentum J_q of quark flavor q which hence could be used to study the sensitivity of the hard electro-production observable on J_q.

Although the GPDs deduced from the double distributions in Eq. (2.7) satisfy the polynomiality conditions, they are found to lead to $h^{q(N)}_{N+1} = e^{q(N)}_{N+1} = 0$, which is of course not meaningful in physics. To avoid this, an additional D-term was suggested to put in Eq. (2.7) to complete the parameterization [50]. The modified GPDs are then as following [32]:

$$\begin{aligned} H^q_{DD}(x,\xi) &= \int_{-1}^{1} d\beta \int_{-1+|\beta|}^{1-|\beta|} d\alpha \delta(x-\beta-\alpha\xi) F^q(\beta,\alpha) + \theta[1-\frac{x^2}{\xi^2}] D^q(\frac{x}{\xi}), \\ E^q_{DD}(x,\xi) &= \int_{-1}^{1} d\beta \int_{-1+|\beta|}^{1-|\beta|} d\alpha \delta(x-\beta-\alpha\xi) K^q(\beta,\alpha) - \theta[1-\frac{x^2}{\xi^2}] D^q(\frac{x}{\xi}). \end{aligned} \tag{2.12}$$

Here $D^q(z)$ is an odd function with $-1 \leq z \leq 1$ and can be decomposed into a Gegenbauer series,

$$D(z) = (1-z^2)[d_1 C_1^{\frac{3}{2}}(z) + d_3 C_3^{\frac{3}{2}}(z) + d_5 C_5^{\frac{3}{2}}(z) + ...]. \tag{2.13}$$

Following the Eq. (2.6) this term from $H^q(x,\xi)$ and $E^q(x,\xi)$ has the same absolute value but with the opposite sign.

So far the GPDs have only been discussed for the t-independent part without involving the t-dependent part. The t-dependence is essential for the Ji relation and can mainly be constrained by the first moments in Eq. (2.4) and be simply expressed [32] as

$$H^q(x,\xi,t) = H^q(x,\xi) \cdot F_1^q(t), \tag{2.14}$$

and

$$E^q(x,\xi,t) = E^q(x,\xi) \cdot F_2^q(t)/\kappa^q, \tag{2.15}$$

where F_1^q and F_2^q denote the ordinary nucleon form factors and κ^q is the anomalous magnetic moment of the nucleon assigned to the quark flavor q.

2.4 The Kinematic Definitions of DVCS

DVCS is the exclusive photo-production of a real photon, i.e. $\gamma^* N \rightarrow \gamma N^*$. It is theoretically the cleanest channel to study GPDs, however, experimentally it is impossible to distinguish the DVCS process from the elastic Bethe-Heitler (BH) process, as both processes have the same initial and final states. In Fig. 2.2 it can be seen that DVCS generates the real photon by the interaction of a quark inside the nucleon while the BH process emits the real photon by the incoming or outgoing electron. Over the kinematics of the HERMES experiment, the cross-section of BH process dominates the one of DVCS. For this reason DVCS is measured via the azimuthal asymmetries with respect to beam helicity, beam charge, and target spin [51] instead of the direct measurement of its cross-section. In this section we will first introduce the related kinematic variables for the BH/DVCS processes, then we will try to deduce the series of azimuthal asymmetries from the interference term of BH and DVCS.

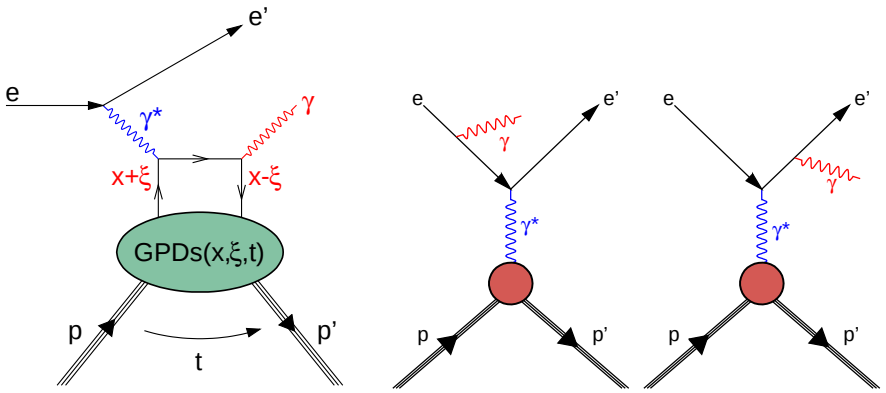

Figure 2.2: (a) Diagram for Deeply Virtual Compton Scattering; (b) Diagrams for the Bethe-Heithler processes.

In order to describe the BH/DVCS processes, the terminologies k (k'), P (P') and q' are introduced to denote the four-momenta of the initial (final) leptons and target protons and the real photon respectively, see Fig. 2.2 and Fig. 2.3. The energy of the virtual photon can be calculated from the energy of the initial and final lepton E (E') as $\nu = E - E'$ in the target rest frame, and its four-momentum q, the photon virtuality Q^2, and the Bjorken variable x_B are defined as

$$Q^2 = -q^2 = -(k - k')^2, \tag{2.16}$$

$$x_B = \frac{Q^2}{2Pq}. \tag{2.17}$$

In the laboratory frame they are calculated as

$$Q^2 = 4EE_e \sin^2(\frac{\theta_e}{2}), \tag{2.18}$$

$$x_B = \frac{Q^2}{2m_P\nu}, \tag{2.19}$$

where θ_e is the lepton scattering polar angle, m_P is the proton mass. The fraction of the beam energy carried by the virtual photon can be represented as

$$y = \frac{\nu}{E}. \tag{2.20}$$

While the invariant mass of the system of virtual photon and target proton is given by

$$W^2 = (p+q)^2 = m_P^2 + 2m_P\nu - Q^2. \tag{2.21}$$

The invariant momentum transfer from initial to final target proton, defined as

$$t = (P - P')^2. \tag{2.22}$$

When the recoil proton is not directly detected, it can be calculated either using the photon energy E_γ:

$$t = -Q^2 - 2E_\gamma(\nu - \sqrt{\nu^2 + Q^2}\cos\theta_{\gamma\gamma^*}), \tag{2.23}$$

or when the recoil proton is in the ground state, it can be calculated without using the photon energy E_γ, the so-called 'constrained' t:

$$t_c = \frac{-Q^2 - 2\nu(\nu - \sqrt{\nu^2 + Q^2}\cos\theta_{\gamma\gamma^*})}{1 + \frac{1}{m_P}(\nu - \sqrt{\nu^2 + Q^2}\cos\theta_{\gamma\gamma^*})}. \tag{2.24}$$

Here $\theta_{\gamma\gamma^*}$ is the angle between the virtual photon and the real photon

$$\theta_{\gamma\gamma^*} = \arccos\frac{\vec{q}\cdot\vec{q'}}{|\vec{q}||\vec{q'}|}. \tag{2.25}$$

2.5 The Azimuthal Asymmetries

The angular-dependent cross section of the hard exclusive production of a real photon can be expressed in a four-fold differential format for the unpolarized proton target [51],

$$\frac{d\sigma}{dx_B dy d|\Delta^2| d\phi} = \frac{\alpha^3 x_B y}{16\pi^2 Q^2\sqrt{1 + 4x_B^2 m_N^2/Q^2}} \cdot |\frac{\mathcal{T}}{e^3}|^2, \tag{2.26}$$

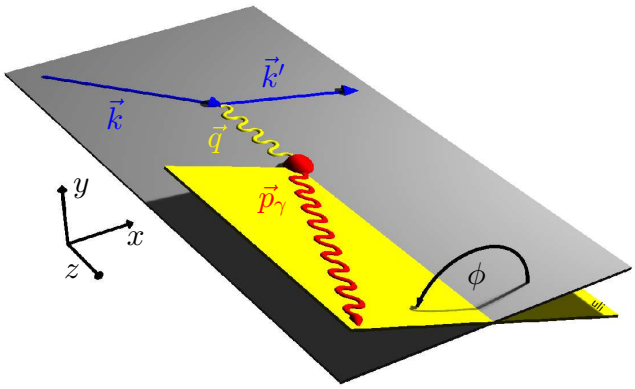

Figure 2.3: Kinematics of real photon production in the target rest frame. The z direction is chosen along the momentum of the virtual photon.

where α denotes the fine-structure constant, e the lepton charge magnitude, the azimuthal angle ϕ is defined for the angle between the lepton scattering plane and the photon production plane from Fig. 2.3. The amplitude $\mathcal{T}$ is the coherent sum of the DVCS amplitude $\mathcal{T}_{DVCS}$ and the BH amplitude $\mathcal{T}_{BH}$,

$$|\mathcal{T}|^2 = |\mathcal{T}_{BH}|^2 + |\mathcal{T}_{DVCS}|^2 + \mathcal{T}_{BH}\mathcal{T}^*_{DVCS} + \mathcal{T}^*_{BH}\mathcal{T}_{DVCS}, \tag{2.27}$$

where $\mathcal{T}_{BH}\mathcal{T}^*_{DVCS} + \mathcal{T}^*_{BH}\mathcal{T}_{DVCS}$ denotes the amplitude of the interference term between the DVCS and BH processes.

The squared amplitudes of DVCS and BH process, and the interference term can be written as

$$|\mathcal{T}_{BH}|^2 = \frac{e^6}{x_B^2 y^2 (1+\epsilon^2)^2 \Delta^2 \mathcal{P}_1(\phi)\mathcal{P}_2(\phi)}\{c_0^{BH} + \sum_{n=1}^{2} c_n^{BH} cos(n\phi) + s_1^{BH} sin(\phi)\}, \tag{2.28}$$

$$|\mathcal{T}_{DVCS}|^2 = \frac{e^6}{y^2 Q^2}\{c_0^{DVCS} + \sum_{n=1}^{2}[c_n^{DVCS} cos(n\phi) + \lambda s_n^{DVCS} sin(n\phi)]\}, \tag{2.29}$$

$$\mathcal{I} = \frac{\pm e^6}{x_B y^3 \mathcal{P}_1(\phi)\mathcal{P}_2(\phi)\Delta^2}\{c_0^I + \sum_{n=1}^{3}[c_n^{\mathcal{I}} cos(n\phi) + \lambda s_n^{\mathcal{I}} sin(n\phi)]\}, \tag{2.30}$$

where the + (-) sign in the interference term corresponds to the negatively (positively) charged lepton beam while λ represents the beam helicity. The symbol ϵ stands for the following expression:

$$\epsilon = 2x_B \frac{M}{Q}. \tag{2.31}$$

The lepton beam propagators $\mathcal{P}_1(\phi)$ and $\mathcal{P}_2(\phi)$ can be parameterized as

$$\mathcal{P}_1 = -\frac{1}{y(1+\epsilon^2)}\{J + 2K cos(\phi)\}, \quad \mathcal{P}_2 = \frac{1}{y(1+\epsilon^2)}\{1 + J + \frac{\Delta^2}{Q^2} + 2K cos(\phi)\}, \tag{2.32}$$

where the parameter J is defined as

$$J = (1 - y - \frac{y\epsilon^2}{2})(1 + \frac{\Delta^2}{Q^2}) - (1 - x)(2 - y)\frac{\Delta^2}{Q^2}. \tag{2.33}$$

The $1/Q$-power suppressed kinematical factor K appearing here can be expressed as

$$K^2 = -\frac{\Delta^2}{Q^2}(1 - x_B)(1 - y - \frac{y^2\epsilon^2}{4})(1 - \frac{\Delta^2_{min}}{\Delta^2})\{\sqrt{1 + \epsilon^2} + \frac{4x_B(1 - x_B) + \epsilon^2}{4(1 - x_B)}\frac{\Delta^2 - \Delta^2_{min}}{Q^2}\}. \tag{2.34}$$

The kinematical factor K is proportional to $\sqrt{-t}/Q$. The s_1^I and c_1^I are the two leading Fourier coefficients related to the quark-helicity-conserving twist-2 GPDs, the others are either kinematically suppressed by the factor of K or related to twist-3 GPDs.

To understand how GPDs enter the azimuthal asymmetries of the experiments, a set of Compton form factors (CFFs) is introduced. In leading twist the CFFs are given by a convolution of perturbatively calculable coefficient functions $\mathcal{C}^{(\pm)}$ and the four GPDs via

$$\begin{aligned} \{\mathcal{H}, \mathcal{E}\}(\xi) &= \int_{-1}^{1} dx \mathcal{C}^{(-)}(\xi, x)\{H, E\}(x, \eta)_{|\eta=-\xi}, \\ \{\tilde{\mathcal{H}}, \tilde{\mathcal{E}}\}(\xi) &= \int_{-1}^{1} dx \mathcal{C}^{(+)}(\xi, x)\{\tilde{H}, \tilde{E}\}(x, \eta)_{|\eta=-\xi}. \end{aligned} \tag{2.35}$$

For simplicity the summation on the right-hand side of the above equations over the quark species:

$$\mathcal{C}^{(\pm)}GPD \rightarrow \sum_{i=u,d,s} \mathcal{C}_i^{(\pm)}GPD_i. \tag{2.36}$$

Furthermore the CFFs are composed of a real part and an imaginary part. They can be generally parameterized.

With respect to beam helicity, beam charge, and target polarization there are several correlated azimuthal asymmetries, which have been studied both theoretically [32] and experimentally [24, 25, 26, 52]. Two of them related to this work will be briefly introduced in the following section.

2.5.1 Beam-Helicity Asymmetry

The Beam-Helicity Asymmetry is an asymmetry measured by using a longitudinally polarized lepton beam and an unpolarized target with respect to the positive and negative beam helicity. The name of Beam-Spin Asymmetry (BSA) was widely used in the community for the Beam-Helicity Asymmetry both in theoretical and experimental articles, in this work

the name of BSA will be used as the abbreviation for Beam-Helicity Asymmetry. The BSA can be calculated as

$$A_{LU}(\phi) = \frac{d\sigma^{\rightarrow}(\phi) - d\sigma^{\leftarrow}(\phi)}{d\sigma^{\rightarrow}(\phi) + d\sigma^{\leftarrow}(\phi)}, \tag{2.37}$$

where $\rightarrow$ and $\leftarrow$ stand for the positive and negative beam helicity. Its azimuthal dependence is approximately given by the $\sin(\phi)$ function

$$A_{LU}(\phi) \propto s_1^I \cdot \sin(\phi) \propto Im\{F_1\mathcal{H} + \frac{x_B}{2-x_B}(F_1+F_2)\tilde{\mathcal{H}} - \frac{\Delta^2}{4M^2}F_2\mathcal{E}\}\sin(\phi). \tag{2.38}$$

The imaginary part of $\mathcal{H}$ dominates the contribution in the small x_B region.

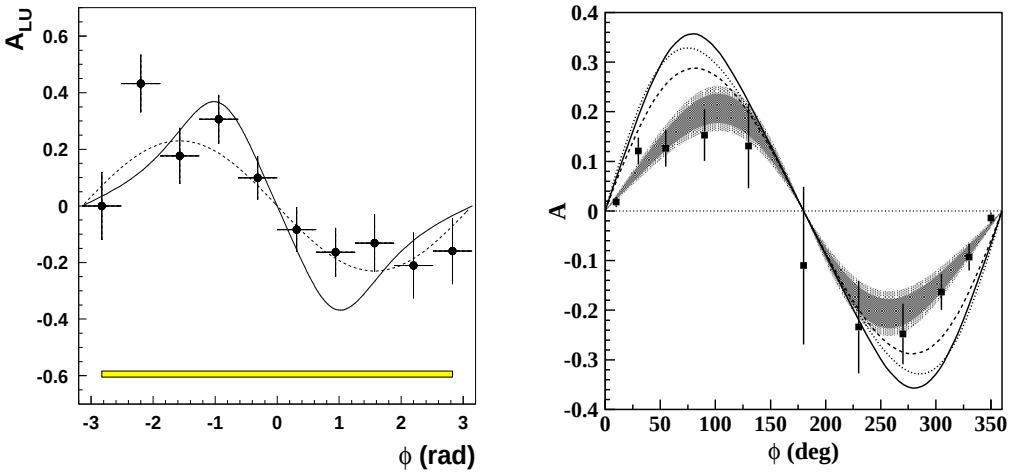

(a) (b)

Figure 2.4: Beam-Helicity Asymmetry A_{LU} on the proton target measured at HERMES (panel a) and CLAS (panel b). In the panel a: the dashed curve represents a $\sin\phi$ dependence with an amplitude of 0.23 from data, while the solid curve represents the result of a model calculation. The error band below shows the systematic uncertainty. In the panel b: the shaded regions represent the ranges of the fitted function $\alpha \sin\phi + \beta \sin(2\phi)$, while the curves represent model calculations. The dashed (dotted) curve is a calculation with ξ-independent (ξ-dependent) GPDs at leading-twist. The solid curve includes twist-three effects.

The BSA has been measured for the first time in the HERMES [24] and CLAS [52] experiments off proton targets, (see Fig. 2.4). The published value of the $A_{LU}^{\sin\phi}$ amplitude from HERMES is $-0.23 \pm 0.04(stat) \pm 0.03(sys)$ at the average kinematics $<x_B>$=0.11, <-t> = 0.27 GeV^2, $<Q^2>$=2.6 GeV^2. While the $A_{LU}^{\sin\phi}$ amplitude measured at CLAS is $-0.202 \pm 0.028(stat) \pm 0.013(sys)$ at the average kinematics $<x_B>$=0.19, <-t> = 0.19 GeV^2, $<Q^2>$=1.25 GeV^2.

2.5.2 Beam-Charge Asymmetry

The Beam-Charge Asymmetry (BCA) is measured by using unpolarized lepton beam and an unpolarized target with different beam charges, i.e.,

$$A_C(\phi) = \frac{d\sigma(e^+,\phi) - d\sigma(e^-,\phi)}{d\sigma(e^+,\phi) + d\sigma(e^-,\phi)}, \tag{2.39}$$

where the sign + and - indicate the positron and electron beam respectively. This azimuthal dependence is approximately given by the cos(ϕ) function and is proportional to the real part of the CFF $\mathcal{H}$

$$A_C(\phi) \propto c_1^I \cdot cos\phi \propto F_1 \cdot R\mathcal{H} \cdot cos\phi. \tag{2.40}$$

The HERMES experiment was the first experiment to measure the BCA [25] at the proton target with respect to the electron and positron beam. (see Fig. 2.5).

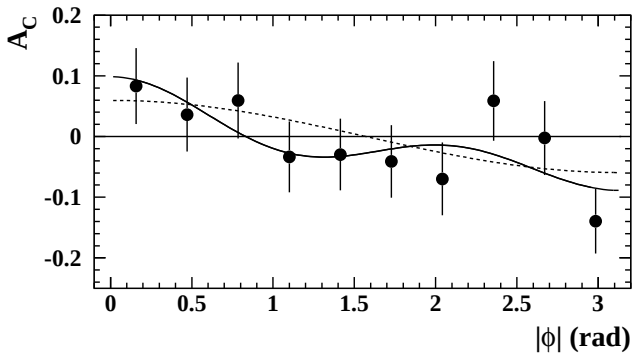

Figure 2.5: Beam-Charge Asymmetry A_C on the proton target measured at HERMES. Statistical uncertainties are shown as the error bars. The solid curve shows the result of a four-parameter fit: (-0.011±0.019) + (0.060±0,027)cosϕ + (0.016±0.026)cos2ϕ + (0.034±0.027)cos3ϕ. The dashed line shows the pure cosϕ dependence.

When the unpolarized lepton beam is used to scatter off a longitudinally polarized or transversely polarized target, the Longitudinal Target-Spin Asymmetry (LTSA) or the Transverse Target-Spin Asymmetry (TTSA) can be measured. The LTSA can access the imaginary part of the CFF $\tilde{\mathcal{H}}$ while the TTSA can access the CFF $\mathcal{E}$, which is essential for the Ji relation. At HERMES the TTSA asymmetries have been extracted from the transversely polarized target for the first time, which can then provide model dependent constraints for total angular momentum from the u quark J_u and the d quark J_d [26].

Chapter 3

The HERMES Experiment

The HERMES experiment was located at DESY (Deutsches Elektronen-Synchrotron), Hamburg. It was one of the four experiments running at HERA (Hadron-Elektron-Ring-Anlage) storage ring. It used the 27.6 GeV longitudinal polarised lepton (electron or positron) beam from HERA and a polarised or unpolarised gas target internal to the storage ring. The HERMES experiment was designed to study semi-inclusive processes involving the detection of hadrons in coincidence with the scattered lepton to explore the nucleon spin structure. However, it is also possible to study exclusive processes with the HERMES detector. The HERMES experiment took data starting in 1995 until the end of HERA running in the middle of 2007. The HERMES has made a significant contribution to the understanding of the nucleon spin structure over the last years with its precise data and various physics programs [3, 4, 21].

3.1 The HERA Collider

HERA was the high energy lepton-proton collider at the DESY research center in Hamburg with a circumference of 6.3 km. The leptons can be accelerated to an energy of 27.6 GeV/c and the protons to an energy of 920 GeV/c separately in two storage rings with the opposite beam directions. The two beams are brought into collision at the north and south points of the ring, where the high energy experiments H1 and ZEUS were located for studying the nucleon structure in deep inelastic scattering. The HERMES experiment is a fixed target experiment using only the lepton beam at the east section of HERA. Figure 3.1 shows the layout of HERA in 2002.

The lepton beam passes through and is accelerated in a set of pre-accelerators before it enters the HERA ring. Up to 220 bunches of the leptons with an energy of 12 GeV/c and beam current of approximately 45 mA are injected into the HERA accelerator. They are separated by a time interval of 96 ns and accelerated to the energy of 27.6 GeV. The beam current decreases exponentially with a life time of typically 8-12 hours down to about 10

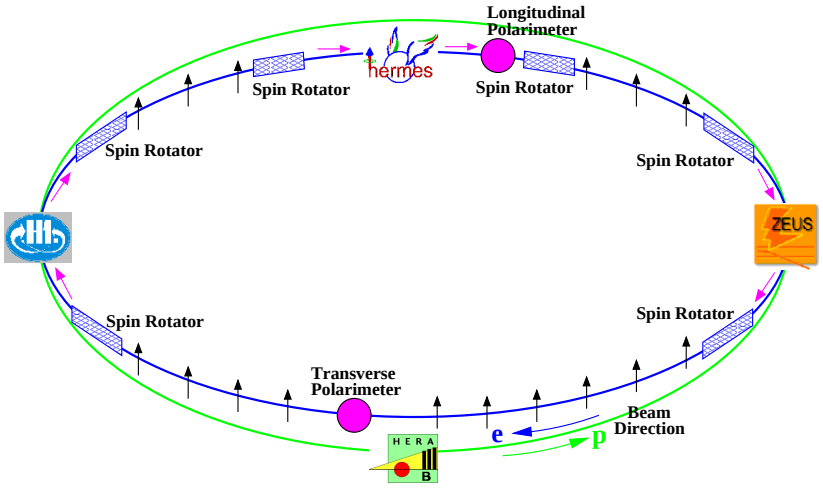

Figure 3.1: Schematic layout of the HERA storage ring from year 2002.

mA, then the beam is dumped and a new beam is refilled. When the beam current reaches 15 mA at the end of the fill, the HERMES is allowed to inject a higher gas density into the target cell to increase the HERMES luminosity. This will reduce the beam life time to 1-2 hours.

For the HERMES experiment it was essential to have a polarized lepton beam. A small asymmetry in spin-flip amplitudes from the emission of synchrotron radiation of charged particles enhances the population of the spin state antiparallel to the direction of the magnetic field, which builds up the transversely self-polarized lepton beam in the storage ring. This is called Sokolov-Ternov-effect and can be described theoretically [54] as

$$P(t) = \frac{8}{5\sqrt{3}}(1 - e^{\frac{-t}{\tau_{ST}}}), \tag{3.1}$$

where τ_{ST} is the rise-time given by

$$\tau_{ST} = \frac{8}{5\sqrt{3}} \frac{2\pi m_e \rho^3}{r_e h \gamma^5} \tag{3.2}$$

with r_e being the classical electron radius and ρ being the bending radius in the magnetic field. At HERA, the $\rho = 707$ m and $\gamma = E/m_e = 53800$, the theoretical rise-time is about 25 minutes. The theoretical self-polarization of the lepton beam can be up to 92.4%. Due to the interaction with the proton beam and other depolarizing effects, the lepton beam polarization obtained in the HERA is much lower.

The physics programs at HERMES require a longitudinally polarized beam. The transverse polarization has to be rotated to the longitudinal direction in front of the experiment area. This is achieved by a spin rotator consisting of interleaved horizontal and vertical

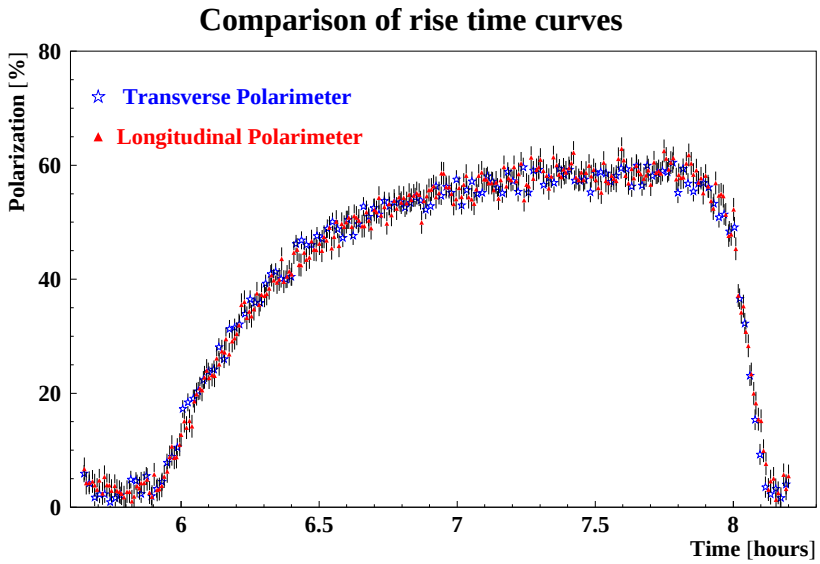

Figure 3.2: Beam polarizations measured by the transverse and longitudinal polarimeters.

bending magnets. A pair of spin rotators was installed up- and down- stream of the interaction point of the HERMES experiment. The upstream spin rotator rotates the direction of the polarization into the beam direction, whereas the downstream rotator reverses the polarization back to the transverse direction.

The lepton beam polarization is continuously measured by two polarimeters [55], the longitudinal polarimeter (LPOL) located close to the HERA east hall and the transverse polarimeter (TPOL) located in the west. Both polarimeters use Compton scattering as an underlying principle to measure the polarization. The LPOL measures the integrated energy asymmetry between Compton photons from left and right circularly polarized laser photons. While the TPOL measures the small transverse spatial asymmetry between the Compton photons from left and right circularly polarized laser photons. Fig. 3.2 shows the beam polarization values measured by the TPOL and LPOL. A rise time around 40 minutes can be seen in the figure and the results of the two polarimeters overlap, confirming the good performance of the polarization measurements.

3.2 The HERMES Forward Spectrometer

The HERMES forward spectrometer was operated from 1995 until the end of HERA operation. It is a forward angle instrument of conventional design to measure the DIS scattering leptons and the total hadronic final state in a wide kinematic range. A dipole magnet with an integrated field of 1.3 Tm is used to bend the charged particles for the momentum measurement. The spectrometer consists of two identical halves located above and

below the lepton beam pipe, and has an angular acceptance of ±170 mrad horizontally, and ±(40 − 140) mrad vertically.

Three drift chambers (DVC, FC1/2) in the front region, three multi-wire-proportional chambers (MC1/3) inside the magnet and four drift chambers (BC1/2 and BC3/4) in the backward region compose the tracking system of the spectrometer. The track reconstruction is based on a pattern-matching algorithm and momentum look-up method [13, 56]. The average angular resolution is better than 0.6 mrad and the average momentum resolution is better than 2% [13]. These resolutions degraded somewhat after the insertion of the Ring Imaging Cherenkov detector (RICH) to replace the threshold Cherenkov detector in 1998 with more materials in the path of the particles [57, 58].

Particle identification (PID) [59] is provided by a combined system of a lead-glass calorimeter [60], a pre-shower detector (H2), a transition radiation detector (TRD), and the RICH. The PID system allows for electron/positron identification with an average efficiency of 98 − 99% and a hadron contamination of less than 1%. The calorimeter plays a unique role in the DVCS study as it is the main detector that provides energy and position information for photons.

The trigger for the scattered electron/positron is formed by requiring hits in three scintillator hodoscopes together with energy above a certain threshold deposited in two adjacent columns of the calorimeter [13]. Fig. 3.3 shows the schematic side view of the forward spectrometer during the last 2 years running together with the Recoil Detector.

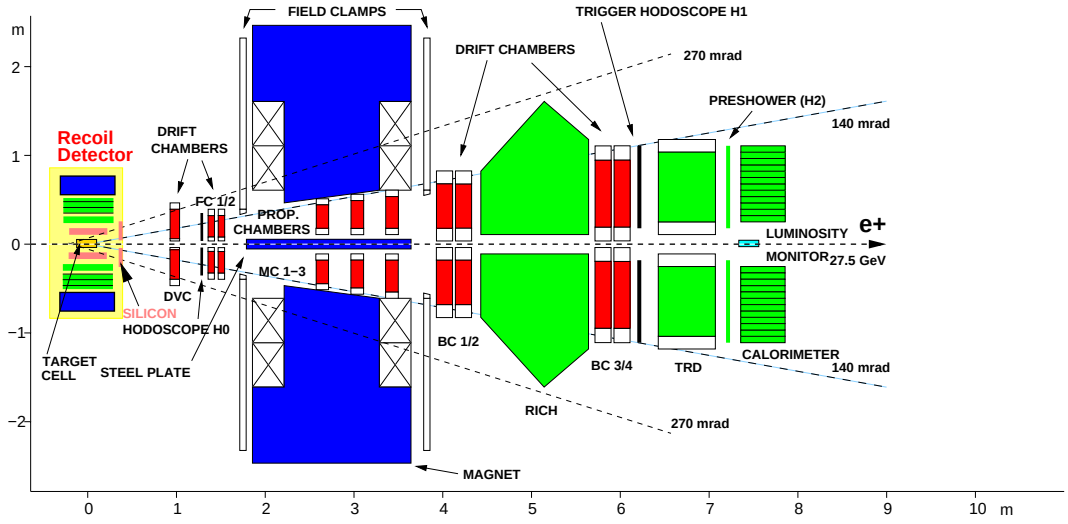

Figure 3.3: Side view of HERMES spectrometer configuration in the years 2006-2007.

3.2.1 The Tracking System

The magnet is essential to the HERMES tracking system, which is a H-frame type dipole magnet with a field integral of 1.3 Tm. It is located between the drift chambers FC2 and BC1 with field clamps in both sides to reduce the fringe fields. In order to shield the proton and the lepton beam pipe from the strong magnetic field, a septum steel plate was introduced in the beam plane. The magnet gap together with the steel plate enclose the geometrical acceptance $\pm(40 - 140)$ mrad in the vertical direction and ± 170 mrad plus another ± 100 mrad starting half-way through the magnet in the horizontal direction. Since such a passive shielding is still not sufficient, a correction coil with a deflecting power of 0.08 Tm is installed inside the septum plate in order to compensate the remaining dipole components. The fringe field at the positions of the adjacent drift chambers does not exceed 0.1 T. The field measurements have been done with a 3D-Hall probe on an automated 3D-mapping machine. The overall reproducibility of the results presents at a level of 0.1% and the results agree with the model calculations using the MAFIA and TOSCA codes [13].

The drift chambers DVC, FC1/2, BC1/2 and BC3/4 are the main tracking detectors of the conventional horizontal-drift type. Each chamber has 6 layers of drift cells (U,U',X,X',V,V') with a plane of alternating anode and cathode wires between a pair of cathode foils in each layer. The X and X' planes staggered by half the drift cell size with respect to each other are the vertical planes while the U and U' (V and V') planes are tilted by 30^o to left (right). A gas mixture of $Ar(90\%)/CO_2(5\%)/CF_4(5\%)$ is chosen for all the drift chambers, which is fast and non-flammable as required in a tunnel environment. The DC readout system consists of Amplifier/Shaper/Discriminator (ASD) cards mounted onboard the drift chambers, driving ECL signals on 30 m long flat cables to LeCroy 1877 Multihit FastBus TDCs in the external electronics trailer.

The DVC and FCs are used to determine the event vertex in the target cell, as well as to measure the scattering angles and the initial trajectories of charged particles before the magnet. The BCs are used to determine the trajectories of charged particles after the magnet, and to identify the hits in the PID detectors associated with each track.

The Multi-wire proportional chambers inside the magnet gap (MC1/MC2/MC3) were originally designed to help resolve multiple tracks in case of high multiplicity events. But it turned out to be very useful for the momentum reconstruction of relatively low energy particles with large deflection angles inside the magnetic field. Each chamber consists of three submodules U, X and V with the gas mixture of $Ar(65\%)/CO_2(30\%)/CF_4(5\%)$.

3.2.2 The Particle Identification Detectors

The HERMES particle identification (PID) system discriminates electrons/positrons, pions and other hadrons, it consists of a lead-glass calorimeter, two scintillator hodoscopes (H0 and H1), a lead-scintillator hodoscope H2 (the preshower detector), a ring-imaging Cerenkov detector (RICH) and a transition radiation detector (TRD). The PID is essen-

tial to the HERMES [13], as the rate of positrons from DIS is lower by factor of about 400 than that of hadrons (mostly pions) from photoproduction in certain kinematic regions. A high hadron rejection factor (HRF) and a low contamination of the lepton sample by hadrons were achieved by the HERMES PID system. The HRF is defined as the ratio of the total number of incident hadrons to the number of hadrons that are misidentified as leptons. A HRF of at least 10^4 is provided by the combination of the pre-shower, the calorimeter and the TRD.

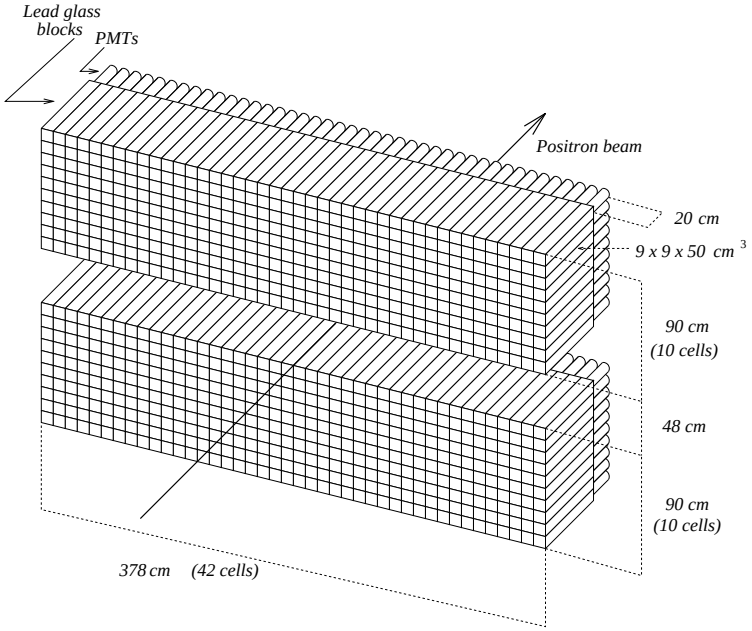

Figure 3.4: Isometric view of the HERMES calorimeter.

The function of the HERMES calorimeter is to provide a first level trigger for scattered leptons; to suppress pions in the leptons' selection at the first level trigger; to measure the energy of leptons and also of photons from radiative processes or from π^0 decays; and to give a coarse position measurement of scattered leptons and photons.

Each half of the calorimeter is constructed from 420 radiation hard F101 lead-glass blocks, arranged in 10 rows and 42 columns. Each block is coupled to a PMT of 7.5 cm diameter viewing from the rear side. A schematic drawing of the calorimeter is shown in Fig. 3.4. The blocks have an area of 9×9 cm^2, a length of 50 cm corresponding to 18 radiation lengths, they were polished, wrapped with 0.051 mm thick aluminized mylar foil and covered with a 0.127 mm thick tedlar foil to provide light isolation.

Each lead-glass block was calibrated within 1% at DESY in a 3 GeV electron beam incident at the center of the block. The calorimeter halves are moved away from the beam pipe during beam injection to prevent radiation damage of the lead glass. The effects of long-term radiation damage and long term stability in general are monitored by looking

at the ratio of the measured energy by the calorimeter to the reconstructed momentum of the leptons (E/p). It was found to be stable within 1% per year.

Due to the different topologies of electromagnetic and hadronic showers, electrons/positrons lose all of their energy in the calorimeter while hadrons deposit only a fraction of their kinetic energy through ionization energy loss. The ratio of E/p is typically unity for electrons/positrons and photons and less than unity for hadrons.

The energy resolution of the calorimeter for scattered leptons can be described by the following parameterization:

$$\frac{\sigma(E)}{E}[\%] = \frac{5.1 \pm 1.1}{\sqrt{E(GeV)}} + (2.0 \pm 0.5) + \frac{10.0 \pm 2.0}{E(GeV)}. \tag{3.3}$$

Impact positions of leptons and photons in the calorimeter can be obtained from the energy distribution inside the nine-block cluster. It can be calculated by the following energy-weighted average position of the cluster :

$$x = \frac{\Sigma_i x_i \sqrt{E_i}}{\Sigma_i \sqrt{E_i}}, \tag{3.4}$$

$$y = \frac{\Sigma_i y_i \sqrt{E_i}}{\Sigma_i \sqrt{E_i}}, \tag{3.5}$$

where x_i and y_i are the central coordinates of the i-th block, and the square root of the corresponding energy $\sqrt{E_i}$ is used as the weight. The position resolution can be evaluated by checking the difference between the positions of scattered leptons obtained in this way and the positions reconstructed from the tracking chambers.

The transition radiation detector (TRD) plays a key role in the particle identification system to provide a high pion rejection factor. The underlying principle of the TRD is the emission of transition radiation from a traversing of a relativistic charged particles between two media with different dielectric constants. In each medium, the particle induces a different Coulomb field. These fields do not match at the boundary. The required continuity at the boundary gives rise to an additional field - the transition radiation. The total energy emitted as transition radiation is given by

$$E = \frac{2}{3}\alpha\omega_p\gamma, \tag{3.6}$$

where α is the fine structure constant, ω_p the plasma frequency of the medium, and γ the usual Lorentz factor. Transition radiation is emitted in a cone about the particle track with an opening angle $\theta \simeq 1/\gamma$. At high energies the radiation, mainly consisting of X-rays, is therefore emitted almost collinear to the particle trajectory. Hadrons leave less amount of energy than leptons from transition radiation due to the larger mass.

The HERMES TRD consists of six modules above and below the beam. Each module (active area: 325×75 cm^2) contains a radiator and a proportional chamber to measure the

energy and the coarse positions. The radiator material is a predominantly two-dimensional matrix of fibres with 17-20 μm diameter. Each radiator is 6.35 cm thick and thus has approximately 267 dielectric layers. The MWPC consists of 256 vertical anode wires of 75 μm gold coated Be-Cu separated by 1.27 cm, and cathode planes made of 50 μm thick, double-sided aluminized mylar foils.

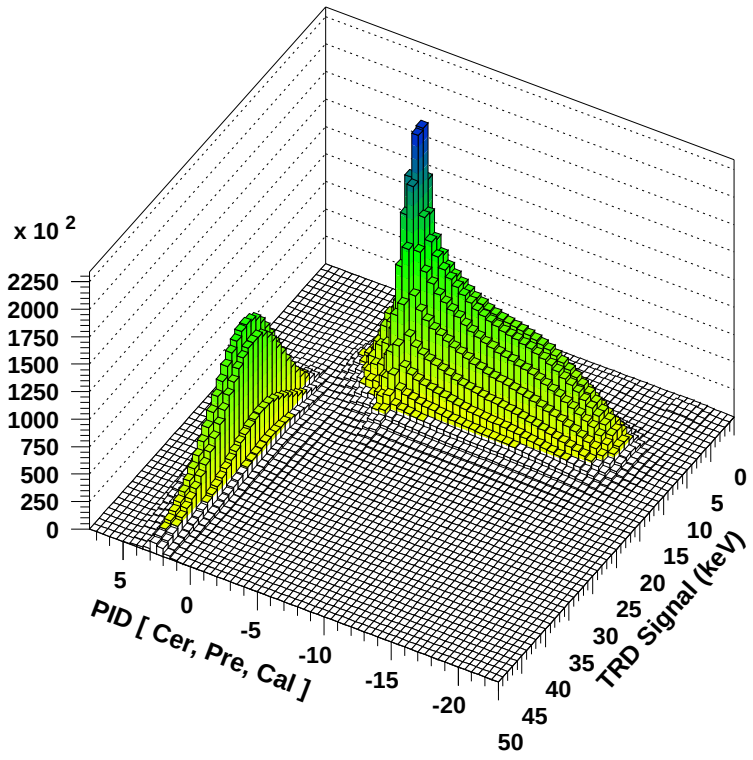

Figure 3.5: Plot of the PID3-TRD plane. Positrons appear at positive PID3 and large values of "TRD" signal.

Both positrons and hadrons deposit energy in the detector due to ionization of the chamber gas (dE/dx). Positrons deposit on average approximately twice this amount of energy due to transition radiation and the relativistic rise in dE/dx. Using the truncated mean method, in which the largest signal from the six modules is discarded and the average of the remaining is used, a PRF of about 150 for 90% lepton efficiency can be reached. Using a probability based analysis to combine the responses of the six modules, a PRF of 1460±130 can be reached with 90% lepton efficiency.

Three hodoscopes are installed in the HERMES spectrometer. The scintillator hodoscope H1 and the lead-scintillator H2 (the preshower detector) are constructed from 42 vertical panels of scintillator. Each panel is 1 cm thick and has an area of 9.3×91 cm^2. The modules overlap by 2-3 mm to avoid any gaps in the acceptance. Both hodoscopes are used to provide fast signals for the first level trigger. The preshower detector is additionally

used for particle identification. For this purpose, an 11 mm (2 radiation length) sheet of lead sandwiched between two 1.3 mm steel sheets is installed in front of the scintillator.

The front hodoscope H0 located directly in front of the drift chamber FC1 is constructed from a single sheet of 3.2 mm thick plastic scintillator corresponding to 0.7 % radiation length. The sole use of H0 is backward particle discrimination in the trigger. The low rate of about 1 MHz does not require segmentation.

The discrimination between positrons and hadrons by the pre-shower detector is based on the fact that for positrons the radiator will initiate electromagnetic showers and hence produce much more scintillation light than for hadrons. A pion rejection factor of 10 is provided by the pre-shower detector with 95 % efficiency for positron detection.

A ring-imaging Čerenkov detector was installed in the HERMES experiment in spring 1998 to replace the threshold Čerenkov detector. Charged particles passing through a radiator material with the velocity more than the speed of light in that medium will produce radiation photons, this is the underlying principle both for the RICH and the threshold Čerenkov detector. The RICH performs superior compared to the threshold Čerenkov detector as it measures the Čerenkov angle to discriminate the pions, kaons and protons.

The responses of the four PID detectors can be combined to provide good particle identification. The responses of the calorimeter, the pre-shower detector, and the Čerenkov are combined together to form a PID quantity PID3:

$$PID3 = log_{10}[(P^e_{Cal}P^e_{Prel}P^e_{Cer})/(P^h_{Cal}P^h_{Prel}P^h_{Cer})], \tag{3.7}$$

where P^i_j is the probability that a particle of type i produced a given response in detector j. Another quantity of PID2 was defined in the similar way using only the calorimeter and pre-shower detectors. Fig. 3.5 shows the distribution of PID3 versus the TRD signal. The positrons locate at the region with the positive PID3 and large TRD signal and the hadrons stay with negative PID3 and small TRD signals. The clear separation between the positrons and hadrons indicates a good PID performance for the experiment.

3.2.3 The Luminosity Monitor

Determination of the luminosity is essential to normalize data which are taken under different circumstances (e.g. different target spin states, different target gases, etc) as well as for a determination of absolute cross section. Luminosity is measured at the HERMES luminosity monitor by coincident detection of electron-positron or photon pairs, originating from the Bhabha scattering and the annihilation of the beam positrons with the target electrons. In the case of an electron beam, electron pairs are detected from the Møller scattering of the beam electrons with target electrons.

The HERMES luminosity monitor consists of two modules, located in the aperture in between the two calorimeter halves, at the left and right hand side of the beam pipe, 30 mm

away from the beam axis. Each module consists of an array of 3×4 $NaBi(WO_4)$ crystals, each having a size of $22 \times 22 \times 200$ mm^3. The coincidence rate of e^+e^- or e^-e^- particles is measured to determine the luminosity. The Bhabha scattering (Møller scattering) and annihilation events have a high energy deposition in both calorimeters, while most of the background events have a high energy deposition only in one calorimeter.

3.2.4 The Trigger System

The function of the trigger system is to distinguish interesting events from background with high efficiency, and initiate digitization and readout of the detector signals. A first level trigger of the HERMES spectrometer works within about 400 ns. This trigger requires the signals from the Hodoscopes (H0, H1, H2), the calorimeter, and a few chambers. The most important trigger in the HERMES is the DIS trigger (trigger-21), which selects leptons events by requiring hits in the three scintillator hodoscopes, H0, H1, and H2 together with sufficient energy deposited in two adjacent columns of the calorimeter, in coincidence with the accelerator bunch signal (HERA Clock). The hodoscope H0 is located in the front region of the spectrometer and consists of only one scintillator paddle in each detector half, read out by two PMTs. H1 is placed directly in front of the TRD in the back region of the spectrometer. Its setup is similar to the hodoscope H2 as described in the previous section. The timing between H0 and H2 is used to reject backward-going particles from the HERA proton beam. The hodoscope thresholds were set below minimum ionization. The calorimeter threshold is set to 1.4 GeV during the normal-low density data taking and to 3.5 GeV during the high density data taking, see Fig. 3.6.

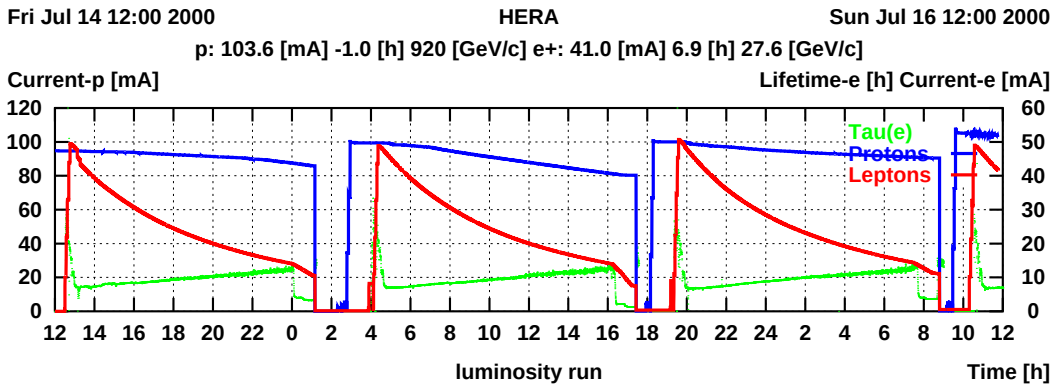

Figure 3.6: Example of the HERA performance. The upper (middle) curve represents the intensity of the proton (electron) beam and the lower curve indicates the lifetime of the electron beam over the 48 hours HERA running in July 2000. The drop in the electron beam lifetime was caused by the HERMES data taking with the high density of the gas target.

For a 3.5 GeV calorimeter threshold, two-thirds of the triggers had tracks, 95% of

reconstructed tracks came from the target, and one third had accompanying positrons. For a 1.4 GeV calorimeter threshold, the physics trigger rate increased by a factor of about 6 while the fraction of DIS leptons only went up by about 10%. These runs had significant contamination coming from collimator scattering just upstream of the target. About two-thirds of the events had tracks, but only 70% of the tracks came from the target, with most of the remaining one coming from the collimator.

Chapter 4

The Recoil Detector

Deeply Virtual Compton Scattering (DVCS) provides access to the Generalized Parton Distributions (GPDs), which offer a possibility to determine the orbital angular momenta of quarks [23]. The recoil protons from the DVCS and other hard exclusive processes can not be directly detected by the HERMES forward spectrometer [24,25,26]. The existed missing mass method to maintain the exclusivity is limited by the resolutions of the detectors and the incapability to clean the background from the semi-inclusive DIS and the associated BH processes. A Recoil Detector was built and installed to upgrade the HERMES forward spectrometer at the beginning of 2006 to measure the recoil protons [27].

4.1 The Design Requirements

The main background of DVCS measurement consists of the associated BH process with a Δ^+ resonance final state and the semi-inclusive DIS events. These backgrounds can not be completely cleaned by the missing mass technique and have a level of about 15% in the final exclusive data sample. Monte Carlo (MC) studies show [27] that most of the protons from DVCS and other hard exclusive reactions locate in the kinematic region with low momenta and large polar θ angles, which are out of the acceptance of the forward spectrometer. The relative low momenta of the recoil protons and the energy resolution of the calorimeter lead to a low resolution of the missing mass squared distribution M_x^2 with a value around 1.5 GeV^2. The left panel of Fig. 4.1 shows the kinematic distributions of recoil protons from elastic BH/DVCS events in terms of momentum p and polar angle θ. Most of the statistics are located at polar angles between 0.5 and 1.3 rad and momenta between 50 and 600 MeV/c. The right panel of Fig. 4.1 shows the missing mass squared distributions from data with positron (filled points) and electron (empty circles) beams and from MC simulations (solid line). The MC line is decomposed into elastic BH (dashed line), associated BH (filled area), and semi-inclusive (dotted line) processes. The contribution from the DVCS process is not included in the MC distribution, as at the HERMES kinematics the cross-section

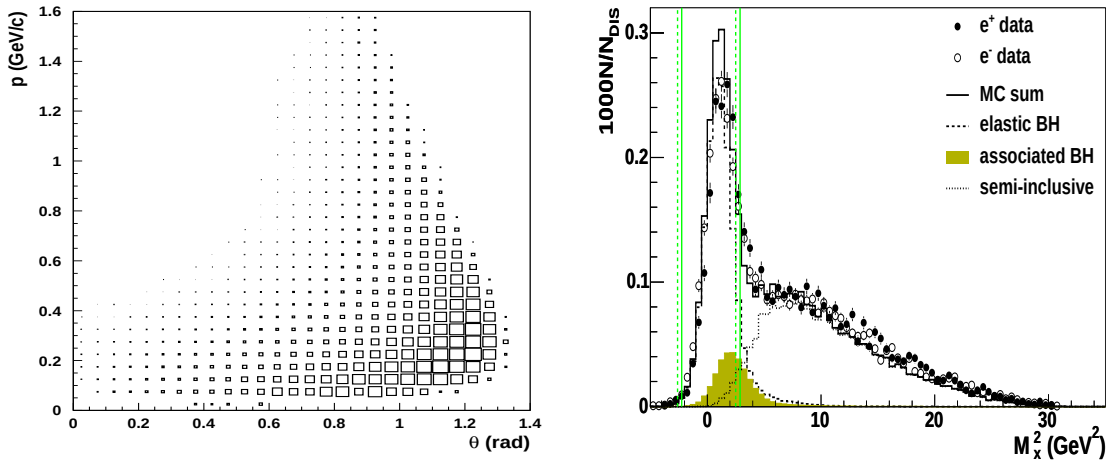

Figure 4.1: The left panel shows the two dimensional distribution of momenta versus polar angle θ of the recoil protons from the elastic BH/DVCS processes. The right panel indicates the missing mass squared distributions from data with positron (filled points) and electron (empty circles) beams and from Monte Carlo simulations (solid line). The latter include the contributions from the elastic BH (dashed line), the associated BH (filled area), and the semi-inclusive (dotted line) processes.

of the elastic BH process is much larger than the cross-section of the DVCS process. The exclusive region was chosen between -2.25 GeV^2 to 2.89 GeV^2 in the M_x^2 distribution, which corresponded to a range of -3 σ to 1 σ of the M_x and was determined according to the ratio of the background to signal [53].

As Eq. (2.2) illustrates, the invariant momentum transfer to the target t is a crucial quantity to access DVCS and GPDs. A high quality measurement of the different azimuthal asymmetries requires a high t-resolution. However the missing mass method can not provide a good t resolution, as it is indicated in the right panel of Fig. 4.2 with a t-resolution of around 0.17GeV^2 for the DVCS process.

Various MC studies have proven that the direct detection of the recoil protons will improve the measurement of DVCS significantly. A Recoil Detector was designed to fulfill the requirements of such a measurement. The Recoil Detector was installed in the HERMES experiment at the beginning of 2006 and took data together with the forward spectrometer until the end of HERA running in June 2007. It consists of three main components: a silicon strip detector surrounding the target cell inside the beam vacuum in a scattering chamber, a scintillating fibre tracker and a photon detector consisting of three layers of tungsten and scintillator bars. A schematic overview of the detector can be seen in Fig. 4.3. An aluminum target cell is located in the middle of the scattering chamber with 75 μm wall thickness. All three detectors are placed in a longitudinal magnetic field of 1 T generated

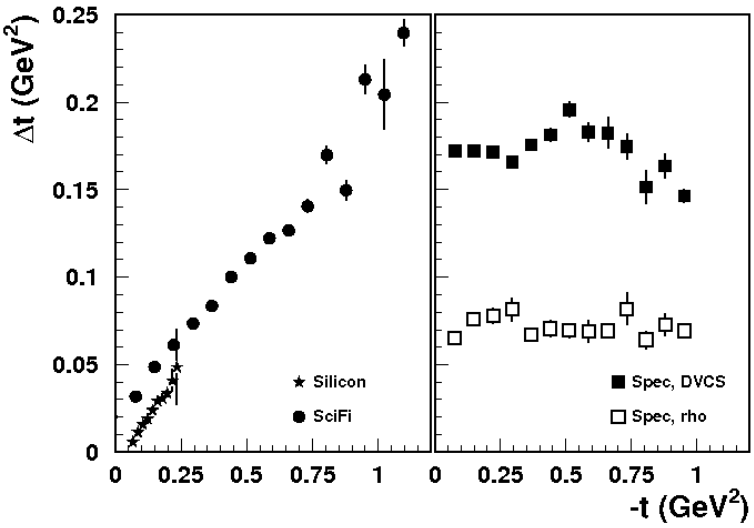

Figure 4.2: The resolution of the invariant momentum transfer to the target t of the DVCS process (filled symbols) calculated from the direct detected momenta of the recoil protons (left panel) and from the reconstructed photon energy with the forward spectrometer (right panel).

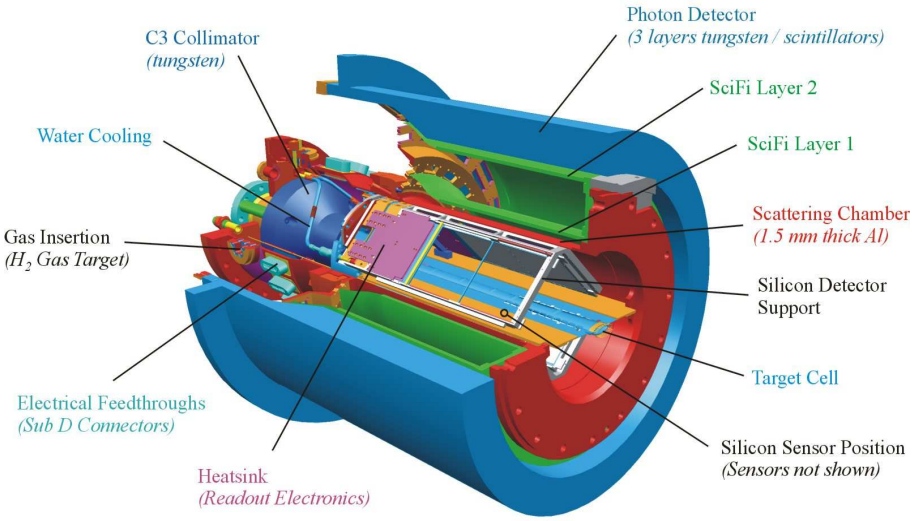

Figure 4.3: Schematic overview of the HERMES Recoil Detector.

by a solenoidal magnet. An additional collimator (C3) was installed in the front part of the target chamber to suppress the beam-related background in the Recoil Detector.

The silicon detector uses the energy deposition of the slow recoil protons to determine

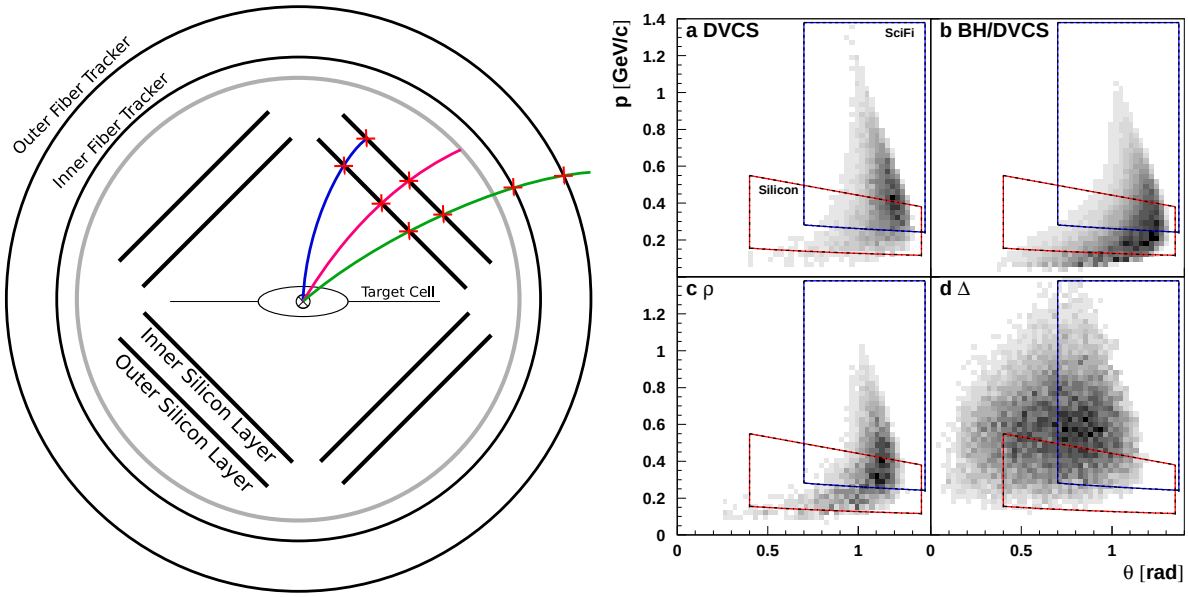

Figure 4.4: The tracking schema and the momentum coverage of the Recoil Detector. In the left panel, the slow protons stopping in the outer silicon sensor (blue line) or in the wall of the scattering chamber (red line) are reconstructed by their energy deposition; while the momenta of the particles reaching the fibre tracker (green line) are reconstructed by their bending inside the magnetic field. The momentum coverage of the silicon strip detector (red box) and the fibre tracker (blue box) is indicated in the right panel for the DVCS, the elastic BH/DVCS, the exclusive ρ, and the associated BH processes.

their momenta. The momentum reconstruction of the protons with higher momenta is achieved by the fibre tacker together with the silicon detector using the deflection of the charged particles in the longitudinal magnetic field. In addition, the energy deposition of the protons in the SSD is used to correct the reconstructed momentum, and the beam position is also used to constrain the tracking. The left panel of Fig. 4.4 shows the schema of the recoil tracking with different methods. Overall the Recoil Detector covers a momentum range up to 1.4 GeV/c. The right panel of Fig. 4.4 indicates the momentum coverage of the SSD and SFT for different physics processes. The low momentum cut-off which is determined by the SSD should be as small as possible and depends on the material between the interaction point and the inner silicon sensors (mainly the target cell). In addition to the large momentum coverage, the Recoil Detector also provides a high t-resolution for slow proton. The left panel of Fig. 4.2 indicates this resolution in the small momentum region. The particle identification is done by evaluating different energy depositions from protons and pions in the detector modules.

The photon detector is used for particle identification of high momentum particles and for background rejection of neutral particles by detecting the photons from the π^0 decay.

A fraction of 2/3 of the associated Δ^+ particle decay into a π^0 and a proton and can with certain efficiency be detected in the photon detector of the Recoil Detector to evaluate this background source. Furthermore, it may be possible to use the photon detector to reconstruct π^0 if both decay photons can be detected and well separated. In this case the Δ^+ may be reconstructed via the recoil proton and the reconstructed π^0.

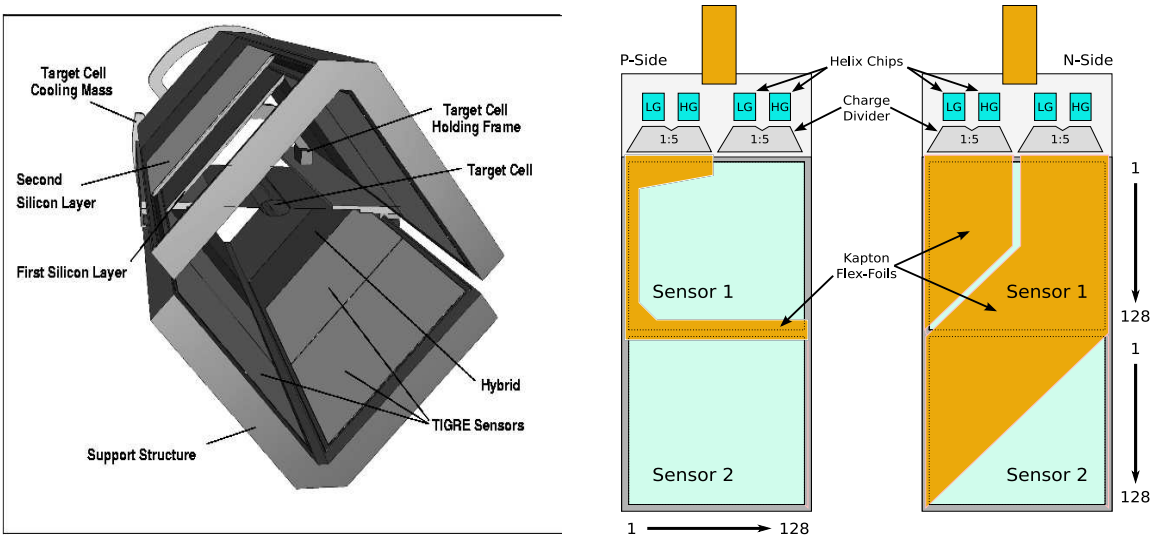

Figure 4.5: Left panel shows $3D$ model of the silicon detector and its support structure, looking upstream. Right panel shows the silicon sensor both the P- and N- sides.

4.2 Recoil Detector Components

4.2.1 The Silicon Strip Detector

The silicon strip detector (SSD) [61, 62, 63] was designed to measure the momentum of recoil protons in the range of $135 - 450$ MeV/c via their energy deposition and provides space points along the deflected trajectories for the tracking of minimum ionizing particles (MIPs) which include the high momentum protons and almost all the charged π mesons. It located inside the vacuum chamber, which requires that all components and processing steps are vacuum compatible. The SSD consists of 16 double sided silicon sensors based on a design of Micron Semiconductor. Both sides are segmented into 128 strips (4096 SSD-strips in total), with the p-side strips perpendicular to the n-side strips to form space points. The sensors have an active area of 97.3×97.3 mm^2 with a thickness of 300 μm and are placed around the target cell in two layers of four modules. The whole silicon detector consists of 8 single modules mounted in two layers on two roof-like structures, see the left panel of Fig. 4.5. The modules are constructed from a ceramic holding frame on

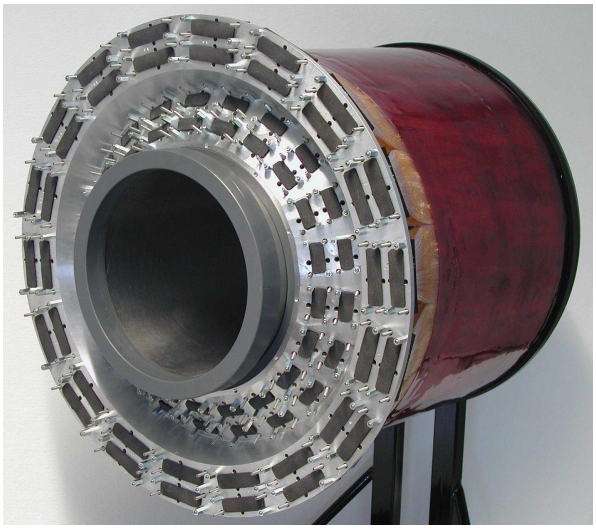

Figure 4.6: Picture of the completed Scintillating Fibre Tracker (SFT) mounted to a dummy scattering chamber. Protective caps are put onto connectors. Kapton film on outer barrel servers as protection from mechanical influence.

which the two silicon sensors are mounted, connected to an aluminum heat sink on which the read-out hybrids are fitted. The right panel of Fig. 4.5 shows the silicon sensors. The serializing read out chip Helix 3.0 is used to read out the SSD signal. The Helix chips are mounted together with some auxiliary electronics onto a printed circuit board. The electronic noise at the input stage is on the order of 400 e^- + 40 e^- / pF for not irradiated chips. The necessary high dynamic range of up to 70 MIPs is established by a charge division readout where the signal is split into a high gain and a low gain path: each silicon sensor strip is connected directly to one Helix read out chip (high gain) and via a 10 nF capacitive divider to a second Helix chip (low gain). This kinetic range enables the silicon detector to detect very low momentum recoil protons from the DVCS process.

4.2.2 The Scintillating Fibre Tracker

The scintillating fibre tracker (SFT) [64,65,66,67] was designed to measure the particles of higher momenta above 250 MeV/c using two barrels consisting of 4 layers of 1mm Kuraray SCSF-78 scintillating fibres each. Fig. 4.6 shows the completed SFT mounted on a dummy scattering chamber. A stereo angle of 10^o between each two adjacent layers of each barrel allows for space point reconstruction. The choice of the 1 mm fibres was a compromise of the spatial resolution and the financial budget of the SFT. The detailed specification of the fibres can be found in reference [68]. The 10^o of the tilt angle yields a modest polar angle resolution while the detector could still be easily assembled. Each layer was assembled in modules so that single modules with defects could have been discarded. The

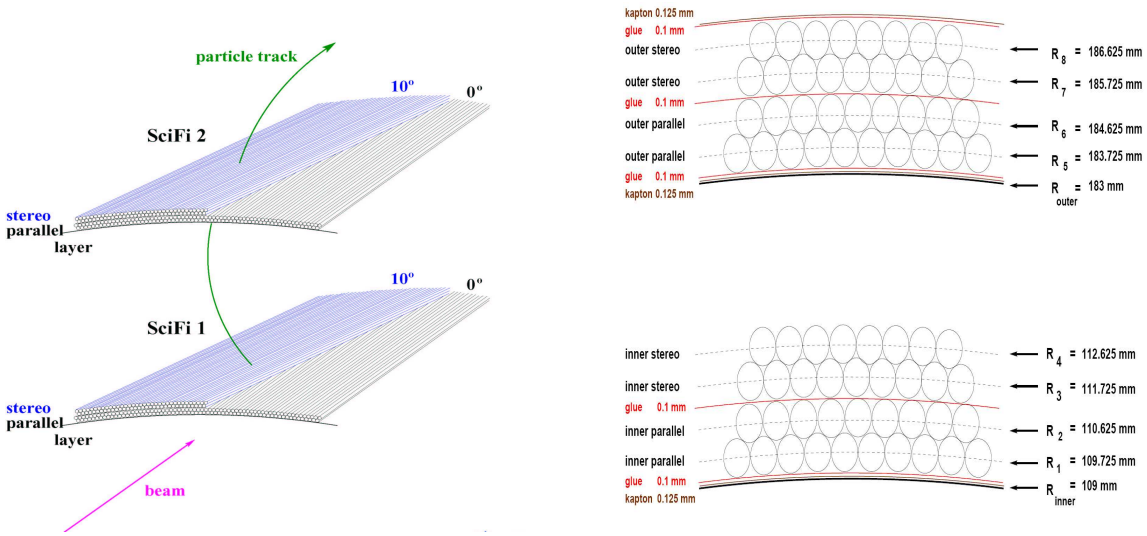

Figure 4.7: Arrangement of the fibres in the two barrels. The tracking concept is illustrated in the left panel while the detailed geometry structures of the fibre layers is demonstrated in the right panel.

diameters of the barrels are 220 mm for the inner and 370 mm for the outer respectively. These distances were optimized for the momentum resolution, and the outer distance is also constrained by the scattering chamber and the photon detector. The arrangement of the fibres can be seen in Fig. 4.7.

The signals of the fibres are read out on the upstream end via 3.5m long light guides of Kuraray clear fibres coupled to Hamamatsu H-7548 64-channel Photo-Multiplier Tubes (PMTs). The readout of the SFT is based on a Preprocessing Front-end Module (PFM) using GASSIPLEX chips which are hold-and-sample chips. A Charge Divider Circuit (CDC) was integrated on the Photo-Multiplier Board (PMB) to adapt the fast PMT signal to the PFM. The timing resolution of the GASSIPLEX is low so that the readout integrates over 6 adjacent HERA bunches, which would increase the random background [69]. In order to avoid this, the common dynode 12 signal of each PMT is used to extract additional fast timing information to discriminate between different HERA bunches.

The cylinders are built from 72 SciFi strips as self-supporting structures to minimize the material transverse by the particles. A gain monitoring system (GMS) was built to monitor changes in the response of PMTs. The momenta of particles are measured by deflection of the charged tracks in the solenoidal 1 T longitudinal magnetic field. From a test experiment with a mixed proton and pion beam at GSI/Darmstadt, the detection efficiency of the SFT modules for minimum ionizing particle using a threshold of 1 photo electron has been determined at $\approx 99\%$, efficiencies for protons even exceed this value. In addition to the tracking information, the energy deposition in the fibres was used to obtain pion/proton particle identification up to about 800 MeV/c.

4.2.3 The Photon Detector

The photon detector [70] consists of 3 layers of scintillator bars as active detector material with tungsten as a converter for the photons. The scintillator are 1.1 cm thick and are read out using wavelength shifting (WLS) fibres. The innermost scintillator are parallel to the beam, the two further layers have stereo angles of $\pm 45^o$ respectively so that charged particle tracks can be reconstructed in space. The first tungsten converter layer is 6 mm thick, corresponding to two radiation lengths whereas the other converter layers only correspond to one radiation length each. The signals are readout via two WLS fibres which are connected via clear fibres to the same type of PMTs as the fibre tracker. The photons from the decay $\Delta^+ \rightarrow p\pi^0 \rightarrow p\gamma\gamma$ can be detected by the photon detector only and will allow for the further reduction of non-exclusive background events. The photon detector also provides a cosmic ray trigger for test and alignment measurements, and provides additional pion/proton particle identification at higher momenta together with the fibre tracker.

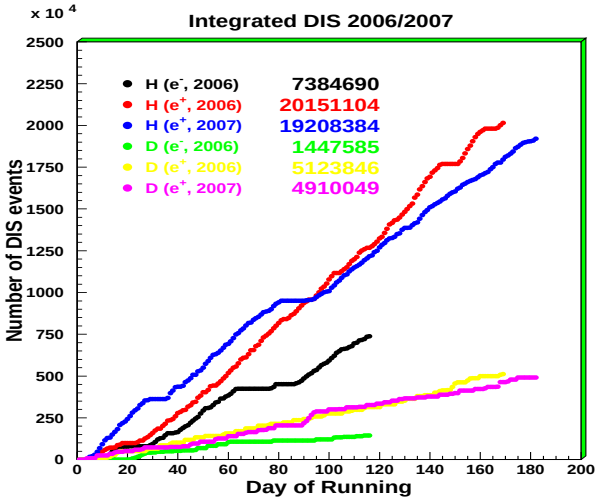

Figure 4.8: The number of DIS events collected from years 2006 and 2007.

4.3 The Commissioning of the Recoil Detector

Before the Recoil Detector was installed in the HERMES experiment, the completely assembled detector had been tested in 2005 using cosmic particles with the magnetic field turned on at a test site in the HERMES experimental hall. This test not only provided the chance to commission the whole hardware and data acquisition system, but also gave the opportunity to accumulate cosmic data, to develop required software, and to take data for the internal alignment of the detector.

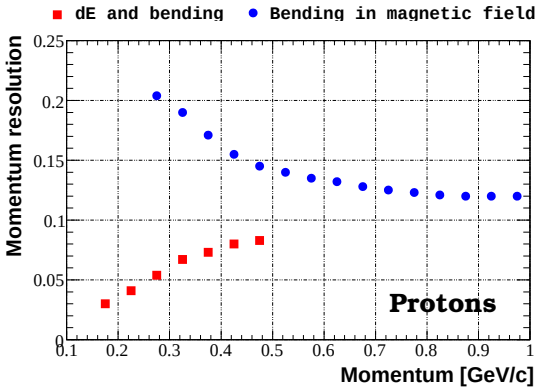

Figure 4.9: The resolution of the reconstructed momentum for the recoil protons. The squares represent the tracks reconstructed by the energy deposition from the SSD while the circles indicate the ones reconstructed by the bending inside the magnetic field.

The detector was installed in January 2006 and the commissioning started with the electron beam in February. The SFT performed smoothly from the beginning while the silicon detector could not be commissioned due to serious noise induced by the beam. Later the silicon detector suffered from a radiation damage, which caused a hole in the target cell. After that most parts of the detector were dismounted and the silicon detector was repaired and reinstalled along with an improved target cell in July 2006. At this time the HERA machine was switched to a positron beam. After that the detector was fully commissioned and took data successfully until the end of HERA running. Fig. 4.8 shows the number of DIS events collected with the Recoil Detector in 2006/2007 by different beam species and types of target. For the positron beam, a large amount of data was taken with the fully commissioned detector both in 2006 and 2007. For the electron beam, the data was only taken with the SFT. Currently it is still under study about how to use this data period.

To get usable data sample for physics analysis, a lot of effort has been made to align and calibrate the data, and to polish the reconstruction software. Meanwhile the HERMES Monte-Carlo (MC) programme was tuned for the Recoil Detector based on the knowledge gained from data. This work has not been completely finished yet, some of the alignment and calibration procedures have to be iterated to improve the data quality. After a rough alignment of the SFT and SSD with the cosmic data, the residuals were measured to be 0.27 mm for the silicon detector and 0.35 mm for the SFT, about 20% higher than what would be expected for a perfectly aligned detector. However the reconstruction software worked well with such aligned detector and provided possibility for the calibration and extraction of detector performance for the MC programme. Fig. 4.9 shows the resolutions of the reconstructed proton by the Recoil Detector. In the small momentum region, the detector provides a very good momentum resolution for the study of the DVCS and other exclusive processes.

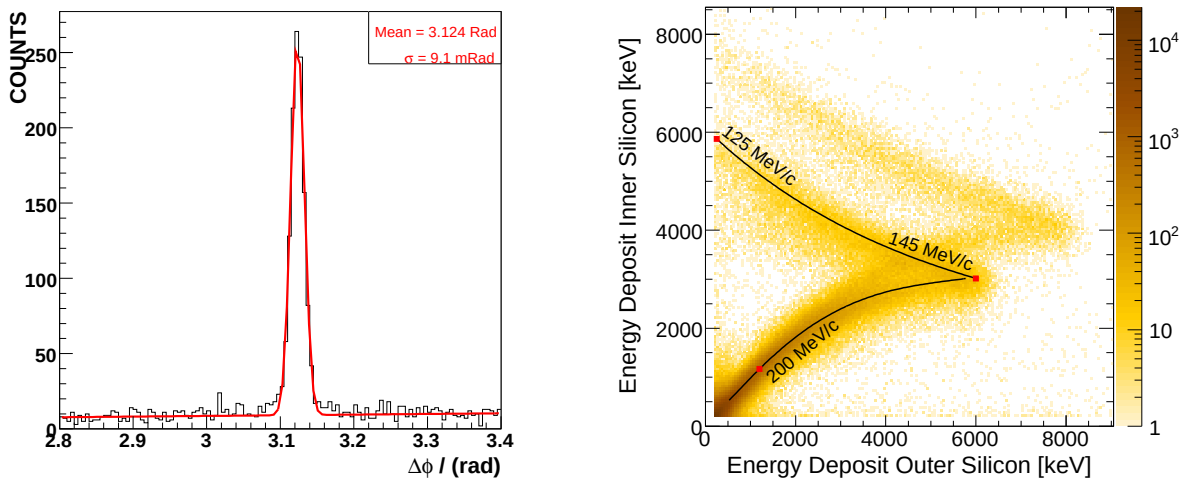

Figure 4.10: Two examples of the detector performance. Left: The difference of the azimuthal angles for the ep elastic scattering protons measured by the SFT and the forward spectrometer. Right: The distribution of the energy deposition measured in the inner and outer SSD layers from the deuterium target. The black line represents the results from a Geant4 simulation using protons.

Two examples can be seen in Fig. 4.10 to demonstrate the performance of the detector. In the ep elastic scattering process the scattering electron and proton fly in the opposite directions along the beam. The left panel of Fig. 4.10 illustrates the difference of the azimuthal angle of the scattering electron measured by the forward spectrometer and the azimuthal angle of the recoil proton measured by the SFT. A peak at 3.124 rad with the σ of 9.1 mrad is obtained from a Gaussian fitting (the red line). The two numbers indicate good relative position and azimuthal resolution capabilities of the SFT. The right panel shows the distribution of energy deposition measured in the inner and outer SSD layers from the deuterium target. The black line represents the results from a Geant4 simulation using protons and is in agreement with the measurement. The additional second band corresponds to deuterons stopped in the outer SSD layer.

Chapter 5

The Commissioning of the SFT

The scintillating fibre tracker (SFT) is the key component of the Recoil Detector, which was located between the silicon detector and the photon detector inside the magnetic field. It provides two spacepoints for the track reconstruction of the high momentum protons (250 - 1400 MeV/c) and nearly all the pions, at the same time it provides information for the particle identification via energy deposition from the charged particles. An overview of the fibre tracker has been presented in the previous chapter and in the references [27,66]. This chapter describes the commissioning details of the SFT, which are related to the offline data handling, the raw data corrections, the various calibrations, the noise extraction during the running of detector and the SFT particle identification.

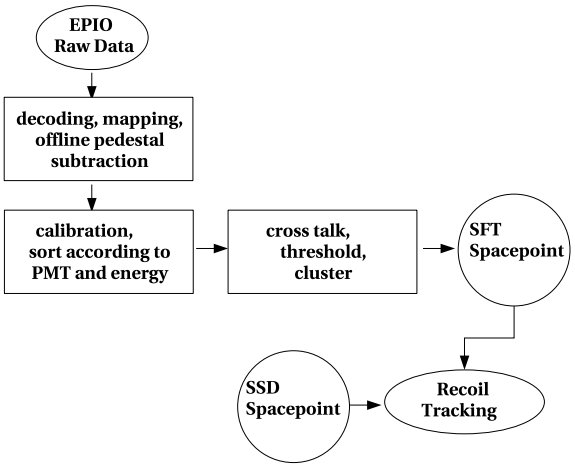

Figure 5.1: Flowchart of chain of the SFT data analysis

5.1 The Chain of the Data Analysis

A standard flow was designed to make the data collected by the HERMES forward spectrometer usable for the physics analysis, which includes several steps and a lot of offline software [71]. In the first step, the raw data based on the EPIO format coming from the DAQ are decoded by the HERMES decoder program (HDC). In the next step, the information from the various detectors are combined and the tracks are reconstructed by the HERMES Reconstructing program (HRC). Alignment and efficiencies are calculated by the ACE program. The final analyzable data are stored in a so-called μDST format.

The raw data taken by the SFT was also stored in the EPIO format, actually together with the other two sub-detectors they were merged with the data from the forward spectrometer into the same data flow and stored on tape. The pedestal was conservatively subtracted online according to the pedestal service data, which were taken previously parallel to the running and could be manually adjusted for specification in the readout system.

Similar to in the forward spectrometer, the first step of the offline data chain is to decode the raw data of the single hits from certain channels, PMTs, layers and barrels. Since during the online data acquisition, the readout encodes hits from the instruments (the positions and the ADC values) into the data-flow in a certain format. During the decoding stage, the decoder separates single hits from the data-flow, and maps them back to the corresponding instruments. However, for the SFT, an additional offline pedestal subtraction was done in the HDC to update the pedestal because it drifted relatively frequently during the data taking. This additional subtraction used information from the pedestal runs taken normally every 2 hours during the data taking.

Other steps to cope with the raw Recoil data are done in the HERMES eXternal Tracking Code (XTC), which was made to perform tracking outside of the standard HERMES acceptance. As seen in Figure 5.1, these steps include the calibrations, the cross talk and cluster corrections to raw data, and if needed the threshold cut on the raw data to remove the noise or background, finally the corrected data entering the SFT spacepoint routine which combines the SFT and SSD spacepoints to the final tracking stage.

The XTC is an important framework to handle both the offline data and the generated data from the Monte-Carlo (MC) programme. It contains not only the raw data handling functions for all the three sub-detectors but also the routines for the recoil tracking.

5.2 Gain Calibration of Photon-Multiplier Tubes

The Hamamatsu Multi-Anode Photon-Multiplier Tubes (PMT) H7546 were chosen to read out the signals from the scintillating fibres. The maximum sensitivity to the wavelength of the incident light is around 420 nm, close to the peak emission wavelength of the scintillating fibres. As the gain is proportional to the high voltage applied to the PMT, the nominal gain is of the order of $10^5 - 10^6$ when the high voltage is set between 800 V and

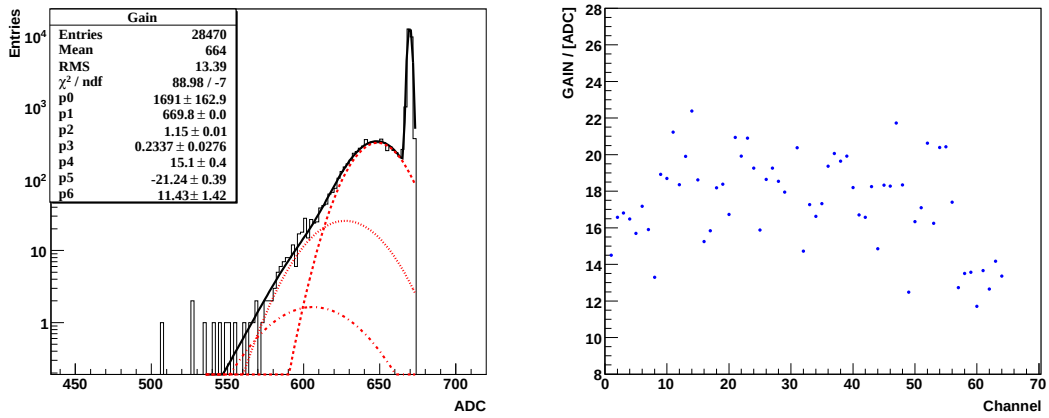

Figure 5.2: Fit of the Poisson function to a single Multi-Anode Photo-Multiplier Tube (PMT) channel spectrum obtained by low level LED illumination. Due to the readout logic high ADC values correspond to low PMT signals. The black curve display contributions from the pedestal and the signals. The red curves represent the contributions from the 1-, 2- and 3-electron. The right figure shows the uniformity of the gains from all 64 channels on one PMT.

1000 V.

The SFT readout needs to be calibrated in order to be suitable to measure the energy deposition of the particles. This was done in the early days of the detector construction by flashing the PMT cathode with weak blue light emitted by a LED [72], as the PMT is sensitive to the wavelength of blue light. A test-stand was set up with the same readout system as in the data taking period to determine the proper high voltages finally used for the experiment, and to measure the gains from the PMT channels under certain high voltages. The left panel of Fig. 5.2 shows the ADC spectrum of one PMT channel from that measurement. The spectrum was fitted by a Poisson function to obtain the single-electron peak [73, 74], which results from the entry of single photo electrons into the multiplier system and is a very natural way to demonstrate the gain. In the figure, the red curves represent the contributions of 1-, 2- and 3-electrons, the black curve represents the overall contributions including the pedestal. The gain can be obtained from the fit using the distance between the single-electron and the pedestal. The uniformity of the gain across all the anodes is expected to be about a factor of 2 according to Hamamatsu which was confirmed by this measurement. The right panel of 5.2 illustrates the gains from all 64 channels of one PMT. The gains from the first 8 and last 8 channels in the PMT surface are always lower than those from other channels as indicated by Hamamatsu, the maximum ratio is around 1:2. This is acceptable and it is a very important parameter as a proper dynamic range is essential for the measurement of the recoil protons.

According to Hamamatsu the gain is expected to be exponential to the supply volts.

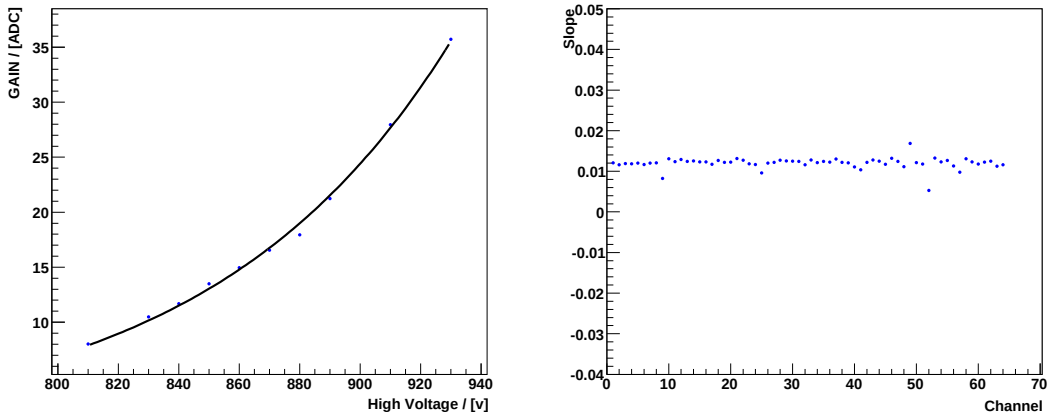

Figure 5.3: Gain versus supply voltage on the PMT. The left panel shows that the correlation between the gain and the supply voltage agrees with the function $Gain = b + e^{K*Voltage}$. The right panel shows that the K from the function for different channels in the same PMT is the same.

The left panel of Fig. 5.3 shows the gains from one PMT channel under different high voltages, a function Gain = b + $e^{K*Voltage}$ can very well describe these points as indicated by the black curve. The right panel of Fig. 5.3 shows the parameter K from different channels in one PMT, the Ks are the same from all channels in one PMT. The correlation between the gain and the supply voltage has been used to tune the high voltage to get the desired gain during the detector commissioning.

5.3 Cross-Talk Corrections

There are two main types of cross-talks occurring in the SFT: the one coming from the light leakage between the scintillating fibres and that from the optic leakage in the PMT surface. The uncorrected cross-talks are problematic [75], they may lead to wrong tracking information from the SFT barrels and alter the energy response. As there are two types of cross-talks for the SFT, it would be difficult or even impossible to distinguish them if the adjacent fibres were connected to the neighboring PMT pixels. However an advanced feeding scheme was used to construct the detector to avoid this problem. In this scheme as shown in the left panel of Fig. 5.4, the adjacent fibres (in the figure the numbers correspond to the fibre positions) in the SFT barrel are not connected to the neighboring pixels in the PMT surface. Furthermore the four neighboring PMT pixels are not connected to each other in the SFT layer, as an example, the four neighboring pixels to the pixel-19 are -3, -11, -26 and -28 and these numbers clearly demonstrate that the fibers connected to them are not neighboring fibres in the SFT barrel. Such a scheme is very essential for the

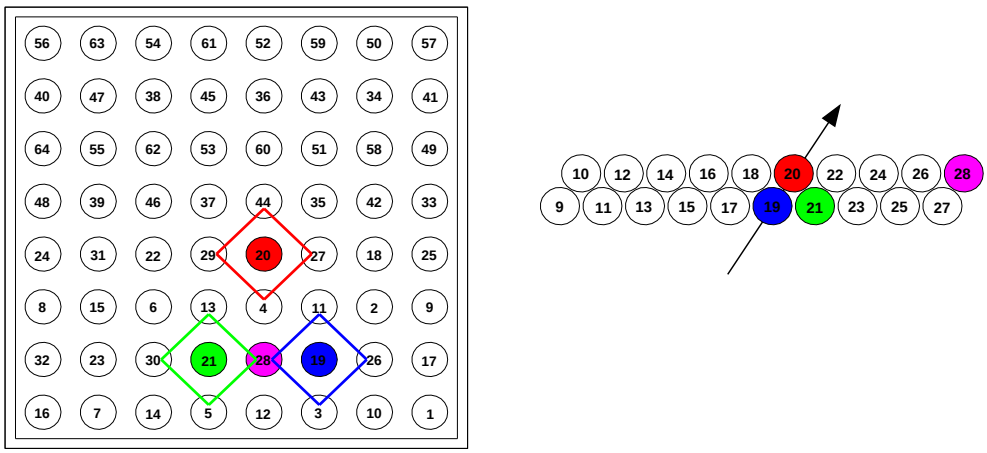

Figure 5.4: The SFT feeding scheme. The left figure shows the mapping of fibres to the PMT channels on the cathode. Odd(even) numbers correspond to fibres in the lower(upper) layer of a module. The right figure shows the corresponding fibres in the module.

successful correction of the cross-talks.

The cross-talk correction routine can handle both types of cross-talks. To clearly explain how these corrections work, we start with an example track passing through the fibre layer in the right panel of Fig. 5.4. In the figure a particle traversing the SFT layer through fibre 19 and fibre 20 exactly and its deposited energy generate signals in the PMT channels connecting to these 2 fibres, the corresponding pixels can be seen in the left panel of the figure. Due to the cross-talk effect, fibre 21 is also fired. Tracing these 3 fibres back to the PMT, each of them may cause the optical cross-talk in the PMT surface, for each of the three pixels, the cross-talk correction loops over their four direct neighboring pixels, for any of fired neighboring pixel, its energy will be added up to the central pixel as one hit in the PMT. In this correction only the four direct neighbors are taken into account, the diagonal neighbors are not touched due to the fibre feeding scheme and the not so strong cross-talk of this type of PMT. Investigations by the MINOS collaboration using the same PMT for their fibre tracker show [76] that the signal in the center pixel accounts for about 90% of total signals, direct neighbors make up about 8% and diagonal neighbors the last 2%. This is confirmed by looking at the signal of the channel with the largest signal in the PMT and the signals from its four neighboring channels in the PMT surface (see Fig. 5.5). Back to the example, the pixel-21 and -19 have the same fired neighboring pixel-28 while there is no fired neighboring pixel for the pixel-20. In this case the pixel-20 doesn't need any correction while the signal of the pixel-28 is split into two parts weighted by the values of the signals from pixel-19 and -20. Then the two parts are added to the

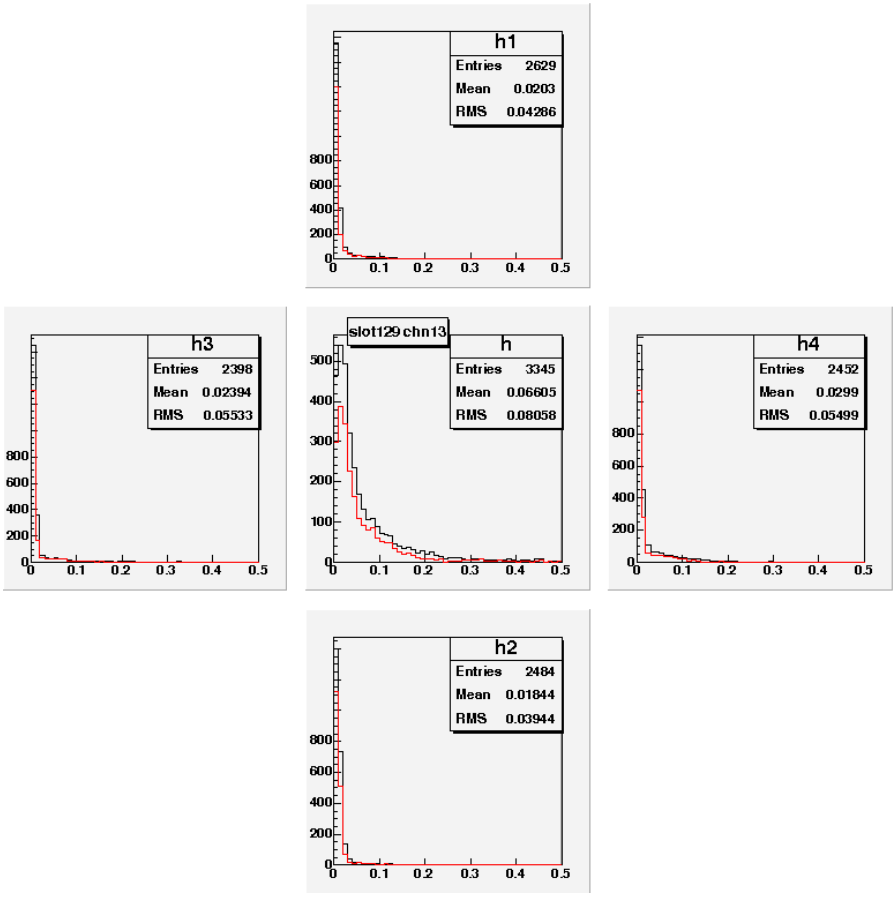

Figure 5.5: The pixel with the largest signal in one PMT and the signals from it's four direct neighboring pixels (black histogram). A threshold was required to select the largest signal for the red histogram.

two pixels separately.

After the cross-talk correction in the PMT surface, only the fibres-19, -20 and -21 are fired in the SFT barrel and the signal of fibre-28 is removed due to the correction, which of course fits better to the reality. The cross-talk correction in the fibre level will then take place. The principle is to combine all neighboring fibres into one cluster weighted by their signals. In this case the fibre-19 will be combined by -21 to form a new virtual fibre which is between the -19 and -21 according to their signals. After this correction the new virtual fibre and the fibre-20 are called the clusters which then will be delivered to the spacepoint routine to form the spacepoint with the space coordinate for the tracking.

5.4 The SFT Noise Study

Apart from signals of particle tracks, the Recoil Detector receives noise signals from various sources. To understand the effect of noise on the data, a proper noise model is needed to tune and test the tracking methods; and to make data-MC comparisons with the MC program. The noise was measured for the Recoil Detector with some dedicated runs under different beam conditions with trigger 29 just before the HERA shutdown. The detailed procedure and the results of the analysis on these data will be explained in this section.

5.4.1 Noise Measurements

Possible sources of the noise in the Recoil Detector are [77]: electrical noise (due to machine operation), Møller scattering, synchrotron light, collimator scattering, and proton showers. In order to measure all the possible sources of the noise, it was decided to take the measurements [78] using the HERA-Clock (trigger 29) at the maximum allowable rate (pre-scale factor of 10K), meanwhile all the other triggers were prescaled to zero. Four sets of data sample were collected with trigger 29 under different beam conditions. Measurements triggered with HERA clock were taken at the maximum trigger rate at the beginning of one fill (Positron Beam current 28mA) and at the end of that fill (Positron Beam current 15mA). Additionally the noise was measured with the empty target (Positron Beam current 35mA), to understand the noise coming from the target. The influence of Møller scattering can be seen by the comparison of the measurements with empty and filled target. A measurement was also performed with only the proton beam at the end of one fill when HERA dumped the positron beam and kept running with the proton beam. All the four sets of measurements provide the opportunity to determine the noise rate in the detectors from most possible sources.

5.4.2 Analysis Procedure

The pedestal drifting can affect the determination of the noise occupancy of the SFT. The pedestal has been mainly cut off during the online data taking and further subtracted in the stage of offline decoding. There is still some remaining pedestal left in the PMTs which then can increase the occupancy calculation largely and bias the noise determination. During the noise measurements, pedestal movement has been noticed in one box located in the inner SFT barrel. The left panel of Fig. 5.6 shows the noise occupancies of the inner parallel SFT layers and clear bumps can be seen between fiber 376 to fiber 437. The observed bumps clearly indicate the pedestal drifting during the noise measurements.

In the normal offline data analysis, this kind of remaining pedestal will be removed by imposing certain threshold cuts to the data in the XTC programme. However, the current analysis is performed based on the raw data right after the HDC output before going through the XTC stage. To eliminate the effect from the remaining pedestal to the

noise determination, a threshold cut at 15 ADC channels was used for the analysis. This is a conservative cut compared to that used for the data production in the XTC stage and has been found out to be very useful in the GSI test beam [64]. The right panel of Fig. 5.6 shows the ADC distribution from the part of the inner parallel layers with the drifting PMT pedestals (black line) and the part without any pedestal drifting (red line). It is clear that if there are remaining pedestals in the SFT, they are always the hits with small signals, and can be cut away with the threshold cuts.

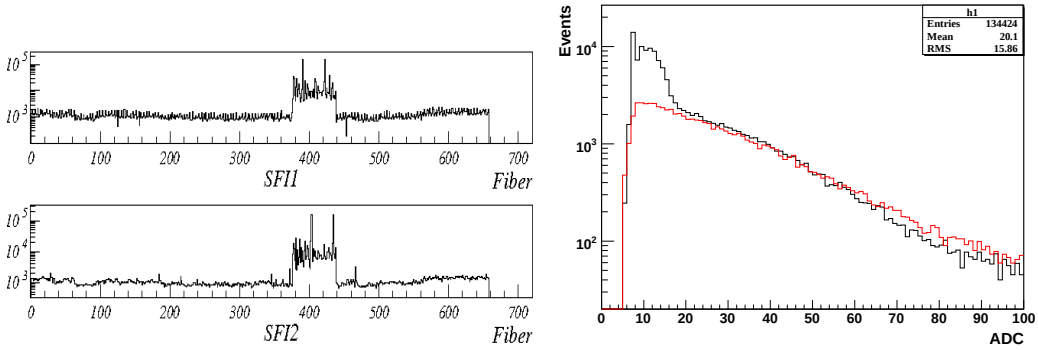

Figure 5.6: The pedestal drifting during the noise measurements. The hit multiplicities from inner parallel layers are plotted in the left panel. Clear bumps can be seen from fiber 376 to fiber 437 due to the pedestal movement. The right panel shows the ADC distribution from inner parallel layers with the PMT pedestal shifting (black line) and the without the pedestal shifting(red line).

The triggers in the HERMES experiment are generated according to a clock corresponding to the beam bunches provided by the HERA accelerator. In other words, the HERMES triggers are fired when the bunch arrives at the interaction point. Due to the low timing resolution of the GASSIPLEX chips, the SFT readout system can not be used to distinguish the signals from the triggered bunch and its neighboring non-triggered bunches [69]. To get rid of this disadvantage of the readout system, signals from the 12th dynode in PMT via the TDC have been used to determine a timing signal of the hit in the PMT. The noise occupancy is counted from the different timing slices corresponding to the different bunches after the threshold cuts. However, the 12th dynode is common for all 64 channels of the PMT, while the channels from the same PMT in the inner SFT barrel are split into different layers. Hence, only two occupancy numbers can be extracted from the inner barrel for the parallel layers and the stereo layers separately, despite the fact that all the individual inner layers can be read out [64, 66]. For the outer SFT, there will be two numbers to describe the noise rate from the outer parallel layer and the stereo layer separately.

Fig. 5.7 indicates the noise occupancies in different timing slices extracted from the

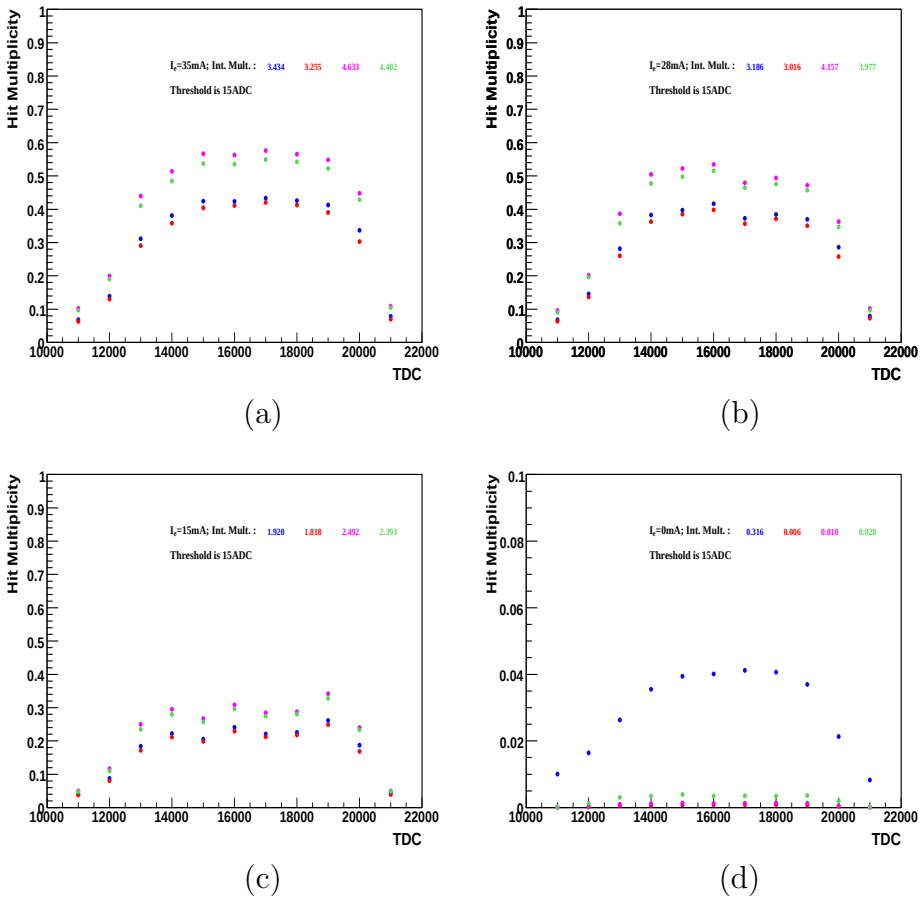

Figure 5.7: The noise occupancies in different timing slices extracted from the trigger-29 noise data. The points of different colors indicate the hit multiplicity from different layers, the blue (red) points are from the inner parallel (stereo) layers, while the pink (green) points denote the outer parallel (stereo) layers. A threshold cut at 15 ADC channels was used here. The panel (a) [(b), (c), (d)] represents the occupancy versus the timing slices with the beam current 35 mA [28, 15, 0 mA]. In the panel (a) the target is empty, while in the panel (d) there was only proton beam in the machine.

trigger-29 noise data. Different timing slices represent different bunches in the HERA lepton ring. The bunch around 15000 [0.1 ns] is when the HERMES trigger takes place. The interval between two neighboring slices is around 96 ns corresponding to the interval between two adjacent HERA bunches. The points of different colors indicate the hit multiplicity from different layers, the blue (red) points are from the inner parallel (stereo) layers, while the pink (green) points denote the outer parallel (stereo) layers. A threshold cut at 15 ADC channels is used here. The panel (a) [b,c,d] represents the occupancy versus the

timing slices with the beam current 35 mA [28, 15, 0 mA]. In the panel (a) the target is empty, while in the panel (d) there was only proton beam in the machine. The integrated number of occupancy from different bunches can be found in Table 5.1 for different beam conditions.

Table 5.1: The noise occupancies of the SFT for different beam conditions and for different SFT layers.

Beam Condition	Inn.Para. Layer	Inn.Ster. Layer	Out.Para. Layer	Out.Ster. Layer
$I_e = 35mA$	3.434	3.255	4.633	4.402
$I_e = 28mA$	3.186	3.016	4.157	3.977
$I_e = 15mA$	1.920	1.818	2.492	2.393
Proton Beam	0.316	0.006	0.01	0.028

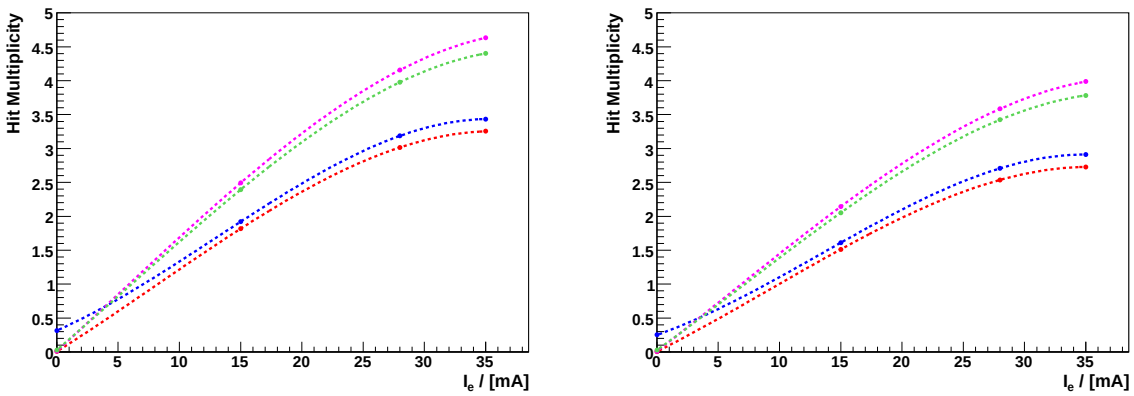

Figure 5.8: The distributions of the noise occupancies versus the positron beam currents. The blue (red) points are from the inner parallel (stereo) layers, the pink (green) points denote the outer parallel (stereo) layers. The dashed lines are from the polynomial fittings. The left panel indicates the results with threshold cut at 15 ADC channels; while a threshold cut at 20 ADC channels was imposed in the right panel.

The noise occupancy increases with the positron beam current (see Table 5.1), while the proton beam does not cause much noise rate in the SFT except for the inner parallel layers. Fig. 5.8 shows the distributions of the noise occupancies versus the positron beam currents. The layout of the colors is the same as the ones in Fig. 5.7: the blue (red) points are from the inner parallel (stereo) layers, while the pink (green) points denote the outer parallel (stereo) layers. The dashed lines are from the polynomial fittings. The left panel of Fig. 5.8 indicates the results with thresholds at 15 ADC channels; while in the right panel of Fig. 5.8 the results with thresholds at 20 ADC channels are demonstrated to check the effect the threshold cut. Table 5.2 shows parameters of the fits from the left

panel of Fig. 5.8. The hit occupancies from different bunches in different layers are shown in Table 5.3 when the beam current is 28 mA, the integrated numbers from Table 5.3 have been implemented into the MC as the worst case for the SFT noise model.

Table 5.2: The polynomial fitting parameters from the left panel of 5.8, the threshold of 15 ADC channels was implemented here.

Layer	p0	p1	p2	p3
Inn.Para. Layer	3.163e-01	7.908e-02	3.036e-03	-7.858e-05
Inn.Ster. Layer	5.948e-03	1.136e-01	1.282e-03	-5.359e-05
Out.Para. Layer	1.025e-02	1.654e-01	7.211e-04	-4.776e-05
Out.Ster. Layer	2.825e-02	1.554e-01	9.155e-04	-5.098e-05

Table 5.3: The noise occupancies extracted from different bunches in different layers when the positron beam current is 28 mA. The threshold of 15 ADC was implemented here. The zero bunch indicates the triggered bunch; the bunches with negative numbers denote the bunches before the triggered bunch; while the positive numbers are for the bunches after the triggered bunch. The absolute number in the first column shows the location of the bunch compared to the triggered bunch.

Bunch	Inn.Para Layer	Inn.Ster. Layer	Out.Para. Layer	Out.Ster. Layer
-4	0.068	0.064	0.096	0.091
-3	0.146	0.136	0.201	0.196
-2	0.282	0.260	0.387	0.358
-1	0.383	0.362	0.505	0.478
0	0.397	0.385	0.523	0.498
1	0.417	0.398	0.534	0.516
2	0.373	0.356	0.479	0.465
3	0.384	0.371	0.494	0.475
4	0.370	0.350	0.472	0.457
5	0.286	0.258	0.363	0.348
6	0.079	0.073	0.101	0.096

So far the noise occupancy has only been extracted from the individual layers under different beam conditions. To build a proper noise model the correlations between the different layers have to be understood. The physics processes normally leave the space points in the detector and form certain hit correlations between the individual layers. If there is only electrical noise in the SFT, they are randomly distributed in the layers and on the PMTs. The noise occupancy has only been investigated at the level of raw hits

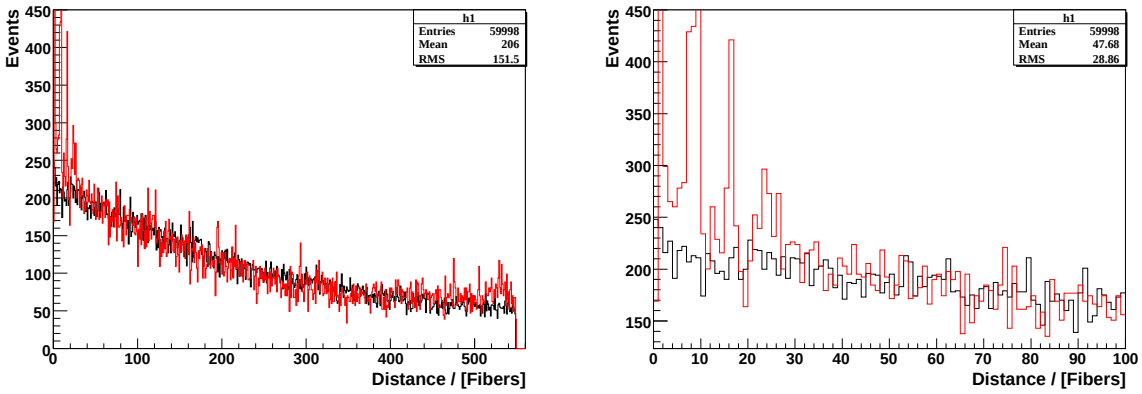

Figure 5.9: The distance of the two neighboring raw hits after the readout from outer parallel layer. The events with four hits in the layer are included. The red line is from the trigger-29 data and the black line is the result from a simulation that the four hit are assumed to be randomly distributed in the layer. The left panel indicates the result from all the fibers in that layer while the right panel shows a zoomed window of the first 100 fibres.

directly from the decoder after the pedestal subtraction without any cross talk corrections. Although the cross talk corrections do not play a big role in the SFT offline analysis, it is of interest to examine the noise after the cross-talk corrections.

Fig. 5.9 shows the distance of the two neighboring hits from the outer parallel layer. Only the events with four hits have been used here as the integrated hit multiplicity is around 4 from this layer after implementing the threshold cut. The red histogram indicates the distribution from the trigger-29 data; the black one shows the result from a simulation where the four hits are assumed to be randomly distributed in the layer. The left panel of Fig. 5.9 shows this distance distribution from all fibers in the layer while the right panel of Fig. 5.9 shows the result only from the small window of the first 100 fibers. It can be clearly seen that there are bumps around the fiber-1, -8, -15 and -25 due to the uncorrected cross talks from both the PMT surface and fibre layer. According to the feeding scheme of the construction for the SFT from Fig. 5.4, the neighboring channels in the PMT surface are not distributed close to each other [66]. Their locations are 8,15 or 25 fibers apart from the center channel, they are exactly where the bumps stay in Fig. 5.9. The uncorrected effect from the cross talk in the fibre layer causes the bump in the first fiber. Except those uncorrected effect, the distribution from the trigger 29-data and the random simulated one can overlap very well from all other parts.

After the cross talk correction on the PMT surface has been done, the distribution of Fig. 5.9 becomes the distribution as shown in Fig. 5.10. Again the four-hit events are used here. The bumps around fiber 9,15 and 25 disappear while the bump in the first fiber stays

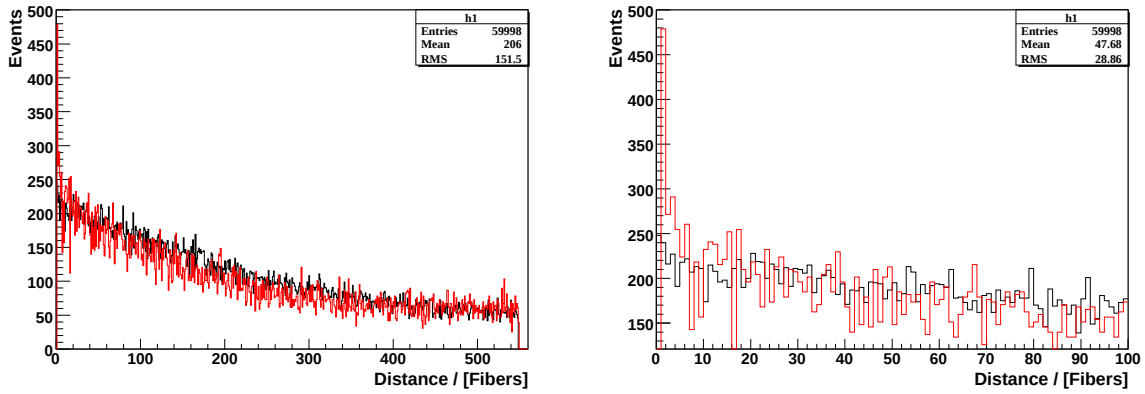

Figure 5.10: The distance of the two neighboring hits after cross talk correction on the PMT surface. The layout of the figure is the same as in Fig. 5.9.

after correction. This indicates the expected effect of cross talk correction.

The cross talk correction for the SFT layer can be performed in addition. Fig. 5.11 shows the distance of the neighboring clusters (bundle of fibres belonging to same hit after the cross talk corrections in the PMT surface and in the SFT layers). The same layout is used here as in Fig. 5.9 and Fig. 5.10. After the cross talk corrections, all the bumps are gone, which may indicate that there exist some real hits instead of electrical noise only in the SFT. However, these real hits seem to locate randomly in the layers, otherwise the data and MC distributions could not overlap so well.

As there are no cross talk corrections in the MC programme, it's necessary to extract the results from the cluster distributions of different layers to construct the noise model. Fig. 5.12 shows the distribution of the noise occupancies at the level of clusters from different SFT layers. These distributions were fitted by the Poisson function. The parameters from the fit functions have been implemented in the MC. Fig. 5.12 a (b) shows the cluster occupancy from the inner parallel (stereo) layers, while Fig. 5.12 c (d) shows the cluster occupancy from the outer parallel (stereo) layers. All these fitting parameters can be found in Table 5.4.

The ADC spectra of the hits can be described by a Gaussian plus a 3rd degree Polynomial function. The parameters can found from Table 5.5. As in the MC there is no cross talk and cluster correction for the SFT and the rPuls in the raw dataSciRec table is the key value for the reconstruction, the ADC values need to be converted into energy loss values. This conversion has been extracted from the PMT calibration [72] and the MIP calibration from the data. For the noise model, a rough conversion of 20 ADC channels to 21e-6 GeV has been used.

In order to implement the random noise model into the MC, the spacepoints have to be confirmed that they are also randomly constructed from the clusters even though all the

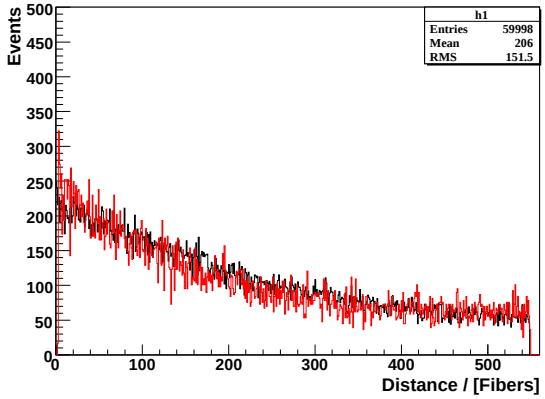

Figure 5.11: The distance of the neighboring clusters (after the cross talk corrections in the PMT surface and in the SFT layers). The same layout is used here as in Fig. 5.9 and Fig. 5.10

Table 5.4: The parameters of the Poisson fitting to the clusters' occupancies of different SFT layers from the background data.

Inn.Para Layer	Inn.Ster. Layer	Out.Para. Layer	Out.Ster. Layer
3.563	3.674	4.695	4.473

Table 5.5: The parameters of a Gaussian plus 3rd Polynomial function to describe the ADC spectra for hits in different layers.

Layer	Height	Mean	Sigma	p0	p1	p2	p3
Inn.Para Layer	1.15e+14	786	126	2715	13.6	0.023	1.3e-5
Inn.Ster Layer	5.42e+14	808	124	2806	14.3	0.025	1.4e-5
Out.Para Layer	6.97e+11	676	126	2047	9.3	0.015	0.8e-5
Out.Ster Layer	3.24e+15	1035	153	2246	10.3	0.016	0.9e-5

clusters are randomly distributed. Fig. 5.13 shows the multiplicity of the spacepoints from the outer SFT. Blue points demonstrate the spacepoint multiplicity from the trigger-21 data while the red points are from the trigger-29 background data. A set of black points is plotted here to indicate the case that the spacepoints of the outer SFT are randomly constructed by the clusters extracted from trigger-29 data. It is clear that though there is difference between the background data and the random distribution model, the difference is quite small compared to the total number of the events. Therefore it seems to be quite safe to implement this random noise model into the MC.

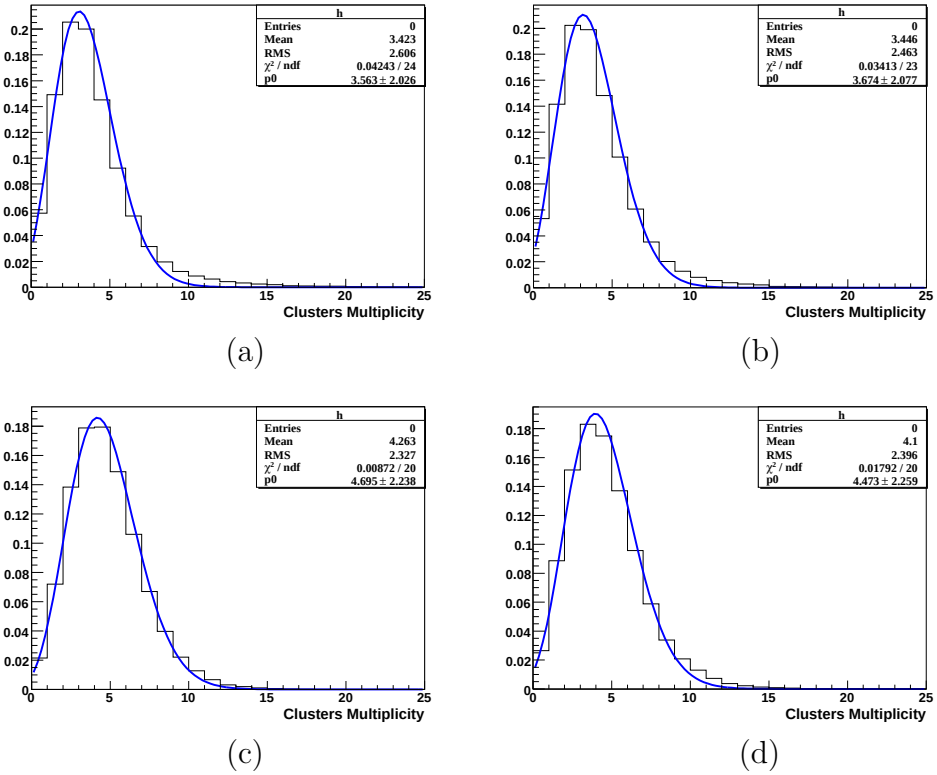

Figure 5.12: The distributions of the noise occupancies in the level of clusters from different SFT layers. These distributions were fitted by the Poisson function. The panel a (b) indicates the noise occupancy from the inner parallel (stereo) layer. The panel c (d) shows the noise occupancy from the outer parallel (stereo) layers.

5.4.3 Conclusions

The noise of the SFT has been measured by triggering the HERMES readout by the HERA-Clock (trigger-29) at the maximum allowable rate. The measurements have been taken under different beam conditions to check the different sources of the noise. The standard analysis has been performed on those dedicated data samples. The occupancy of the noise is strongly correlated with the positron beam current, the occupancy increases when the positron beam current increases. The proton beam seems not to have influence to the occupancy of the background in the SFT. After the cross talk corrections, the hits in the SFT layers seem to have no correlation with each other. Even at the level of spacepoints, the noise seems to randomly locate in the SFT barrel. Based on these rates, a random distributed noise model has been implemented to the Recoil Monte-Carlo programme.

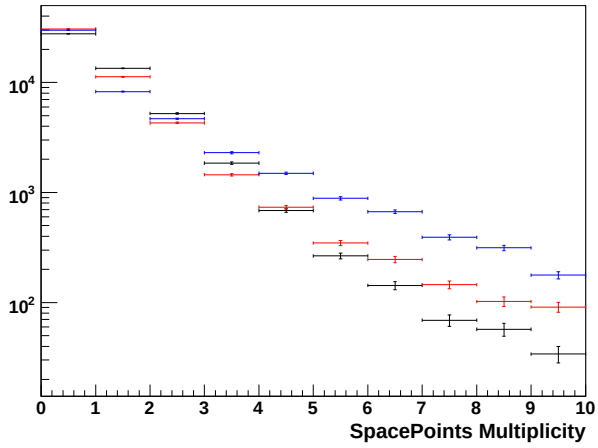

Figure 5.13: The multiplicity of the spacepoints from the outer SFT. Blue points demonstrate the spacepoint multiplicity from the trigger-21 data while the red points are from the trigger-29 background data. A set of black points are plotted here to indicate the case that the spacepoints of the outer SFT are randomly constructed by the clusters extracted from trigger-29 data.

5.5 Calibration of the Energy Response

In order to distinguish protons and pions with the Scintillating Fibre Tracker, the response of the single fibre to the deposited energy from the particles has to be calibrated. This is the second level calibration of the SFT. The first level calibration refers to the step converting the raw ADC values to the number of photo electrons, which is called the PMT gain calibration and has been explained in the previous section. The energy response of the fibres to the traversing charged particles can be described by the Bethe-Bloch formula [79]:

$$-\frac{dE}{dx} = 2\pi N_a r_e^2 m_e c^2 \rho \frac{Z}{A}\frac{z^2}{\beta^2}[\ln(\frac{2m_e\gamma^2\nu^2 W_{max}}{I^2}) - 2\beta^2]. \quad (5.1)$$

The mean energy deposition of the charged particles traversing the materials can be found in Fig. 5.14. The material of our fibres is comparable to carbon. The π mesons with momenta larger than 250 MeV/c can be treated as Minimum Ionizing Particles (MIPs) which deposit constant energy through the materials. For any kind of calibration, constant input signals are always required. In our kinematics the deposited energy of pions are naturally good signals to calibrate the energy response of the fibres. However, unlike silicon detector and photon detector, the SFT doesn't require an absolute calibration for momentum reconstruction. A relative calibration which tunes the signals from the individual fibres to a fixed value without needing the absolute energy loss already meets our requirements.

To make a precise and stable calibration of the energy response from the fibres, a clean

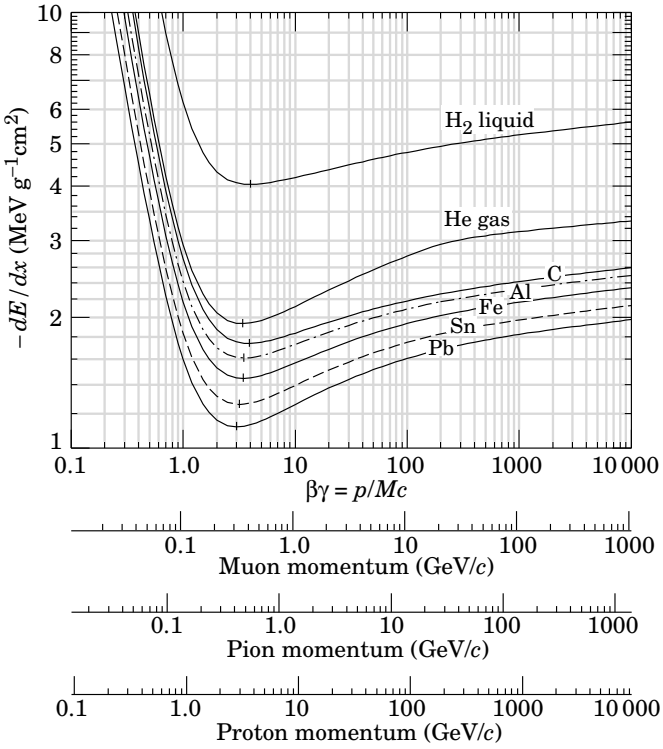

Figure 5.14: Mean energy loss of charged particles for various materials [80]. The energy loss in scintillating fibres is comparable to the carbon curve.

sample of π mesons with proper momenta and enough statistics is essential. In order to exclude ghost tracks as much as possible, only the events with single reconstructed tracks are collected in this work. The π^-s with the momenta less than -200 MeV/c, and the part of the π^+s under the red line in Fig. 5.15 with the momenta larger than 200 MeV/c are used for the calibration. Fig. 5.15 indicates the energy deposition of particles traversing the SFT versus the reconstructed momenta. The points on the left side are from π^- while on the right side a clear separation of protons (upper band) and π^+s (lower hand) can be seen. The red line is a 'hard cut' which separates the protons and π^+s.

So far a data sample with the single reconstructed MIPs has been collected for the calibration. However, ghost tracks still exist in this sample. The left panel of Fig. 5.16 shows the energy deposition from one fibre in the inner SFT layer. The red histogram includes all the events from the reconstructed MIPs in the data sample. The blue histogram only includes the events whose signals from this fibre are the largest signals in the layer. Obviously the red histogram has lightly more small signals than the blue one, which may come from the noise hits, however, in both histograms the peak positions overlap each other in the middle, which is the MIP's position of the fibre. Hits with the largest signals

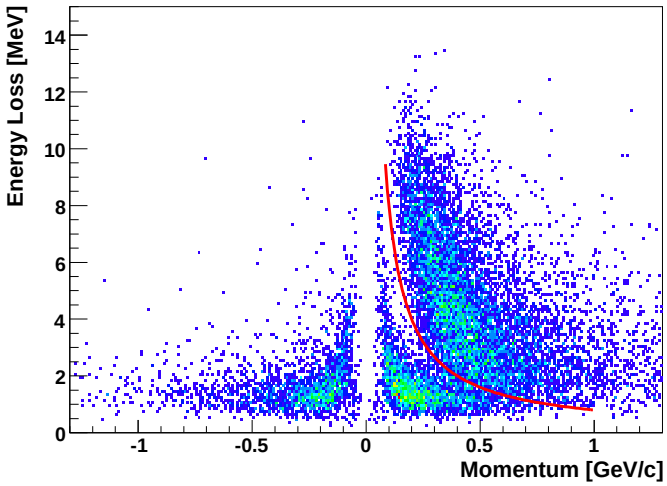

Figure 5.15: Total energy deposition of tracks that go through all SFT layers versus their reconstructed momenta.

of the layer (also called the leading hits) will be used for the calibration. Here, the hits correspond to the signals after the cross talk corrections.

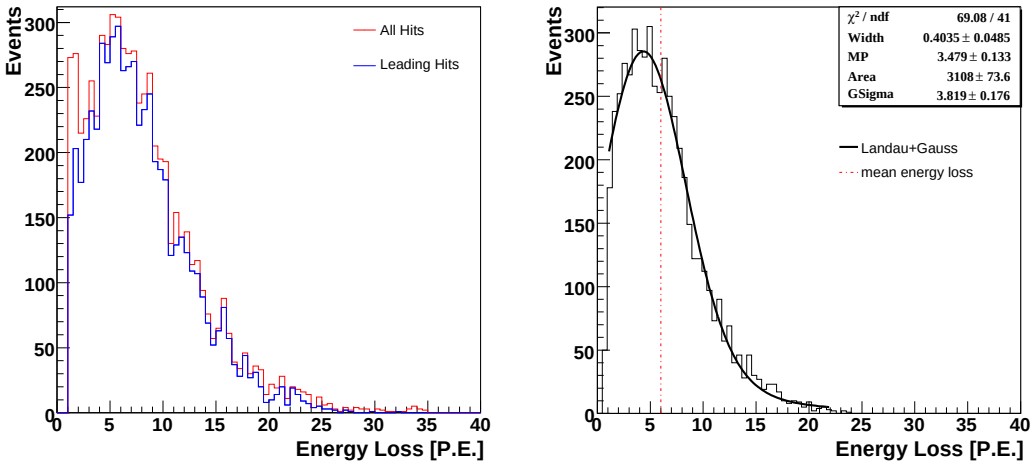

Figure 5.16: Signals of one single fibre from the reconstructed MIPs. The left one indicates the effect of the leading hit selection and the right one shows the MIP distribution of the leading signals with Landau + Gaussian fitting.

To correct the effect from the incident angle θ of the reconstructed tracks, each signal has to be multiplied by a factor of $\sin\theta$. The spectrum of energy deposition from one inner

fibre with the leading signals after the correction of the incident angles is shown in the right panel of Fig. 5.16. The curve is described by the distribution of a Landau convoluted with Gaussian function. The mean value of this spectrum is then recalculated from the fitting parameters and indicated as the vertical line in the figure. This recalculated mean value is considered as the MIP position and used for the relative calibration. The unit in Fig. 5.16 is one photo electron as extracted from the PMT gain calibration.

The same procedure has been executed for all the fibres of the SFT, and the MIP positions of the fibres have been extracted accordingly. In addition, the MIP positions of the fibres have to be normalized to a fixed value layer by layer. These normalization factors from the individual fibres are the relative calibration coefficients for the fibres. Fig. 5.17 shows the fibres' responses to the selected MIPs' sample from the inner most parallel layer (the left panel) and the outer parallel layer (the right panel). The points in the figure refer to the different fibres, and the error bars represent the statistics collected for the corresponding fibres.

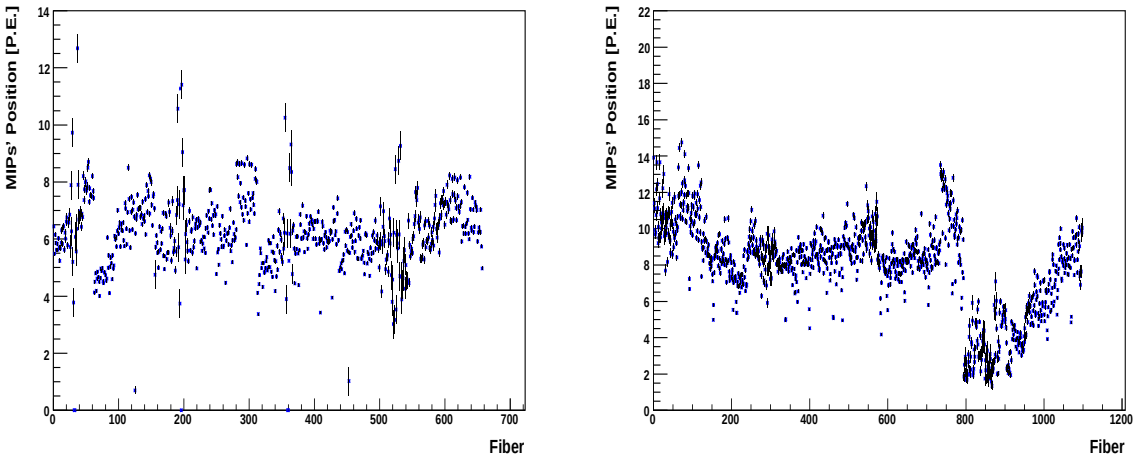

Figure 5.17: Fibre response to the energy deposition of the MIPs flying through the inner most parallel layer (the left panel) and outer parallel layer (the right panel). Effect from the PMT/Lightguide and silicon detector supporting structure can be seen in the left panel. The inefficient part of the outer detector can be seen in the right panel.

The structures of the diagram with the size of fibres around 30 can be observed in the left panel of the figure. This type of structure represents the individual lightguides and mainly come from their bending from the SFT barrel to the PMT readouts. Some of the light gets lost during its traverse when the lightguide is bent. This loss correlates with the radius of the bending of the lightguide. Different lightguides were bent with different radius according to their locations in the experimental region. This effect in the outer SFT barrel is not as big as it is in the inner SFT barrel, which is probably due to the difference

in the construction of the two kinds of the lightguides.

In addition, around the fibre number 18, 193, 360 and 520, there are more fluctuations and bigger error bars. The reason for this is that the supporting structures of the silicon detector are located. These supporting materials stopped the particles flying through and caused the acceptance of the parts in the inner SFT barrel accordingly. While, the corresponding parts in the outer SFT barrel is not affected very much due to the large bending angles of the charged particles between the SFT barrels.

Furthermore, it can be clearly seen from the outer SFT barrel that the fibres between 800 and 960 have much smaller signals and larger error bars compared to the other parts. This part of the outer SFT fibres is found to have a very low efficiency according to a dedicated detector efficiency study [81]. The exact reason for this low efficiency is not clear yet.

Overall, the MIP values from the outer SFT are larger than the ones from the inner SFT, which is understandable as signals from two outer SFT fibres are read out as one signal, whereas one readout channel couples to one fibre for inner SFT barrel.

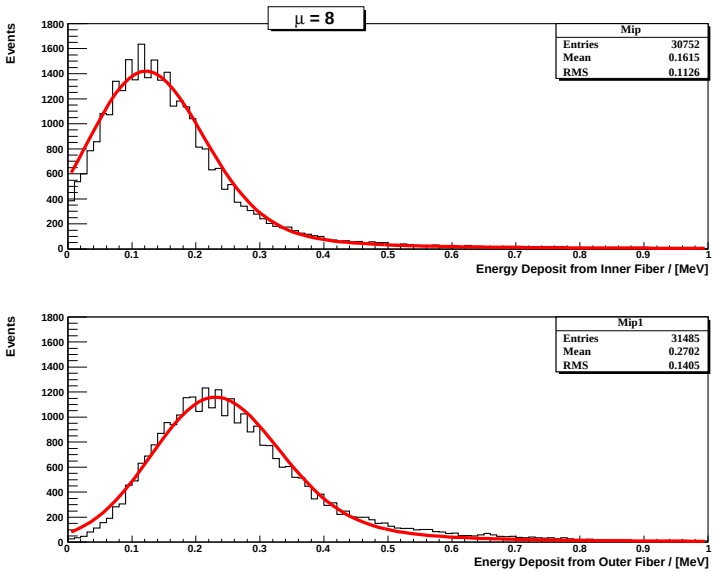

Figure 5.18: Comparison of MIP signals between the real data and the MC. The histograms indicate the responses from the MC and the lines denote these from the real data by using the average values of the fitting parameters from all the fibres.

As mentioned before, to get the calibration coefficients, the energy responses from different fibres have to be normalized to a certain fixed value. This was done by the Monte Carlo simulation after implementing the reasonable digitization algorithms of the fibres to the HERMES detector simulation programme HMC. Fig. 5.18 shows the comparison of the MIPs between the real data and the MC. The same cuts for the data are required here

to select the MIPs' sample. The histograms indicate the responses from the MC and the lines are from the real data by using average values of the fitting parameters from all the fibres. The number of photo electrons for the MIPs in the inner and outer SFT is listed in Table 5.6. One photo electron is assumed to be $2.58 \cdot 10^{-6}$ GeV for the conversion of the absolute energy to the photo electron in MC.

Table 5.6: The fixed number of photo electrons of the MIPs from MC.

	Inner SFT barrel	Outer SFT barrel
Number of Photo Electrons	6.1	9.6

The signals of the MIPs from all the fibres are then normalized to the two fixed values for the inner and outer SFT barrel separately. The normalization factors for the individual fibres are the so-called relative calibration coefficients. Fig. 5.19 shows the MIPs' signals from inner most parallel (the left panel) and outer parallel layers (the right panel) after correcting the raw signals with the calibration factors fibre by fibre. A data sample used here was collected from different time periods compared to that used to extract the calibration factors. No lightguide structures can be seen now from either of the layers. The corrected signals have low correlations to each other and tend to be a flat distribution. In the inner layer, there are large fluctuations in the regions where the silicon supporting structure is located due to the low statistics. In the outer layer, fluctuations can be seen in the low efficient parts for the same reason. Except these particular parts, the relative calibration works well and the corrected signals are under control.

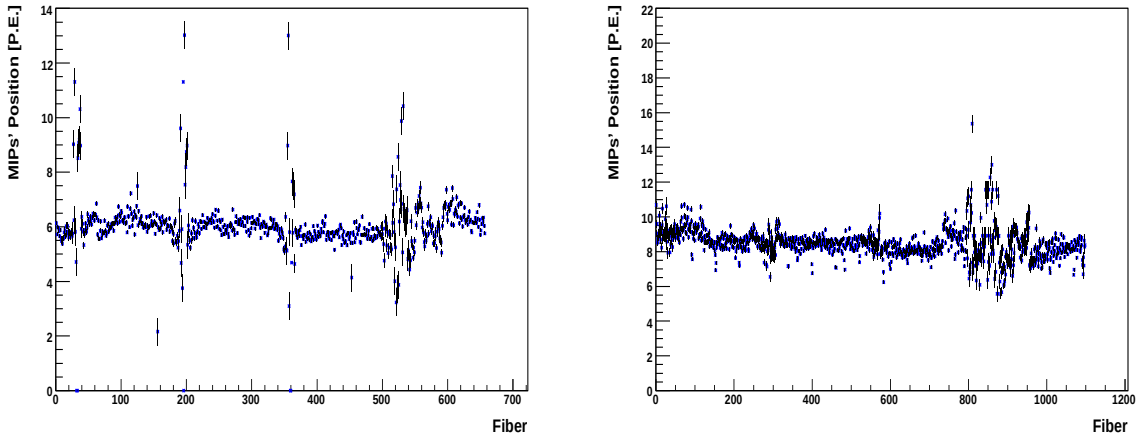

Figure 5.19: shows the corrected fibre response to the energy deposition of the particles flying through the inner most parallel layer (the left figure) and outer parallel layer (the right figure).

There are still two items to be considered and checked for this calibration. First, it

is essential to check the timing dependence of the fibre response and the stability of the calibration, as any kind of particle identification needs a stable input signal or at least a corrected stable input signal. During the calibration study of the 2007 data, the data was divided into 13 parts, each containing the similar number of statistics. Thus the detector can be calibrated from different times. The left panel of Fig. 5.20 shows a 3-dimensional plot of the energy response from the inner SFT layer versus the different time periods and the fibre numbers. Where the signals were corrected by a list of dummy calibration factors. It is clear from the figure that there is almost no time dependence of the fibre responses.

The particles can interact at the different positions along the longitudinal direction in the target which is also the beam direction. The right panel of Fig. 5.20 demonstrates the MIPs' values from the inner layer versus the longitudinal vertex position. The error bars here indicate only the collected statistics. Most of the statistics locate from 14 cm to 25 cm due to the acceptance of the recoil detector and the location of the target cell. This distribution can be considered as a flat distribution, which excludes a z-dependence of the fibre signals.

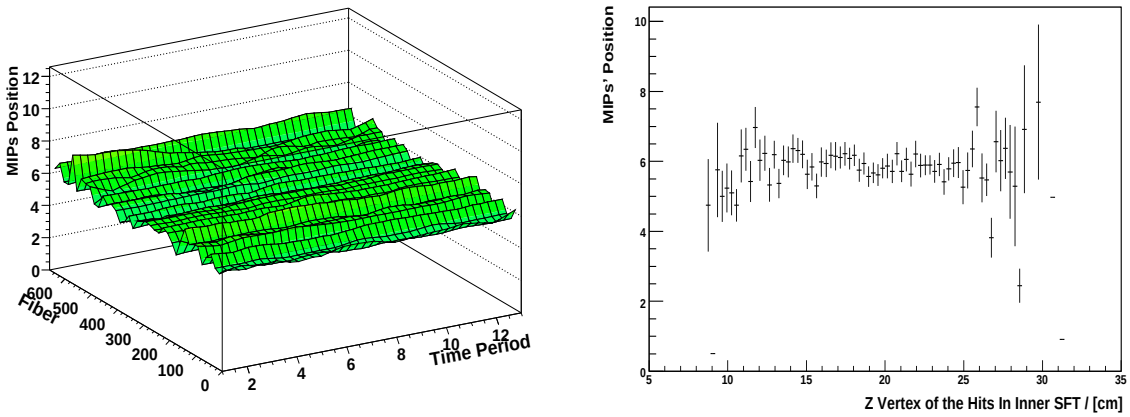

Figure 5.20: Stability of the MIPs (left panel) and a z-dependence of the MIPs' values (right panel).

5.6 The Particle Identification

The energy depositions from the charged particles provide a method to distinguish protons and pions in the Recoil Detector. Particle identification (PID) of the SFT can be carried out in certain momentum ranges using the calibrated signals. Using additional information from the silicon detector and the photon detector, the Recoil Detector is able to distinguish protons from pions in the momentum range between 200 and 800 MeV/c [27]. In the following section, a brief introduction will be given for the principles of the particle identification, followed by the discussion of the PID of the SFT.

5.6.1 The Scheme of the Particle Identification

The particle identification is performed by using the conditional probability method [59,82]. The principle idea of this method is to calculate the probability that a measured detector response X was caused by a particle type A and to compare it with the probability caused by another particle type, this probability is written as $P(X|A)$. To calculate this probability, we first have to know the probability that a particle of type A causes the detector response X, $P(A|X)$. The two probabilities can be compared with each other. The relation between the two probabilities can be first clarified by assuming that there is only a single particle type A and a single particle identification detector. A distribution $p(X)$ can be defined as the probability to obtain the signal X from the detector. The integral to all the probabilities of this distribution is unity. The probability $P(A|X) = p(X)$ is given by this probability distribution, in addition, we have $P(X|A) = 1$ as there is only one particle type in this case.

When there are several particle types A_i being measured by the detectors, the probability $P(A_i|X)$ is still given by the normalized detector response, but the probability to observe that a particle A_i causes the detector response X becomes $P(A_i) \cdot P(A_i|X)$, where $P(A_i)$ is the probability that the observed particle is of type A_i. $P(A_i|X)$ is now called a conditional probability, because it is a probability under the condition that the particle is of type A_i. The probability $P(A_i)$ is in particle physics terminology referred to as the flux factor ϕ^i of the particle type A_i.

For several particle types A_i, the probability $P(X|A_i)$ is given by Bayes' theorem [80,83]:

$$P(X|A_i) = \frac{P(A_i) \cdot P(A_i|X)}{\sum_j P(A_j) \cdot P(A_j|X)}, \tag{5.2}$$

which takes the flux factors properly into account. The flux factor is normally dependent on the momentum p and the incident angle θ.

The conditional probability can also be called parent distribution $\mathcal{L}_D^i$ which is the response of the detector D was caused by a particle of the type i. The parent distribution can be extracted by using the distribution from the test beam data or from clean particle samples obtained with restrictive hard cuts on the other PID detectors in the experiment.

These distributions are normalized and either used directly or by fitting with an analytical function. During the calculation of the conditional probability, the parent distributions from different detectors can be combined together

$$\mathcal{L}^i = \prod_D \mathcal{L}^i_D. \tag{5.3}$$

So the probability of a particle of the type i is

$$\mathcal{P}^i = \frac{\phi^i \mathcal{L}^i}{\sum_j \phi^j \mathcal{L}^j}. \tag{5.4}$$

There are only two particle types, proton and pion in the Recoil Detector, therefore the their probabilities can be written as [84]

$$\mathcal{P}^\pi = \frac{\mathcal{L}^\pi}{\Phi \mathcal{L}^p + \mathcal{L}^\pi}, \tag{5.5}$$

and

$$\mathcal{P}^p = \frac{\mathcal{L}^p}{\mathcal{L}^\pi/\Phi + \mathcal{L}^P}, \tag{5.6}$$

where only the parent distributions and the flux ratio $\Phi = \phi^p/\phi^\pi$ have to be known. Normally in the data analysis, a more intuitive PID parameter can be created by taking the logarithm of the ratio of the pion and proton probabilities

$$PID = \log_{10}(\frac{\mathcal{P}^p}{\mathcal{P}^\pi}) = \log_{10}(\frac{\Phi \mathcal{L}^p}{\mathcal{L}^\pi}) = \log_{10}(\frac{\mathcal{L}^p}{\mathcal{L}^\pi}) + \log_{10}\Phi, \tag{5.7}$$

where the $PID = 0$ represents the case that a particle is equally likely to be a pion or a proton and naturally an ideal value to cut. Equal fluxes are often assumed, when the PID from a single detector is calculated the flux factor is ignored

$$PID_D = \log_{10}(\frac{\mathcal{L}^p_D}{\mathcal{L}^\pi_D}). \tag{5.8}$$

The PID value including the flux factor for the whole recoil detector can be written as

$$PID = \sum_D PID_D + \log_{10}\Phi. \tag{5.9}$$

5.6.2 The Parent Distributions

The Recoil Detector has three sub-detectors and each sub-detector has a certain number of sub-layers, so the whole recoil PID will be done by combining all the information from these 3 sub-detectors [27]. The Silicon detector provides 2 PID values from the inner and outer

detectors separately and the photon detector will give three PID values from the three sub layers. The SFT will have four PID values instead of two as of the silicon detectors. The four PID values are separately from inner parallel layer, inner stereo layer, outer parallel layer and outer stereo layer. The reason that the SFT PID is done in the sub-layer level is to reduce the systematic uncertainties for the PID, which mainly come from the calibration uncertainties of different PMTs.

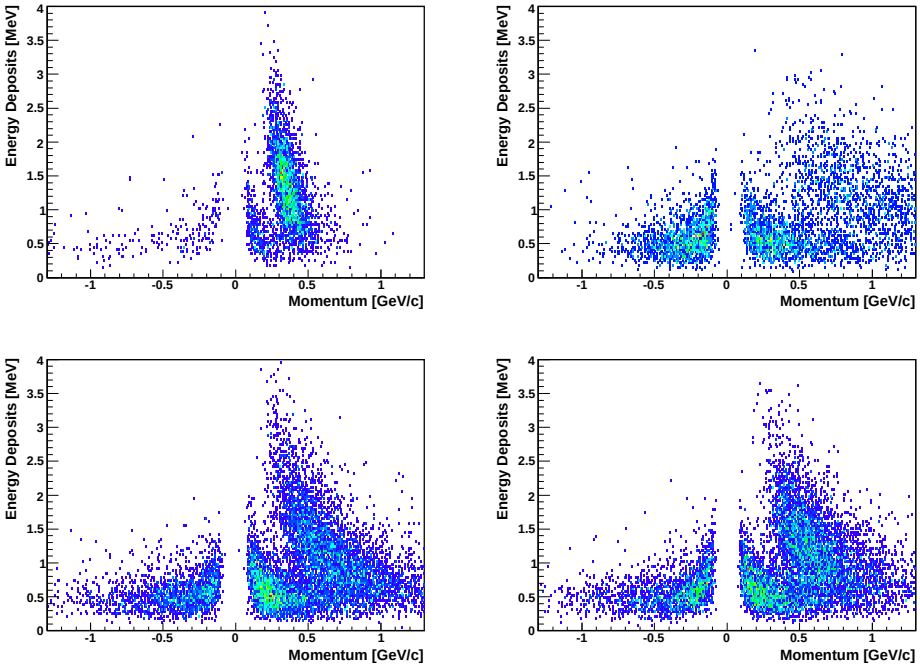

Figure 5.21: Energy depositions from the charged particles which pass through all the SFT layers versus their reconstructed momenta. Different panels represent the results from different quadrants, the upper left (right) indicates the first (second) quadrant while the bottom left (right) indicates the third (fourth) quadrant.

Based on the previous scheme, four parent distributions need to be generated for the SFT PID calculation. However, due to a small misalignment of the recoil detector and some miscalibration features from the silicon detector, the momentum reconstruction from different quadrants has different behaviour, hence the distributions of the energy depositions change quadrant by quadrant accordingly. The quadrant dependent distributions of the energy deposition challenge the extraction of the parent distributions and the PID calculation. Fig. 5.21 shows the energy depositions versus the reconstructed momenta from 4 different quadrants. The upper left (right) indicates the first (second) quadrant while the bottom left (right) indicates the third (fourth) quadrant. It can be clearly seen in the figures that the shapes of the proton and pion bands in the four quadrants are different,

and in the second quadrant fewer protons can be reconstructed which results from inefficiencies of both the silicon and the fibre detectors. According to these features, the parent distributions are also generated based on the quadrant level. So far, 16 parent distributions have to be generated for the scintillating fibre tracker. The idea to make so many parent distributions is to resemble the detector as much as possible and to proceed the upcoming PID calculation in a common way without considering too much hardware details.

The parent distributions of the Recoil Detector were generated by collecting a clean data sample from the real data. In order to select the clean data sample for a certain sub-detector, some 'hard cuts' have to be imposed on the other sub-detectors. Normally the parent distributions are generated from test beam data or even from Monte Carlo simulation. However, extraction from the real data is also allowed, as the correction of the flux factors from the real data will eliminate the kinematic bias in the PID system. The reconstructed charged particles with four spacepoints (two from the silicon detector and the other two from the fibre tracker) are first required to be candidates for the clean sample. Then a set of very strict cuts is implemented to the energy responses and momenta on the silicon detector to select the clean proton and π^+ sample. The responses of the fibre tracker to these particles will be used as the parent distributions. Fig. 5.22 shows the energy depositions in the SFT from the selected protons (left panel) and π^+s (right panel). Both figures show clean bands with very few statistics outside of the band. Based on this fact, this clean data sample can be safely used to extract the parent distributions.

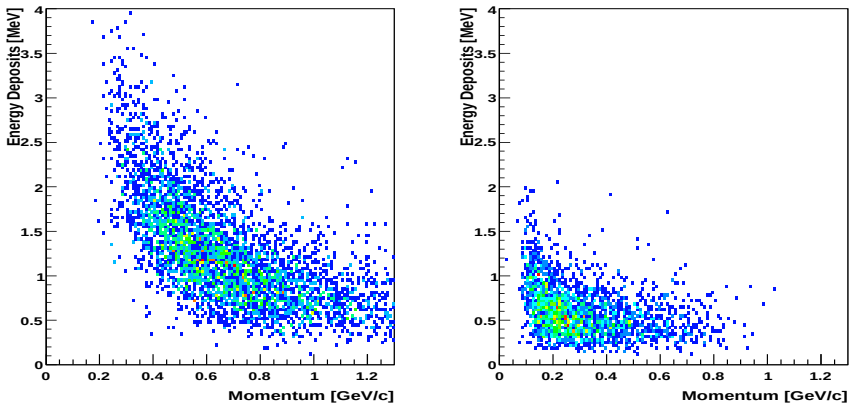

Figure 5.22: Energy deposition of the selected protons (left panel) and π^+'s (right panel) that go through all SFT layers versus their reconstructed momenta.

As the energy response in the recoil kinematics varies in a big range depending on the momenta, it is essential to make the parent distributions in different momentum bins. The principle of the selection of the momentum bin is: firstly the signal should keep constant inside the momentum bin; secondly the number of bins used should be as small as possible

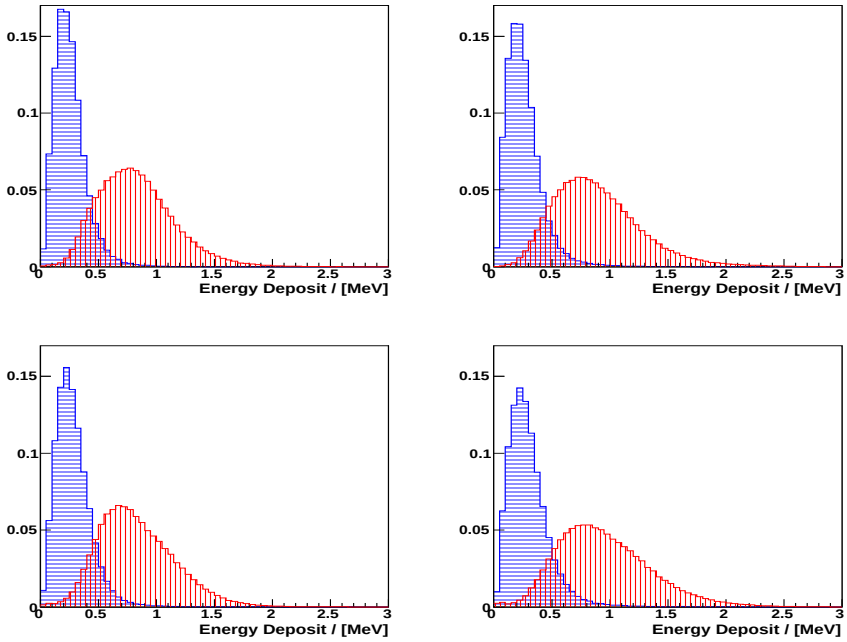

Figure 5.23: The parent distributions in the momentum bin of [400, 500] MeV/c. The four panels represent the four layers. The area filled with the vertical (horizontal) lines indicates the pion (proton) parent distributions.

for the parent distributions. In the momentum below 1 GeV/c, 9 momentum bins were used. The width of the first bin is 200 MeV/c, while 100 MeV/c is used for the other bins. The first momentum bin covers the momentum from 0 to 200 MeV/c, where most of the protons with such low momentum already stop in the silicon detector, very few protons can penetrate or even reach the fibre tracker. In principle, the particles detected with SFT in this momentum bin are supposed to be pions. For completeness, we still keep this bin in generating the parent distributions but the quality of the parent distributions will be lower as very few protons can be found in this momentum bin. Fig. 5.23 shows the parent distributions of the third quadrant in the momentum bin from 400 MeV/c to 500 MeV/c. The four panels represent the four layers. In each panel, the vertically shaded area indicates the energy response from the pions, while the horizontally shaded area indicates the energy response from the protons. The separation between the two distributions is good even in the single layer.

The SFT PMT has a limited kinetic range to record the signals. Large signals from the slow protons may saturate the PMT readout. When the saturation happens, no useful number for the pulse height of the signal can be recorded by the detector readout. Only the channel information can be read out. These hits are called the overflow hits. Special

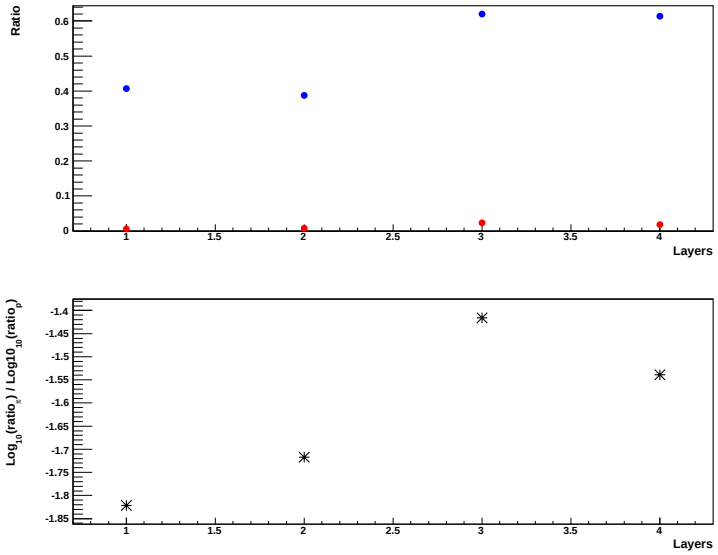

Figure 5.24: Parent distributions from the overflow hits of the third quadrant in the momentum bin from 400 MeV/c to 500 MeV/c. In the upper panel, the blue (red) points indicate the possibilities to find an overflow hit from the proton (pions) in the different four layers. The logarithms of the ratios between the two numbers are put in the lower panel as the PID from the overflow hits for the four layers separately.

treatment has to be implemented to this type of hits to extract the corresponding parent distributions. The principle of the parent distribution is to extract the probability to find a particle type in certain kinematic bins of the observable. For the case of overflow hits, the ratio of the number of overflow hits to the number of non-overflow hits is an observable, which is useful for PID. Unlike the energy depositions which always have a continuous distribution, this observable of the overflow ratio has only discrete values. In the SFT PID scheme, one quadrant of one layer has only one value, but this point will provide additional information for the PID calculation. The slow protons have larger energy loss, they have larger possibilities to exceed the PMT kinematic limit and yield overflow hits in the readout. The pions are the MIPs and generate the overflow hits in the PMT readout very rarely. From this point of view, even there is only one additional point in the parent distribution, this will help to improve the particle identification in SFT.

Fig. 5.24 shows the parent distributions from the overflow hits of the third quadrant in the momentum range from 400 MeV/c to 500 MeV/c. In the upper panel, the blue (red) points indicate the possibilities to find an overflow hit from the proton (pions) in the different four layers. The logarithms of the ratios between the two numbers are put in the lower panel as the PID value from the overflow hits for the four layers separately.

So far the SFT PID has two parts: the part from the non-overflow hits and the part

from the overflow hits and can be described as:

$$PID_{SFT} = PID_{SFT}^{non-overflow} + PID_{SFT}^{overflow}. \tag{5.10}$$

Together with the PID from the silicon detector, a PID observable can be formed to identify the recoil particles. Fig. 5.25 shows a 3 dimensional distribution of PID versus the reconstructed momenta for the positive charged recoil particle. Two peaks (one for the proton and the other one for the π^+ as indicated in the figure) can be clearly seen and are separated very well in the low momentum region.

This PID scheme was implemented in the 07c1 μDST production and used for the physics analysis in the next chapter. The contamination and efficiencies of the PID are still under study and final results will come out soon [85]. Finally the appropriate flux factors have to be included to improve the quality of the PID furthermore.

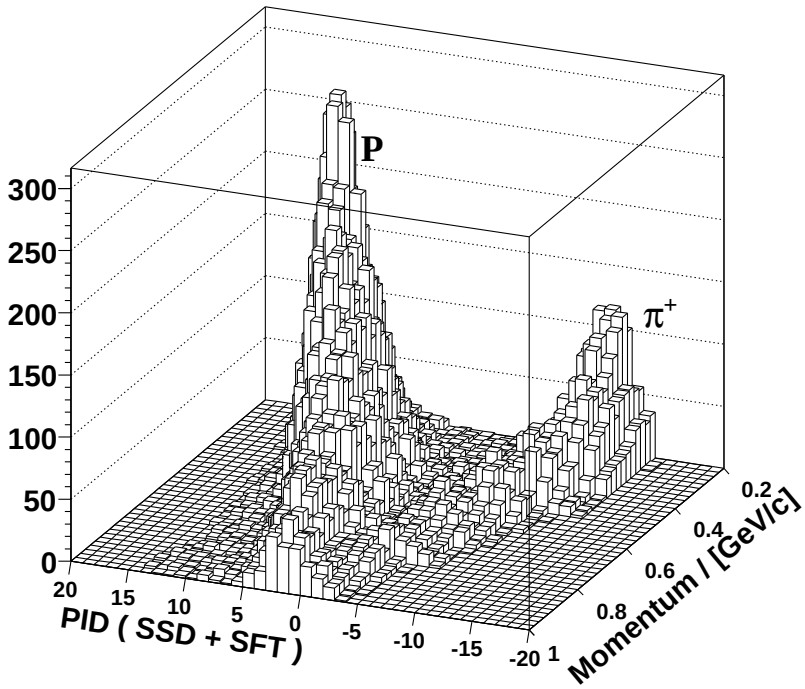

Figure 5.25: The three dimensional distribution of PID versus the reconstructed momenta.

Chapter 6

The Data Analysis

In the years 2006-2007, the HERMES experiment took data with the Recoil Detector using unpolarized hydrogen and deuterium targets. In the first half year of 2006 HERA ran with the electron beam, the silicon detector didn't work due to a serious radiation damage [86]. The silicon detector was repaired and reinstalled along with an improved target cell in July 2006. Since then only the positron beam had been filled in the HERA lepton storage ring.

The Recoil Detector provides exclusive measurements by directly detecting the recoil particles. The data taken with the Recoil Detector has been calibrated. The recoil particles were reconstructed using sophisticated tracking methods. A Monte Carlo programme has also been developed for the Recoil Detector. However, these developments of the offline data processing have not been finalized, especially the complete understanding of the detector and the implementations of certain detector features to the MC require further studies.

In the following parts, we will focus on the particles reconstructed by the silicon detector and the fibre tracker to perform first DVCS studies. The 07c1 μDST production of the positron beam is used for this work. The data taken in 2006 will not be included in this work as it has not been calibrated yet. The Beam-Helicity Asymmetry (BSA) of the positive beam charge will be extracted both from the elastic BH/DVCS process, and from the associated BH process via the decay channel: $\Delta^+ \rightarrow n\pi^+$. This extraction will be performed only from the data taken with the hydrogen target. Finally, very preliminary results will be presented.

6.1 Kinematic Definitions

Most of the kinematic variables have been introduced in the previous chapters for the BH/DVCS processes. Further regarding the additional information from the Recoil Detector, some additional kinematic variables have to be defined.

Due to the limited acceptance of the forward spectrometer, the exclusive measurement of the BH/DVCS processes relied completely on the missing mass technology, through the

missing mass squared distribution M_x^2,

$$M_x^2 \equiv (k + P - k' - q'), \tag{6.1}$$

where $k(k')$, P, and q' have been defined in the previous chapters and denote the four-momentum of the initial (final) positron, the target proton, and the real photon respectively. The M_x^2 can be expressed in the laboratory frame for the hydrogen target as

$$M_x^2 = m_P^2 + 2m_P(\nu - E_\gamma) - Q^2 - 2E_\gamma(\nu - \sqrt{\nu^2 + Q^2}cos\theta_{\gamma\gamma^*}). \tag{6.2}$$

It is a very useful quantity to extract the exclusive processes in the HERMES experiment, independent of whether the recoil protons can be directly detected or not.

In the case the recoil proton was detected by the Recoil Detector, the quantity of squared momentum transfer to the target t can be directly measured as follows:

$$t_{rd} = 2m_P(m_P - \sqrt{p'^2 + m_P^2}), \tag{6.3}$$

where m_P is the rest mass of the target proton and $p^{'}$ denotes the three momentum of the detected recoil proton.

6.2 Data Selection

In this section the data selection will be introduced based only on the forward spectrometer, similar to the traditional HERMES DVCS studies [53]. The data selection relating to the Recoil Detector will be addressed in the next sections.

6.2.1 Data Quality

The analysis is performed for the 07c1 μDST production with the proton target. To avoid including the problematic bursts into the data sample, the following data quality cuts are used during the data selection [87].

- the beam polarization was reasonable
  $20 <$ g1Beam_rPolFit < 80
- the dead time of the DAQ was reasonable
- the burst length was reasonable
  $0 <$ g1DAQ_rLength ≤ 11 s
- the beam current was reasonable
  $2 \leq$ g1Beam_rMdmCurr ≤ 50 mA
- the luminosity was reasonable
  $10 \leq$ g1Beam_rLumiRate ≤ 2500
- the burst was not the first one in a run

- the burst had no bad μDST records
- the PID was available
- the burst was in a run marked as analyzable in the online logrun file
- the Recoil Magnet was on
- DAQ information was available
- no dead blocks in the calorimeter
- no dead blocks in the pre-shower or luminosity monitor
- TRD was not marked as bad
- no High-Voltage trips in the tracking chambers
- the latest beam polarization measurement was less than 5 minutes interval
- the DAQ dead time was in the range
  $0.5 \leq$ g1DAQ_rDeadCorr21 ≤ 1.0

Finally all these items can be translated into a badbits pattern as: badbits & 0x501e13fe = 0.

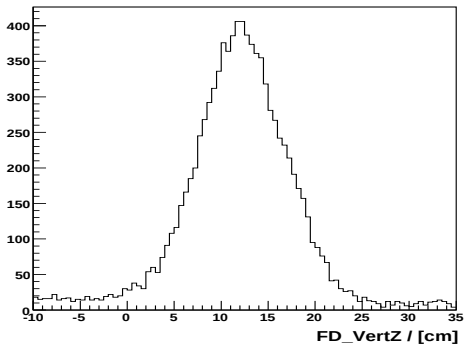

Figure 6.1: Distribution of the reconstructed longitudinal vertices z_{vtx} from the forward spectrometer.

6.2.2 DIS Data Selection

A DIS sample should be preselected to serve the purposes of the exclusive selection and the data-MC normalization. The selection rules for the DIS events are as following:

1. trigger 21 was fired
   smTrack.bTrigMask & (1 << (21-1));
2. each event contained at least one track that satisfied
   - identified as a positron
     g1Track.rPID2 + g1Track.rPID5 > 2
   - selected as a long track
     !(g1Track.iSelect&0x0100) && !(g1Track.iSelect&0x0200)

- longitudinal vertices of the tracks inside the target cell
  $5 <$ g1Track_rVertZ < 20 cm, (compare Fig. 6.1).
- transverse vertices of the tracks in a small region
  |g1Track_rVertD| < 0.75 cm
- tracks passing through the calorimeter
  $|x^e_{calo}| < 175$ cm, $30 < |y^e_{calo}| < 108$ cm
- fiducial volume cuts for the tracks
  |smTrack.rxOff + 172·tanθ_x| < 31 cm
  |smTrack.ryOff + 181·tanθ_y| > 7 cm
  |smTrack.ryOff + 383·tanθ_y| < 54 cm
  |smTrack.rXpos + (383-275)·smTrack.rXslope| < 100 cm
  |smTrack.rYpos + (383-275)·smTrack.rYslope| < 54 cm

3. each event passes the following kinematics cuts
   - $W^2 > 9$ GeV^2, $Q^2 > 1$ GeV^2, $\nu < 22$ GeV.

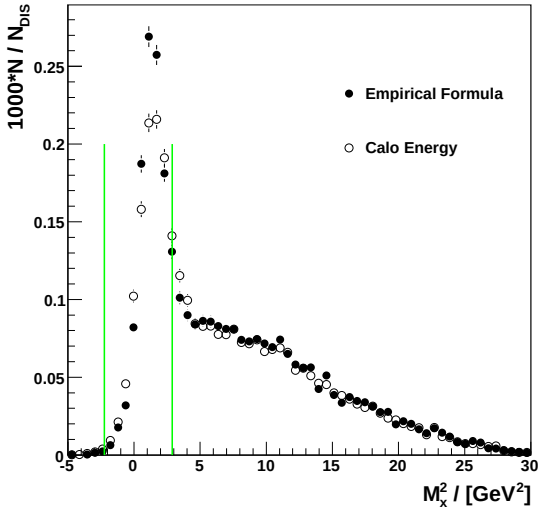

Figure 6.2: The distributions of the missing mass squared M_x^2 of the BH/DVCS events, they are selected by the forward spectrometer with all the standard DVCS cuts. The photon energy is either taken from the calorimeter (open circles) or calculated with the empirical formula combining the both signals from the calorimeter and the preshower detector (solid circles). The two vertical lines indicate the exclusive window.

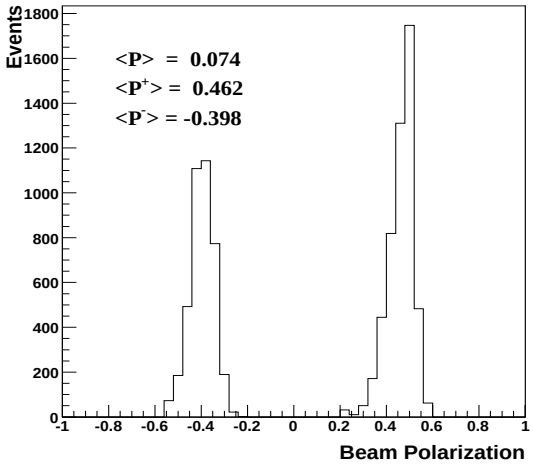

Figure 6.3: The beam polarization from the 2007 positron beam data.

6.2.3 Exclusive Data Selection

The exclusive selection starts by requiring exactly one track and exactly one untracked cluster as a photon in the calorimeter from each event.

The angle between the real photon and the virtual photon $\theta_{\gamma\gamma^*}$ is demanded between 5 mrad and 45 mrad to remove background. In addition to the DIS selection, a strict kinematic boundary is imposed on the data as $0.03 < x_B < 0.35$ and $Q^2 < 10$ GeV^2. The constrained invariant momentum transfer to the target proton t_c is required to be larger than -0.7 GeV^2.

The signals left in the calorimeter from the photon should be above 5 GeV to significantly remove the non-exclusive events. The energy loss from the photon in the preshower detector is required to be more than 1 MeV to improve the resolution of the energy measurement in the calorimeter. The resolution of the reconstructed photon energy drops significantly for the photons which didn't start showering in the preshower detector, hence it will deteriorate the resolution of the missing mass and the exclusive measurement. When the photons hit the blocks in the edge of the calorimeter, the deposited energy can not be completely measured, this will affect the resolution of the missing mass. To avoid this effect the photons are asked to be located in the following region: $|x^{\gamma}_{calo}| < 125$ cm, $33 < |y^{\gamma}_{calo}| < 105$ cm. This set of the cuts is called the photon geometry cut.

An empirical formula combining the response from the calorimeter and the preshower detector together to calibrate the E/P close to 1 is used to calculate the photon energy in this work [88]:

$$E_{\gamma} = E_{calo}(0.949861 + 0.255836E_{preshower}) + 11.24062E_{preshower} \tag{6.4}$$

where the E_{calo} and $E_{preshower}$ represent the energy loss of the photon in the calorimeter and the pre-shower detector respectively. Fig. 6.2 indicates the effect to the missing mass squared after making use of this new formula to calculate the photon energy. All the previous cuts related to the forward spectrometer have been implemented here. In the figure the solid circles show the missing mass squared when the new formula is used, the photon energy taken directly from the calorimeter is represented as the open circles. By using this formula around 6% of the yields can be gained in the exclusive region, while the missing mass peak position does not change and its width becomes slightly narrower.

All the events from Fig. 6.2 are called exclusive candidates. While the events inside the exclusive window are the exclusive events from the BH/DVCS process. The exclusive window is kept between -2.25 and 2.89 GeV^2 in this work. Once the data taken with the Recoil Detector is better understood, it will be tuned for final analysis. A distribution of the beam polarization from the bursts containing the DVCS candidates is indicated in Fig. 6.3. This beam polarization has a positive net polarization with a value of around +7%. The uncertainty of the beam polarization measurement is around 4%.

6.3 Monte Carlo Simulation

Monte Carlo (MC) simulation is proven to be a unique and very useful tool in the experimental particle physics to understand the detectors and the data. In the previous HERMES DVCS studies various types of MC simulations were used to understand the backgrounds, to estimate the systematic uncertainties and to make data-theory comparison. There the BH/DVCS processes and the background processes are simulated by three MC generators: gmc_dvcs, gmc_disNG, and gmc_exclpion.

The gmc_dvcs [61] generator provides simulations of the elastic BH/DVCS and associated BH processes. The unpolarized cross section for the elastic BH process is calculated using the Mo-Tsai formalism [89]. Five different models are used to calculate the cross section for the DVCS process [51]. The associated process for the resonance states is also simulated in the gmc_dvcs generator. Its total cross section is calculated using the Brasse parameterization for the inclusive cross section $\sigma(\gamma^* p)$ in the resonance region measured at SLAC [90]. The main contributions to the total cross section are from single-meson decay channels: $\Delta^+ \rightarrow p\pi^0$ and $\Delta^+ \rightarrow n\pi^+$, and they are modeled according to the MAID2000 model [91]. The remaining contribution is assigned to multi-meson decay channels ($\Delta^+ \rightarrow p\pi^0\pi^0$) according to isospin relations.

The gmc_disNG generator is used to simulate the semi-inclusive DIS for the background processes of the DVCS studies. This generator is extended from the lepton-production generator LEPTO [92] to simulate polarized DIS processes. The fragmentation and decay of unstable particles are simulated with JETSET based on the LUND string model [93] and optimized for energies relevant to HERMES. RADGEN is also included into the gmc_disNG to simulate the radiative processes such as the elastic BH process.

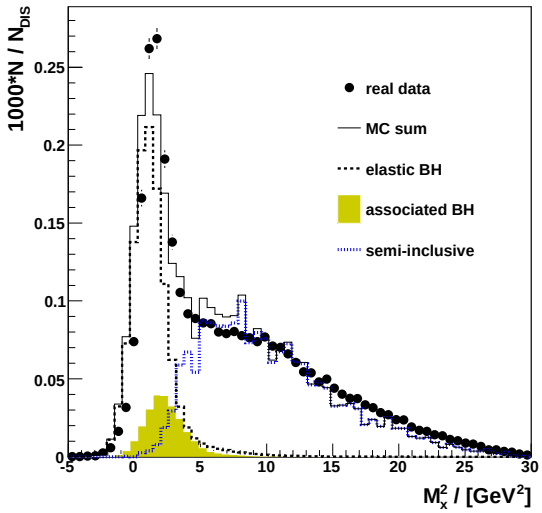

Figure 6.4: Comparison between the absolutely normalized M_x^2 distributions from the MC simulation (solid line) and from the experimental data (solid circles). Also shown are individual contributions from elastic BH process (dashed line), associated BH process (shaded area), and semi-inclusive processes (dotted line).

The gmc_exclpion generator simulates production of exclusive pions. The contribution to the background from exclusive pions is found to be small and thus is neglected in this analysis [53].

In this work only the MC productions generated by the gmc_dvcs and gmc_disNG are used. The detector simulation is done by the HERMES Monte Carlo (HMC) program, which uses GEANT3 package to simulate the passage of particles through detectors. Much progress has been achieved over the last years to extend the HMC for the simulation of the Recoil Detector. However, the work regarding to the MC is still not completed, such as the implementation of detector efficiencies to the MC production. This plays an important role in the data-MC comparisons to successfully understand the physics results.

In the previous DVCS analyses, the calorimeter was found not to be properly modeled for the calculation of the photon energy in HMC. Hence the simulated photon energy is smeared according to the calorimeter resolution:

$$\frac{\sigma(E)}{E}[\%] = \frac{5.1 \pm 1.1}{\sqrt{E(GeV)}} + (2.0 \pm 0.5) + \frac{10.0 \pm 2.0}{E(GeV)} \tag{6.5}$$

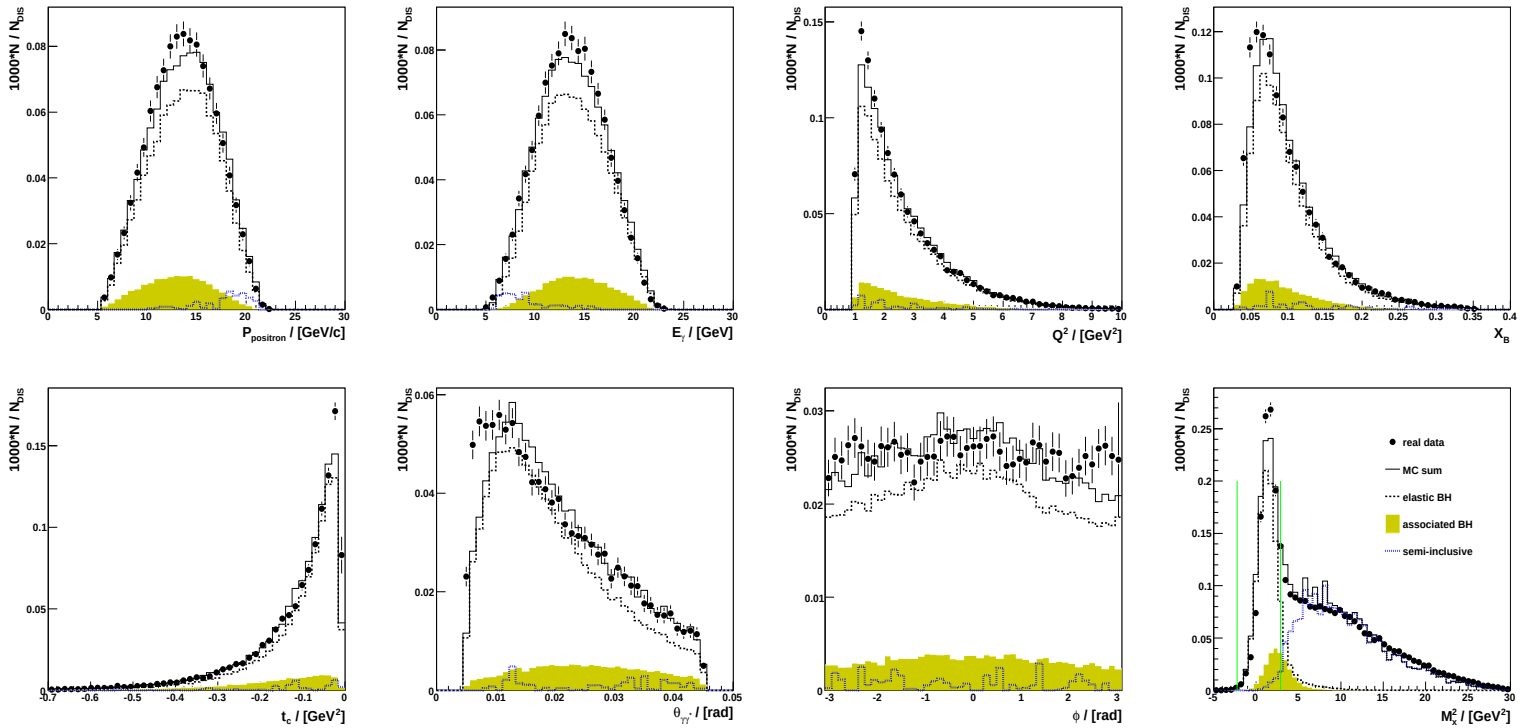

Figure 6.5: Comparison between the MC simulation (solid lines) and the experimental data (solid circles) in the exclusive region -2.25 $<$ Mx^2 $<$ 2.89 GeV^2. The exclusive region is indicated by the two vertical lines in the missing mass squared figure. The MC simulation is performed without including the DVCS process. Due to the usage of the new formula to calculate the photon energy in the data, the data overshoots the MC in the exclusive region. Also shown are individual contributions from elastic BH process (dashed line), associated BH process (shaded area), and semi-inclusive processes (dotted line).

In Eq. (6.5) E is the generated photon energy in MC. It is known that the photon energy is very sensitive to the missing mass squared distribution at HERMES. Fig. 6.4 shows the comparison of the M_x^2 distributions between MC (solid line) and data (solid circles), both the MC and the experimental yields are normalized to the total DIS numbers respectively. The photon energy in MC was calculated according to Eq. (6.5) while in data it is calculated based on the empirical formula Eq. (6.4). The contributions from different physics processes in MC can also be found in the figure. In the exclusive region the data overshoots a bit to the MC due to the usage of the new empirical formula. While in the previous DVCS studies, the MC had a bit higher yield than the data for the exclusive region. There is a small offset in the peak positions between the MC and data, a shift of 0.295 GeV^2 is determined by fitting both the data and MC with the Gaussian function. After shifting M_x^2 from MC with 0.295 GeV^2 to the large value both the data and MC fit each other very well, and it is indicated in the bottom right panel of Fig. 6.5. This shift of 0.295 GeV^2 will be applied to missing mass squared distributions appearing later. The MC-data comparisons in all kinematic distributions extracted from the exclusive region can be found in Fig. 6.5, good agreements can be observed between data and MC except that data-MC overshoot. In the MC distributions only the elastic BH process is included. The part between the two vertical lines in the missing mass squared distribution illustrates the exclusive region.

In the current MC production, a new modeling has been implemented in the digitization of the calorimeter. However, the new modeling still needs to be understood for the analysis. In this work we stick to the traditional way to handle the photon energy in MC.

6.4 BH/DVCS with the Recoil Detector

Up to now the physics processes have only been analyzed from the forward spectrometer through the missing mass squared distribution. In this section we will first check the basic performance of the Recoil Detector, then the forward spectrometer and the Recoil Detector will be integrated to investigate both the elastic BH/DVCS and associated BH processes.

6.4.1 The Performance of the Recoil Detector

The recoil protons from the exclusive processes carry a small fraction of momentum of the final states. For the elastic BH/DVCS processes the low t events are of great interest from the theoretical point of view. However, this region can not be studied very well with the forward spectrometer alone due to the detector resolutions [27]. These low t events correspond to very slow recoil protons in the final states. Therefore, the Recoil Detector was designed to cover a wide momentum range as shown in Fig. 4.4. To deal with this wide momentum coverage, several tracking methods have been developed for the recoil particles, especially for the recoil protons [94, 95].

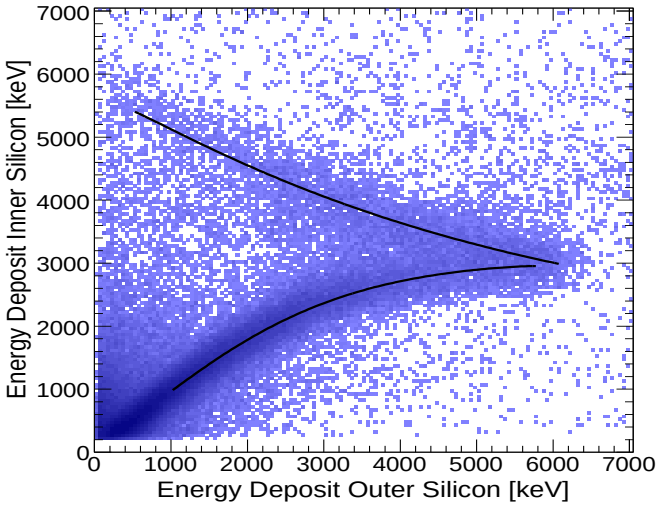

Figure 6.6: Energy deposition in the inner SSD layer vs. energy deposition in the outer SSD layer. The black lines represent the results from a Geant4 simulation.

The Recoil Tracking

Fig. 6.6 shows the energy deposition in the inner SSD layer vs. energy deposition in the outer SSD layer. The black lines represent the results from a Geant4 simulation. The upper branch in the plot indicates the slow protons passing through the inner silicon sensors and getting stopped in the outer silicon sensors. These protons are called the stopped protons and are reconstructed and distinguished by the correlation between the two energy depositions in the inner and outer SSD layers.

Most of the statistics in Fig. 6.6 gather in the lower part of the lower branch. They contain most of the pions and the protons with high momenta, and deposit the similar small energies in the both SSD layers. These particles can reach the SFT barrels and even penetrate the outer SFT barrel, three or four spacepoints can be formed together from the SSD and SFT. Their momenta are reconstructed via the bending inside the magnetic field, the energy depositions from the SSD layers and other passive materials in the scattering chamber are taken into account for the tracking. In the following parts, the 3/4-spacepoint particles refer to these particles. In the reality, all the positive charged 3/4-spacepoint tracks are assumed to be π^+s and reconstructed by the bending, this is so-called the pion-hypothesis tracking. While in the proton-hypothesis tracking all the positive charged tracks from the pion-hypothesis method are assumed to be protons, and their momenta are corrected according to the energy depositions through the passive materials of the protons.

Regarding the events in the higher part of the lower branch, they are very likely the protons which deposit more energy in the outer SSD layer than in the inner layer. They

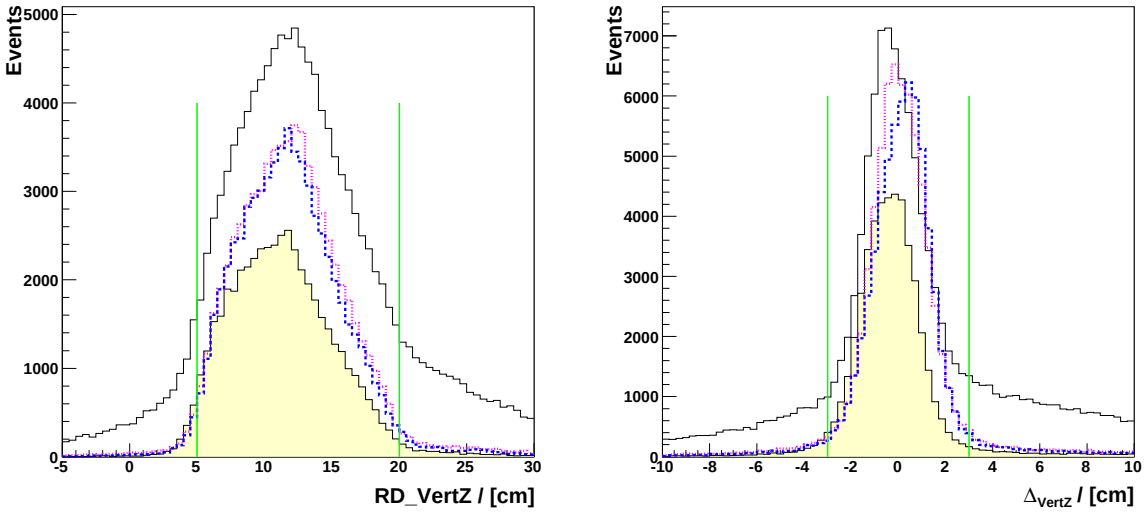

Figure 6.7: The distribution of the reconstructed longitudinal vertex of the recoil tracks z_{vtx} (the left panel), and its difference to the position from the forward spectrometer measurement (the right panel). The solid line and the shaded area represent tracks from the first and second quadrant respectively, while the dotted (dashed) line indicates the third (fourth) quadrant.

have larger momenta than the ones from the upper branch, and they may stop in the outer SSD layer or pass through it and don't have enough energy to reach the SFT barrels. In the recoil tracking, when there are more than one spacepoint in the SSD which are not used in 3/4-spacepoint tracks, the 2-spacepoint tracks will be reconstructed by them according to the energy depositions in the SSD layers and other passive materials. By doing so, the momenta of the protons in the higher part of the lower branch can be reconstructed.

Fig. 6.7 shows the longitudinal vertices of the pion-hypothesis recoil tracks (the left panel) and their deviation to the vertices reconstructed by the forward spectrometer (the right panel). Due to the miscalibration of the silicon detector, less tracks can be reconstructed in the fist quadrant (shaded area). The low efficiency of the outer SFT barrel and the loss of one coordinate in the inner silicon layer cause a larger number of tracks being reconstructed in the second quadrant. The third (dotted line) and the fourth quadrant (dashed line) have the normal performance. The same as for the forward spectrometer, the longitudinal vertices are required to be located between 5 and 20 cm corresponding to the length of the target cell. The difference Δ_{VertZ} is demanded to be between -3 and 3 cm in this work to clean up ghost tracks.

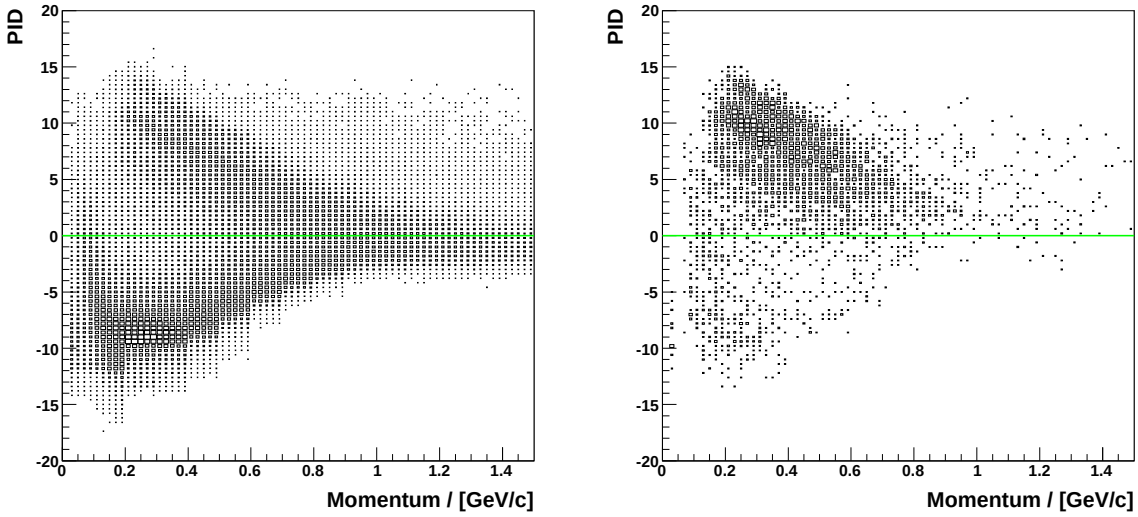

Figure 6.8: The PID distributions from the DIS events (left panel) and from the elastic BH/DVCS process (right panel) are demonstrated for the 3/4-spacepoint pion-hypothesis tracks.

The Recoil PID

As discussed in the previous chapter, the recoil Particle Identification (PID) has been developed based on the pion-hypothesis tracks with 4 spacepoints. Fig. 6.8 shows the recoil PID versus the reconstructed momenta of the DIS events (left panel) and BH/DVCS candidates in the exclusive region (right panel) from data. The systematic quality and the usage of the recoil PID is still being studied. In this work, the positive charged particles with the PID value above 0 are determined as the protons, whereas the π^+s should have the PID value below 0. On the plots the horizontal lines indicate the PID equal to 0. It can be noted from Fig. 6.9 that the number of exclusive events under the missing mass squared distribution drops very little (from dashed line to the solid circles) after requiring this PID cut, meanwhile the events from the non-exclusive region drops much more.

The Recoil Kinematics

Due to the lower number (maximum 4) of the spacepoints available from the Recoil Detector, a relatively high multiplicity of fake tracks can not be completely avoided from the recoil tracking. Fig. 6.10 indicates the positive charged recoil track multiplicities from the DIS events (left panel) and from the exclusive BH/DVCS events (right panel). In the figure the solid line represents the sum of the π^+s (dashed-dotted line) and the protons (points). The proton multiplicity is decomposed into the 3/4-spacepoint tracks (dotted line) and stopped protons (shaded area) and left 2-spacepoint protons (dashed line). The

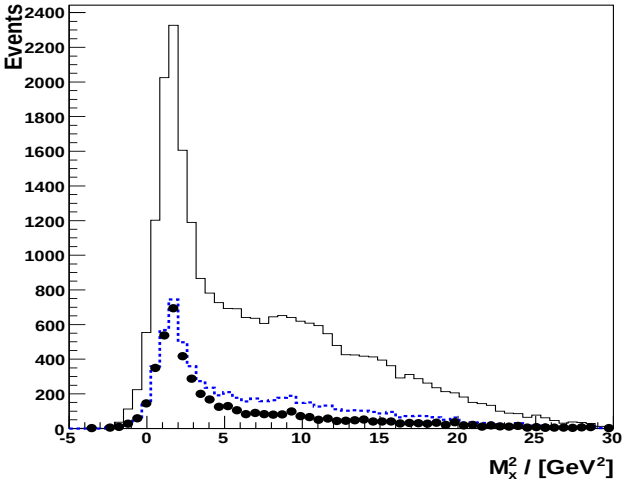

Figure 6.9: The missing mass squared M_x^2 distributions are shown by imposing the standard DVCS cuts for the forward spectrometer (solid line), the additional demanding of the positive charged recoil tracks (dashed line), and the further requirement of the recoil PID > 0 (solid circles).

recoil PID has been used here to distinguish the protons from the pions. The pions have the highest multiplicity in the DIS events. Whereas, in the exclusive events sample, the track multiplicities are dominated by the protons. Around 45% of the exclusive events have the detected recoil protons and among 91% of them the multiplicity of the detected recoil protons is 1. In this work only these events with single detected recoil proton will be used to extract the BSA.

The distributions of the momentum, θ and ϕ of the recoil particles are demonstrated for the DIS events in Fig. 6.11, and for the exclusive BH/DVCS events in Fig.6.12. The layout used in these figures are the same as in Fig. 6.10: the solid line represents the sum of π^+s (dashed-dotted line) and the protons. Meanwhile the proton contribution is also decomposed into the different types of the reconstructed protons.

In the figures, the momentum distribution of the 3/4-spacepoint protons spikes upward at the momentum of 600 MeV/c. This is caused by the tracking method in the 07c1 data production, where the proton-hypothesis tracking method was only applied for the protons with momenta below 600 MeV/c. So the original momentum distribution from the pion-hypothesis tracking was corrected and smeared to the region above 600 MeV/c. The protons with original momenta above 600 MeV/c were not corrected and had the same distribution as the non-corrected momentum distribution. The corrected momentum distribution squeezed the non-corrected distribution in the small region above 600 MeV/c, finally the overall momentum distribution enhanced and produced the spikes in both fig-

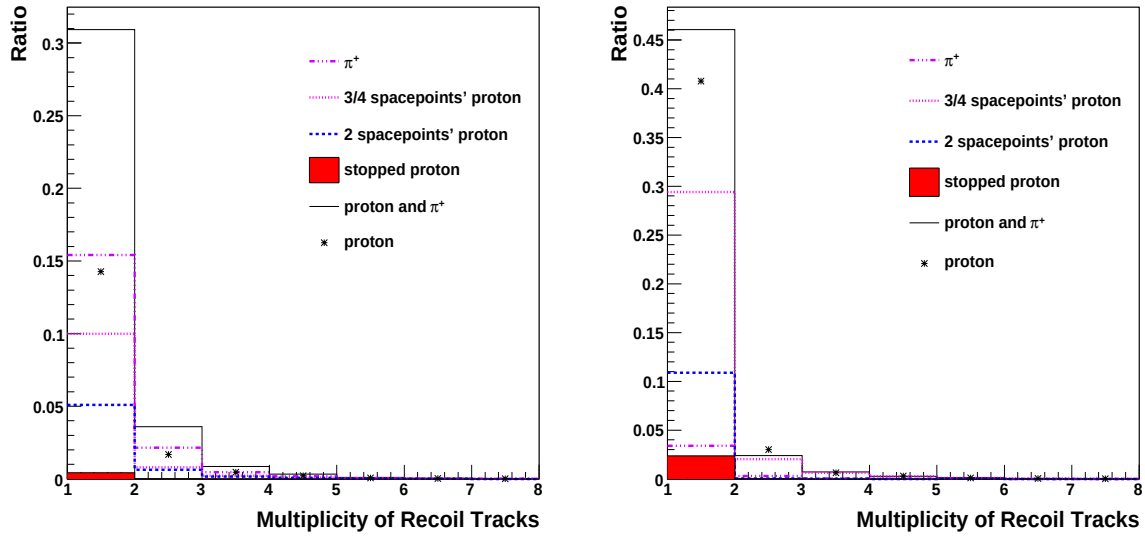

Figure 6.10: The multiplicities of the recoil particles from DIS (left panel) and BH/DVCS (right panel) processes. The solid line represents all the positive charged recoil particles, while the dashed-dotted line indicates the π^+s and the points represent the recoil protons. The contributions from the recoil protons are divided into 3 species: the 3/4-spacepoint protons (dotted line), the stopped protons (shaded area), and the 2-spacepoint protons(dashed line).

ures. In the proton-hypothesis tracking, some ghost tracks can be cleaned using additional information of the energy deposition in the passive materials. This has been proven in Fig. 6.11 by the less number of 2-spacepoint protons reconstructed with the momenta below 600 MeV/c.

In the ϕ angle distributions from Fig. 6.11 clear quadrant features can be observed. These features are related to the performance of the detector. In the first detector quadrant (fourth quadrant in the ϕ angle), due to the miscalibration of the silicon detector less pions were reconstructed. While in the second detector quadrant (first quadrant in ϕ), the low SFT efficiency and the lack of one silicon coordinate make more pions and less 2-spacepoint tracks be reconstructed. The other two healthy quadrants have similar performance. However, the quadrant features in Fig. 6.12 don't behave as notable as the ones in Fig. 6.11.

The recoil data is still under development, some of the kinematic features will be changed from the new data productions in the future. For example, the momentum distributions will be changed due to the extension of the proton-hypothesis tracking to the higher momentum region. The features in the first detector quadrant will probably be gone with the improved silicon calibration. However, the performance of the second detector

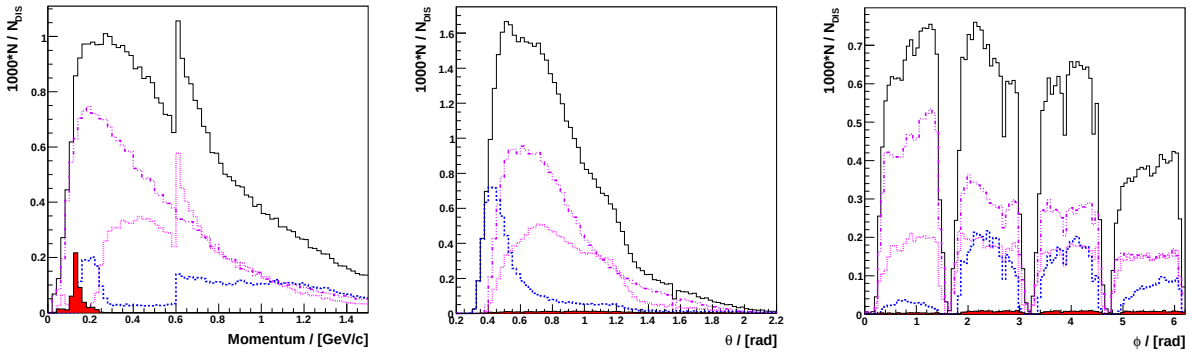

Figure 6.11: The distributions of momenta (left), θ (middle) and ϕ (right) of the recoil particles from the DIS events. The layout of the figure is the same as in Fig. 6.10.

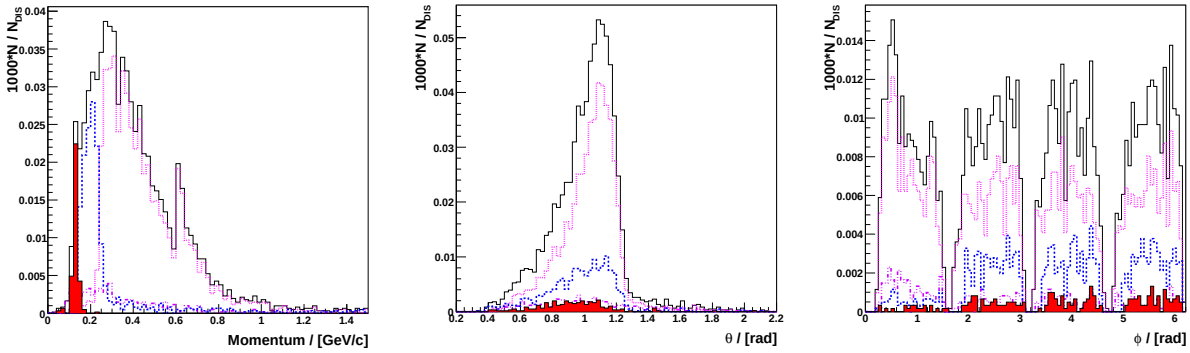

Figure 6.12: The distributions of momenta (left), θ (middle) and ϕ (right) of the recoil particles from the the BH/DVCS processes. The layout of the figure is the same as in Fig. 6.10 and Fig. 6.11.

quadrant will not be improved due to the low detector efficiency and lack of one coordinate information, these features will finally be implemented into the MC simulation and the corresponding systematic uncertainty will be assigned to the final physics results.

6.4.2 The Selection of the Elastic BH/DVCS Process

The final state particles of the elastic BH/DVCS process include two parts: the real photon and the scattering positron detected by the forward spectrometer, and the directly detected recoil proton by the Recoil Detector. The missing mass technology for the forward part can still be used in this analysis. The exclusive missing mass squared distribution can be tagged by the detected recoil protons, the kinematic relations between the forward part and the recoil part can be further required to select the exclusive events.

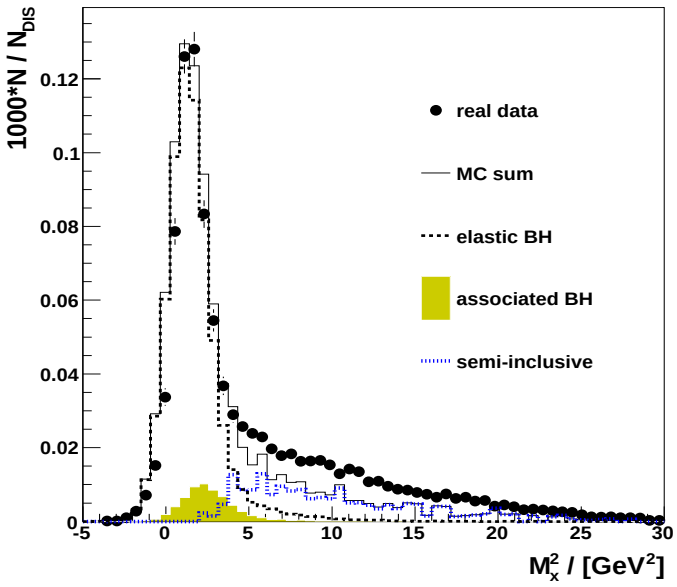

Figure 6.13: Comparison between the absolutely normalized Mx^2 distributions from the MC simulation (solid line) and from the experimental data (solid circles). At least one recoil proton was required in the Recoil Detector. The BH/DVCS processes are simulated from the dominating BH process. The MC contributions are decomposed to the elastic BH process (dashed line), the associated BH process (shaded area), and the semi-inclusive processes (dotted line).

Fig. 6.13 indicates the missing mass squared distribution of the events by requiring all the standard DVCS cuts for the forward spectrometer, and at least one recoil proton from the Recoil Detector. The layout of the figure is the same as in Fig. 6.5. In the non-exclusive region, a higher yield is obtained from the data than from the MC simulation, which is due to the incompletely simulated performance of the detector in the MC. Unlike what is seen in Fig. 6.5, in the exclusive region the MC overshoots the data, which mainly comes from the fact that the efficiency of the detector has not been included in the MC production. With additional information from the Recoil Detector, the background contributions from the associated and semi-inclusive DIS processes to the exclusive region drop from 15% to around 6%.

To further clean up the background both from the physics processes and the possible ghost particles reconstructed from the detector, useful cuts have to be found. Due to the fact that the reconstructed azimuthal angle has a very good resolution (see Fig. 4.10), two related cuts were proposed by the TDR as in Fig. 6.14 and defined as follows [27, 61]:

- the angle ω between the missing transverse momentum and the detected transverse momentum of the recoil proton and the ratio R of their absolute values should be in the

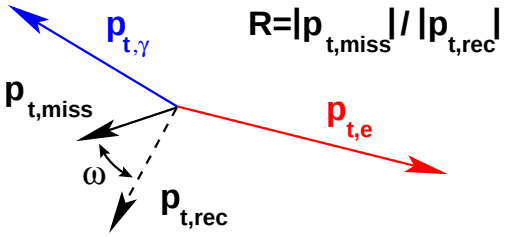

Figure 6.14: Definition of ω and R: The missing transverse momentum vector $\vec{p}_{t,miss}$ is reconstructed from the observed transverse momentum vectors of the photon $\vec{p}_{t,\gamma}$ and the lepton $\vec{p}_{t,e}$. $\vec{p}_{t,rec}$ is the transverse momentum vector of a proton that is detected in the recoil detector. The angle ω and the ratio R are defined in the drawing. (courtesy from [61])

regions [27]: $\omega < 0.3$ rad and $0.5 < R < 1.5$.

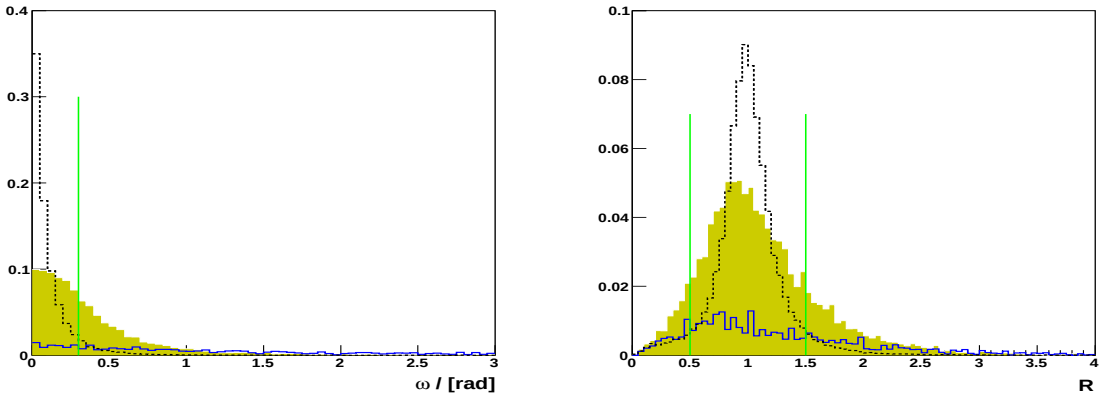

Figure 6.15: The distributions of the ω (left panel) and R (right panel) from the elastic BH (dotted line), associated BH (shaded area), and the semi-inclusive DIS (solid line) processes in the MC simulation. The distributions are normalized to unity.

These two cuts are called coplanarity cuts. The effect of them are shown in Fig. 6.15 and Fig. 6.16. In Fig. 6.15 only the effects from the MC simulation are examined, the dotted line represents the elastic BH process, the shaded area and the solid line are from the associated BH and semi-inclusive processes respectively, all the three processes are normalized to unity separately. The vertical lines in the figures indicate the range of the cuts. These two cuts can not completely clean up the backgrounds, but, they can remove relatively more background than the signal and hence bring down the overall background ratio. Fig. 6.16 indicates the effects both from the MC (the layout same as the previous figure) and the data (solid circles), all the processes normalized to the number of DIS events. Good agreement can be achieved between the data and MC simulation, except that there is a small shift of the data points towards small values in the R distribution.

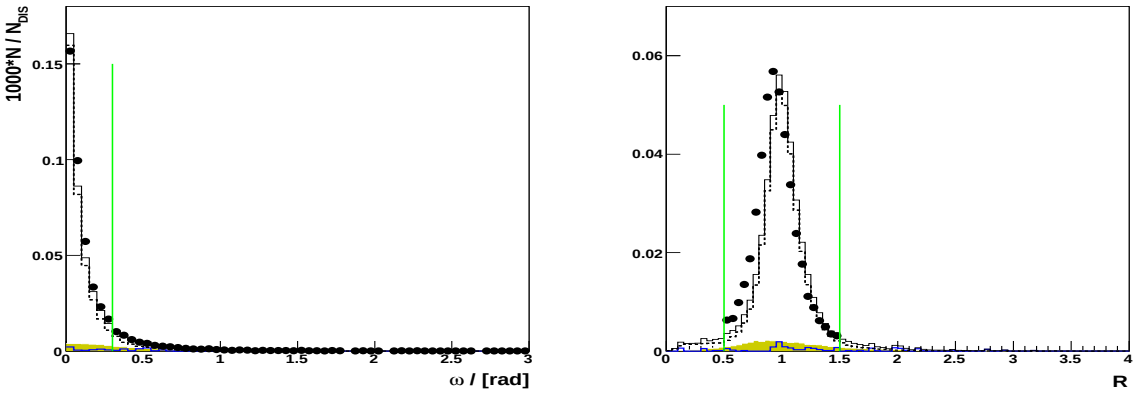

Figure 6.16: The comparisons of the distributions ω (left panel) and R (right panel) between data (solid circles) and MC. The layout of the MC contributions are the same as in Fig. 6.15. All the distributions are normalized to the number of DIS events.

It is noted that the coplanarity cuts can reduce the backgrounds both from the exclusive and non-exclusive regions from the bottom right panel of Fig. 6.19. In the exclusive region the contribution from the associated process decreases to the level of around 3%, while the semi-inclusive contribution is so small that it can be neglected. These two cuts can not only get rid of the physics backgrounds but also eliminate ghost tracks in the Recoil Detector. This is proven by the fact that the discrepancy between the MC and data is gone after imposing the coplanarity cuts in the non-exclusive region.

However, the new coplanarity cuts may be changed and even abandoned in a future analysis in case that the photon detector gives sufficient additional information to clean up the backgrounds. The study of the data from the photon detector is still under way.

The basic recoil kinematics have been examined for the exclusive events. The comparisons of these events between the MC and data are shown in Fig. 6.17. Overall there are some discrepancies between data and MC in all distributions of the momentum, θ, and ϕ. These discrepancies mainly come from incompletely simulated detector performance in the MC production, in which the efficiencies of the detector may play a very important role.

In principle the effect of the quadrant features can be counteracted in the calculation of the asymmetries. Nevertheless, this has to be carefully studied when the MC can fully describe the detector performance. Fig. 6.18 shows the correlation between the ϕ angle of the recoil proton (horizontal axis) and the azimuthal ϕ angle between the lepton scattering plane and the photon production plane (vertical axis). There is a large empty area along the middle of the figure which is related to an acceptance gap in the forward spectrometer. Due to this empty area the quadrant dependent efficiency of the recoil detector can influence the distribution of azimuthal ϕ angle. The effect of this influence to the asymmetries has

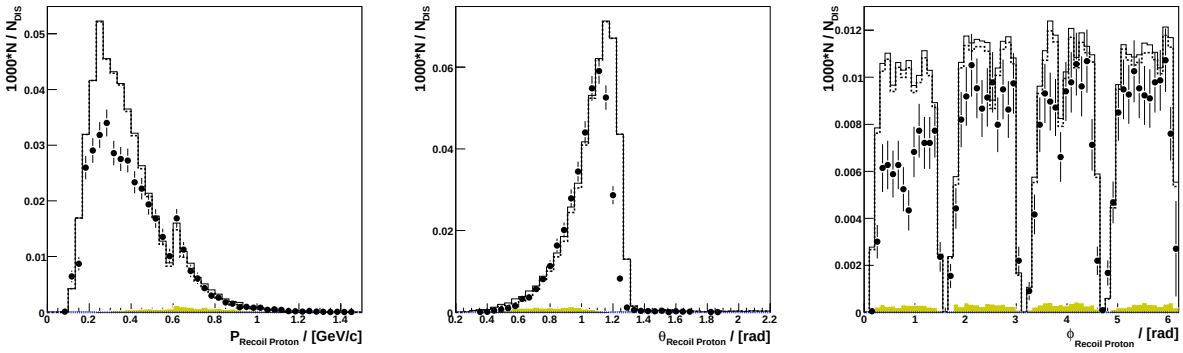

Figure 6.17: The distributions of momenta (left), θ (middle) and ϕ (right) of the recoil particles from the exclusive region of the BH/DVCS processes in the right figure of Figure 6.12. The solid line represents distributions from MC, the solid circles represent for the data, and the other two represent semi-inclusive processes (dashed-dotted line) and BH resonant process (shaded area).

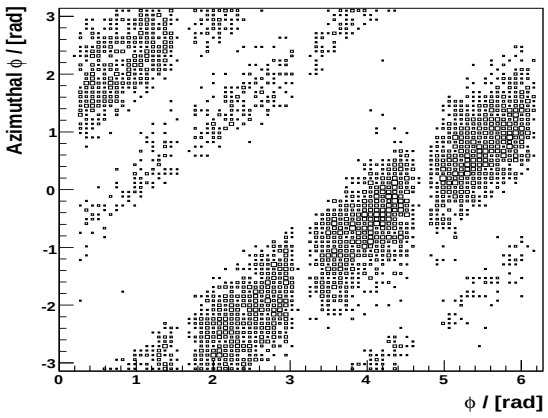

Figure 6.18: Correlation between the ϕ angle of the recoil proton (horizontal axis) and the azimuthal ϕ between the lepton scattering plane and the photon production plane (vertical axis).

to be studied with MC simulation when the detector performance is fully described in MC.

Similar as in Fig. 6.5 the basic kinematic variables of the BH/DVCS exclusive events have been examined between the MC and data, the comparisons are shown in Figure 6.19. Regarding the distribution of the azimuthal ϕ angle, there is a discrepancy between the data and MC. The two shapes look similar overall with different yields, except in the region of large ϕ angle which locate exactly in the second detector quadrant as in Fig. 6.18.

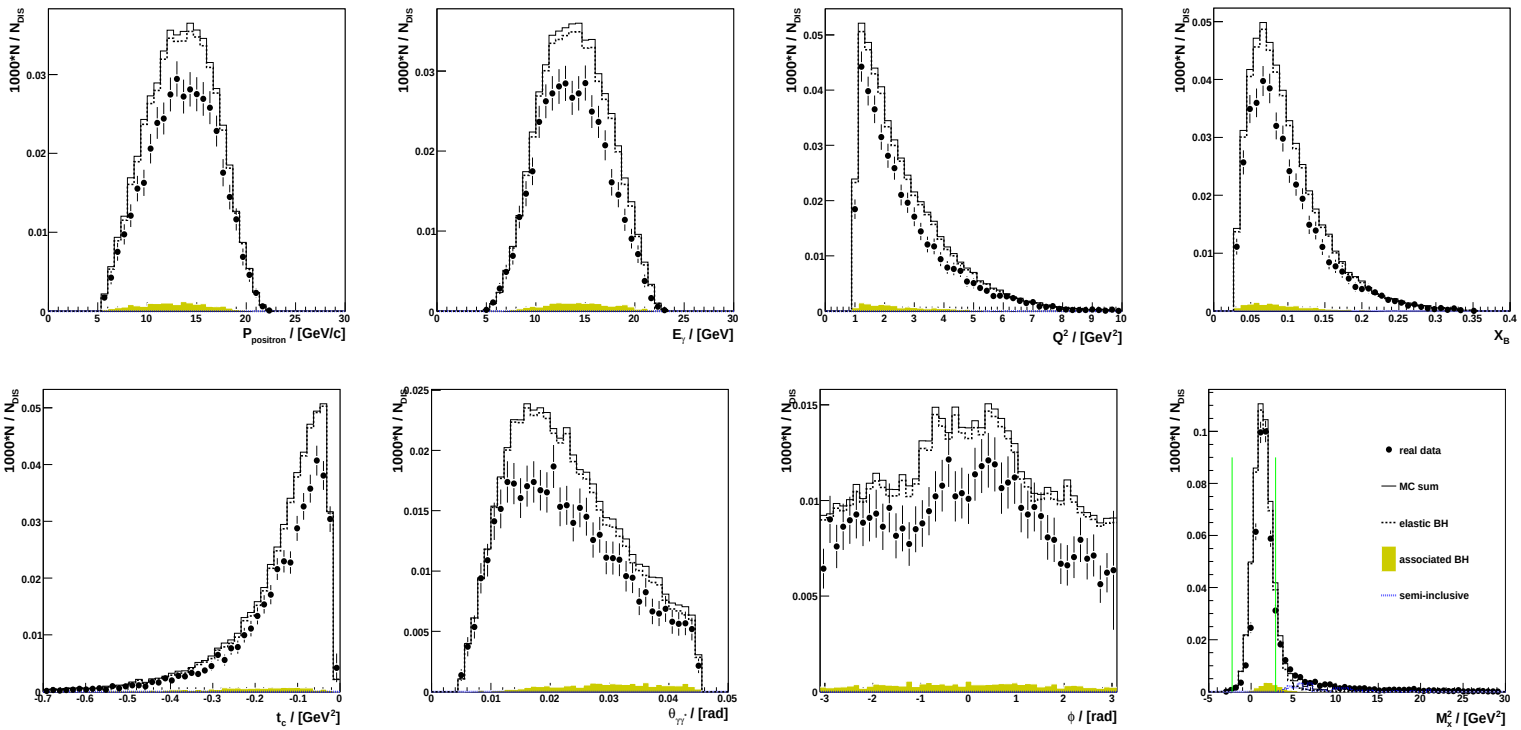

Figure 6.19: Comparison between the MC simulation (solid lines) and the experimental data (solid circles) in the exclusive region -2.25 $<$ Mx^2 $<$ 2.89 GeV^2. The MC simulation is performed without including the DVCS process. Exactly 1 recoil proton passing the coplanarity cuts was detected by the Recoil Detector. Also shown are individual contributions from elastic BH process (dashed line), associated BH process (shaded area). The contribution from the semi-inclusive DIS processes is very little and difficult to be visible.

6.4.3 The Selection of the Associated BH Process

The final state particles of the associated BH process from the decay channel $\Delta^+ \rightarrow n\pi^+$ include a scattered positron, a real photon, a recoil neutron and a π^+. As the Recoil Detector was not designed to detect the neutron, only the π^+ can be detected for the resonance. Due to this fact, the missing mass method has to be used to achieve the exclusivity. There are two ways to calculate the missing mass for the resonance. One is to calculate the missing mass of the Δ^+ by only using the kinematics from the forward spectrometer while a detected recoil π^+ is treated as a tag of the exclusive events. The calculation of the Δ^+ missing mass is the same as the proton missing mass for the elastic processes. The other way is to calculate the missing mass of the neutron by using the π^+ kinematics, in this method the measured π^+ is taken into the calculation which may deteriorate the resolution. We define this missing neutron mass M_N as

$$M_N^2 \equiv (k + P - k' - q' - P_{\pi^+})^2, \tag{6.6}$$

where the P_{π^+} represents the four-momentum of the detected π^+. The M_N can be expanded as

$$M_N^2 = M_x^2 + m_{\pi^+}^2 - 2E_{\pi^+}(\nu + m_P - E_{\pi^+}). \tag{6.7}$$

The two methods will be examined and one of them will be chosen to extract the asymmetries later in this section.

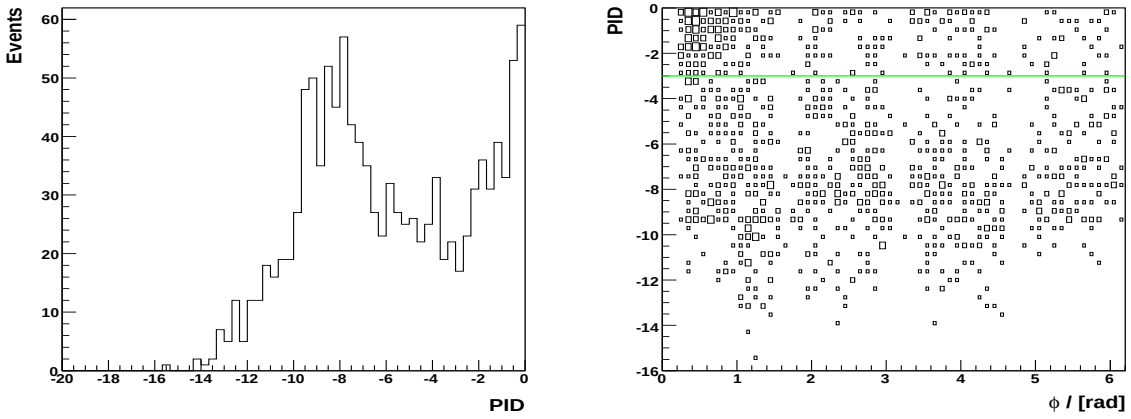

Figure 6.20: The PID distributions of the π^+s from the exclusive region of the BH/DVCS processes. A one dimensional distribution of PID (left panel) and two dimensional plot of PID v.s. ϕ of the recoil π^+s (right panel) are shown here.

From Fig. 6.10 it is known that the yields of the recoil π^+ vary much from quadrant to quadrant due to the performance of the Recoil Detector. Especially, much more π^+s are reconstructed in the second quadrant than the other parts. While in the first quadrant the

number is much less due to the miscalibration of the silicon detector. The low productivity can not be corrected in this work. Most of the π^+s in the second quadrant are the ghost tracks and can be corrected by imposing certain constraints on the data. Fig. 6.20 shows the PID distributions of the recoil π^+s from the exclusive region of the associated BH processes. The left panel represents the one dimensional PID distribution while the right panel indicates the two dimensional plot of PID versus the ϕ angle of the recoil π^+. A main peak can be noted in the left figure around the value of -8, while there are a lot of events gathering around the region very close to zero. In the right panel it can be seen that most of the particles with small PID value come from the second quadrant. This is a strong indication that the low efficiency of the detector causes the high level of ghost tracks. In this analysis a simple cut of PID $<$ -3 will be used to select the real π^+ to avoid including many ghost tracks. This is only a temporary cut used for the current data production. After the ghost track level can be fully understood a more sophisticated cut should be implemented according to the ratio of signal-to-ghost tracks with the help of the MC simulation.

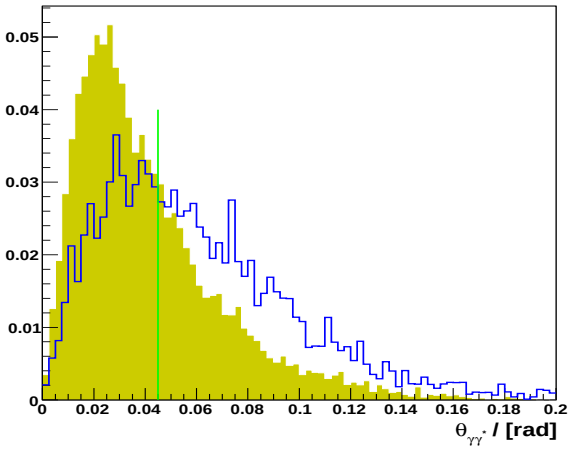

Figure 6.21: The distribution of $\theta_{\gamma\gamma^*}$ of the resonant process from MC. Also shown are individual contributions from associated BH process (shaded area), and semi-inclusive processes (line).

Regarding the cuts to select the associated BH process via the detection of the π^+, the basic kinematic requirements and the fiducial volume cuts used for the elastic BH/DVCS should not be changed. The photon geometry cut, the requirement of the energy loss in the pre-shower detector from the photon and the cuts related to the angle $\theta_{\gamma\gamma^*}$ still have the space to be released to accumulate more statistics. However, releasing the first two cuts can result in a deterioration of the missing mass distribution. This will in our case bring in the difficulty to distinguish the resonance from the elastic processes. About the

effect of releasing the third cut, Fig. 6.21 shows the distribution of $\theta_{\gamma\gamma^*}$ from associated BH process (shaded area) and the semi-inclusive process (solid line) in MC. The vertical line indicates the upper limit of the standard cuts for the $\theta_{\gamma\gamma^*}$. It can be seen from the figure that the contributions of the both processes equal each other at the point where the upper limit of the cut stays. In the region below that line the associated process dominated the semi-inclusive while it is vice-versa in the upper region. Based on these facts, all the standard cuts from the forward spectrometer for the elastic BH/DVCS will be used for the associated BH process .

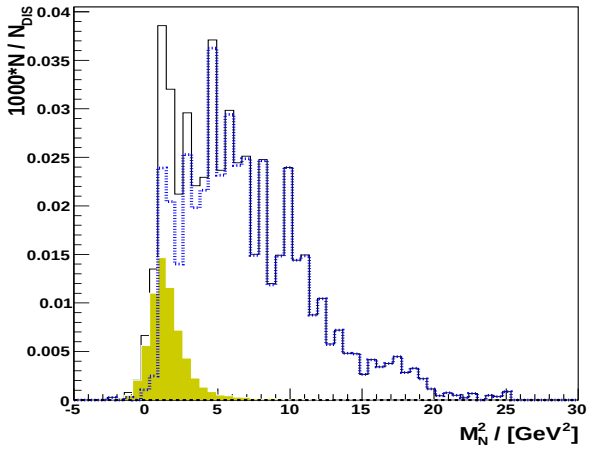

Figure 6.22: Normalized missing mass distributions of the recoil neutrons of the Δ^+ resonant process from the MC simulation. Also shown are individual contributions from associated BH process (shaded area), and semi-inclusive DIS processes (dotted line).

Fig. 6.22 shows the missing neutron mass squared from the MC simulation after implementing all the standard cuts and requiring the π^+ with PID < -3 being detected by the Recoil Detector. In the figure the associated BH process is indicated by the shaded area, the semi-inclusive process is illustrated by the dotted line and the solid line represents the sum of both. In the exclusive region the ratio of the associated and semi-inclusive processes is close to 1 or even more, which can make the extraction of the asymmetry very unreliable.

Fig. 6.23 illustrates the missing mass squared distributions of the Δ^+ both from the MC simulation (solid line) and the data (solid circles). The comparison indicates a large discrepancy of the yields between the MC and data. However the peak positions from data and MC overlap each other, as this position somehow only relates to the detector resolution which has already been modeled well in the current MC programme. The large discrepancy is questionable and needs to be carefully studied at a later stage.

Due to the incapability of the MC simulation to describe the experimental data points. Studies need to be carried out on the experimental data to understand the current situation.

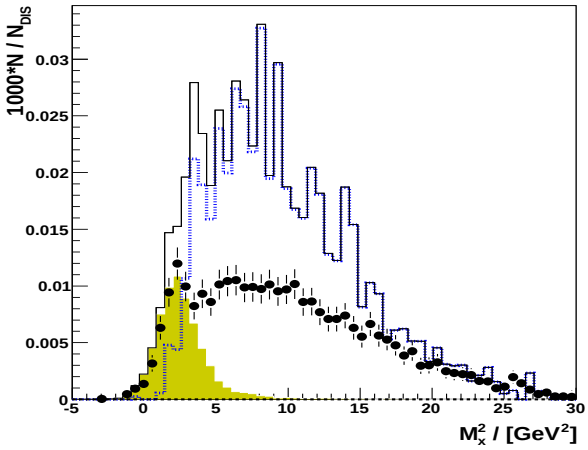

Figure 6.23: Normalized missing mass distributions of the Δ^+ from the MC simulation (solid line) and from the data (solid circles). The MC is decomposed into the contributions from associated BH process (shaded area), and semi-inclusive DIS processes (dotted line).

There are two fundamental points that we have to clarify in order to understand the associated BH process: how real is the peak of Δ^+ and how much semi-inclusive background is contained in the exclusive region.

To elaborate the potential problem, the first point relates to the quality of the particle identification for the π^+ and the level of the ghost tracks from the Recoil Detector. As there is no decay channel of the Δ^+ to the final particles with π^-, the events containing the recoil π^- may give a reasonable estimation of the background for the associated process. These events include both the semi-inclusive process and the ghost events reconstructed by the Recoil Detector.

Fig. 6.24 shows the distributions of the missing mass squared distributions both from the elastic (solid line) and associated processes (solid circles). In the right panel additional distributions from the events when the π^- was detected (shaded area) or the detected π^+s with the PID larger than -3 (dotted line). Compared to the elastic peak, the associated peak locates clearly in the region with higher value and has a broader width. The events under the associated peak can not be mistaken from the elastic events. In the right panel the events with the recoil π^- describe well the background distribution of the associated process, the misidentification of the π^+ and the ghost tracking events can not explain the large extra yields in the exclusive region of the π^+ events. Furthermore, from the events containing the π^+ with PID > -3 no peak or bump can be found in the exclusive region. The σ from the fitting results in the left panel was used to form the exclusive region (between -3 and 1 σ), it is indicated by the two vertical lines from the figure. The events from this exclusive region will be used to extract the asymmetry. Fig. 6.25 shows the basic

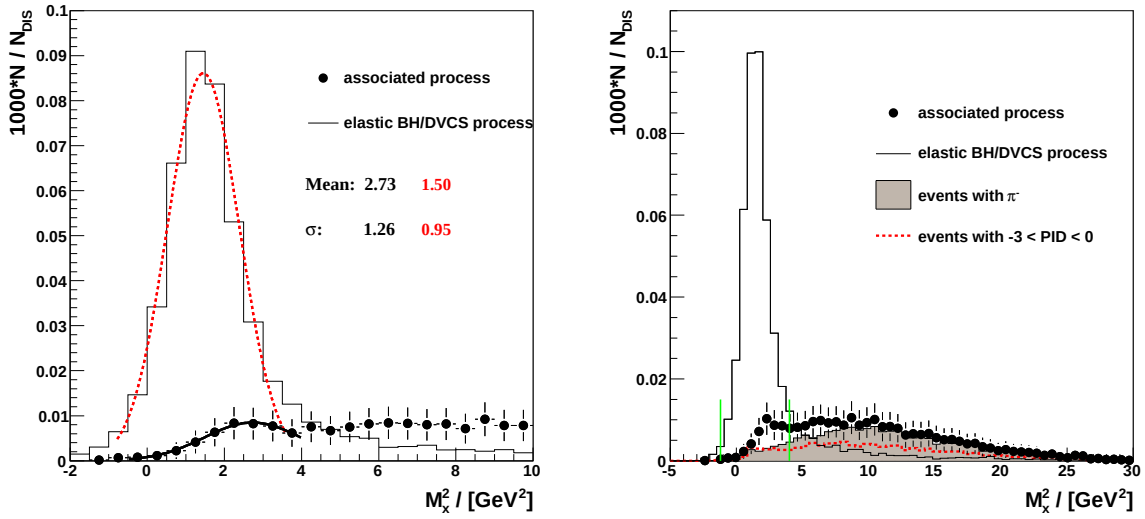

Figure 6.24: The distributions of the missing mass squared both from the elastic (solid line) and associated processes (solid circles). The two distributions are fitted by the Gaussian functions in the left panel. While in the right panel additional distributions from the events when the π^- was detected (shaded area) or the detected π^+s from Fig. 6.8 with the PID larger than -3 (dotted line). The two vertical lines indicate the exclusive region.

kinematics of the π^+ from this exclusive region.

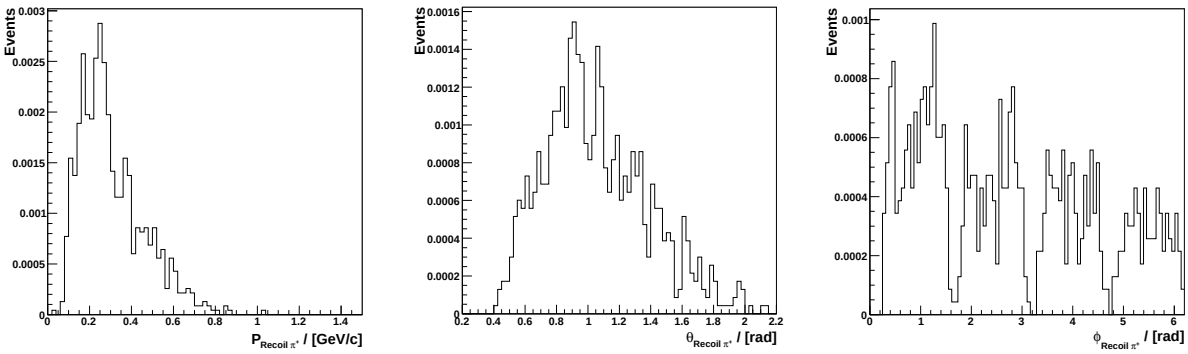

Figure 6.25: The distributions of momenta (left), θ (middle) and ϕ (right) of the π^+ from the exclusive region of the Δ^+.

6.5 The Beam-Helicity Asymmetries

6.5.1 The Fitting Methods

The cross section of the elastic BH/DVCS process can be factorized as [32]

$$\frac{d\sigma_{LU}}{dx_B dy d|t| d\phi} = \sigma^0_{UU}(\phi)[1 + P_b A^{DVCS}_{LU}(\phi) + e_l A_C(\phi) + e_l P_b A^I_{LU}(\phi)], \tag{6.8}$$

where L (U) stands for the longitudinal polarized beam (unpolarized target), e_l and P_b represent the beam charge and beam helicity respectively.

In this work only the positron beam data will be discussed, this equation can be simplified to:

$$\frac{d\sigma_{LU}}{dx_B dy d|t| d\phi} = \sigma^0_{UU}(\phi)[1 + P_b A_{LU}(\phi)], \tag{6.9}$$

where $A_{LU}(\phi) = A^{DVCS}_{LU}(\phi) + A^I_{LU}(\phi)$ and it can be expressed by the following simple formula:

$$A_{LU}(\phi) = A^{\sin(0\phi)}_{LU} + A^{\sin(\phi)}_{LU} \sin\phi + A^{\sin(2\phi)}_{LU} \sin(2\phi). \tag{6.10}$$

Both the least squares and the maximum likelihood fitting can be performed with this formula.

The method of least squares fitting is also called χ^2 fitting which relies on the fact that if x_1,..., x_n are n independent Gaussian random variables, the sum $\Sigma_i (x_i - \mu_i)^2/\sigma_i^2$ follows the χ^2 probability density function with n degrees of freedom. Consider a set of N independent measurements y_i, which are Gaussian distributed with mean $F(x;\theta)$ and known variance σ_i^2, at known points x_i. The estimator for the mean of the parameters θ is given by the minimum location of [80]

$$\chi^2 = \Sigma_i \frac{[y_i - F(x_i;\theta)]^2}{\sigma_i^2}. \tag{6.11}$$

The estimator for the variance of the parameters θ is given by the tangent planes of the contour in the parameter space defined by

$$\chi^2(\theta) = \chi^2_{min} + 1. \tag{6.12}$$

We assume that a set of N independently measured quantities x_i came from a p.d.f. $f(x;\theta)$, where $\theta = (\theta_1, ..., \theta_n)$ is set of n parameters whose values are unknown. In the method of maximum likelihood the estimator θ is taken from the values of θ that can maximize the likelihood function [80]

$$\mathcal{L}(\theta) = \prod_{i=1}^{N} f(x_i;\theta). \tag{6.13}$$

It is usually easier to work with the logarithm of the likelihood function ln$\mathcal{L}$, the maximum likelihood estimator can be found by solving ln$\mathcal{L}$,

$$\frac{\partial ln\mathcal{L}}{\partial\theta_i} = 0, \qquad i = 1, ..., n. \tag{6.14}$$

The estimator for the inverse covariance matrix is given by

$$(\hat{V}^{-1})_{ij} = \frac{\partial^2 ln\mathcal{L}}{\partial\theta_i\partial\theta_j}|_{\hat{\theta}}. \tag{6.15}$$

The p.d.f. $f(x;\theta)$ is usually normalized to unit area, i.e. $\int dx f(x;\theta) = 1$. However, in applying the ML method, the normalization of the p.d.f. is not necessary unity, but has to be fixed - independently of the fitted parameters. As one is only interested in the maximum of $\mathcal{L}$ and in ratios of $\mathcal{L}$ at different values of the parameters, any multiplicative factors in f that do not involve θ may be dropped.

In the experiments of nuclear and particle physics, the observed number of events often has a Poisson distribution around its expected value $\mathbb{N}$, which may also depend on the parameters. Taking this into account, the likelihood function can be modified to

$$\mathcal{L}(\theta) = \frac{[\mathbb{N}(\theta)]^{N_e - \mathbb{N}(\theta)}}{N!} \prod_{i=1}^{N} f(x_i;\theta). \tag{6.16}$$

In both of the likelihood functions, $\mathbb{N}$ can be interpreted as the normalization of the extended p.d.f. .

According to the cross section, the total number of events in a small time interval (τ, $\tau + d\tau$) and small phase space (x, x + dx) is

$$d\mathcal{N}(x,\tau) = L(\tau)d\tau dx\sigma^0_{UU}[1 + P_b(\tau)(\tau)A_{LU}(x)], \tag{6.17}$$

where $L(\tau)$ is the luminosity. By integrating over P_b one can get the number of events for different effective helicity state via

$$\overrightarrow{\mathbb{L}}\sigma^0_{UU}(x)[1 + \langle\overrightarrow{P_b}\rangle A_{LU}(x)] = \overrightarrow{\mathcal{N}}(x), \tag{6.18}$$

$$\overleftarrow{\mathbb{L}}\sigma^0_{UU}(x)[1 + \langle\overleftarrow{P_b}\rangle A_{LU}(x)] = \overleftarrow{\mathcal{N}}(x), \tag{6.19}$$

where $\rightarrow$ / $\leftarrow$ denotes the positive/negative effective helicity state [96], $\overrightarrow{\mathbb{L}}$ ($\overleftarrow{\mathbb{L}}$) represent the corresponding integrated luminosity and $\langle\overrightarrow{P_b}\rangle$ ($\langle\overleftarrow{P_b}\rangle$) indicate the mean effective beam polarization. Taking the corresponding luminosities into account, the BSA from Eq. (2.37) can be calculated as

$$A_{LU}(x) = \frac{\frac{\overrightarrow{\mathcal{N}}(x)}{\overrightarrow{\mathbb{L}}} - \frac{\overleftarrow{\mathcal{N}}(x)}{\overleftarrow{\mathbb{L}}}}{\frac{\overrightarrow{\mathcal{N}}(x)}{\overrightarrow{\mathbb{L}}}\langle\overrightarrow{P_b}\rangle - \frac{\overleftarrow{\mathcal{N}}(x)}{\overleftarrow{\mathbb{L}}}\langle\overleftarrow{P_b}\rangle}, \tag{6.20}$$

the χ^2 fitting can be performed according to this output.

Based on the above deduction, when the detection efficiency is set to unity the $\mathbb{N}(\theta)$ can be obtained as the following:

$$\mathbb{N}(\theta) = \frac{\mathbb{L}}{\overrightarrow{\mathbb{L}}} \frac{\Sigma_i^{\overrightarrow{N}}[1 + \langle P\rangle A_{LU}(x_i;\theta)]}{[1 - \frac{\langle \overrightarrow{P}\rangle}{\langle \overleftarrow{P}\rangle}]} + \frac{\mathbb{L}}{\overleftarrow{\mathbb{L}}} \frac{\Sigma_i^{\overleftarrow{N}}[1 + \langle P\rangle A_{LU}(x_i;\theta)]}{[1 - \frac{\langle \overleftarrow{P}\rangle}{\langle \overrightarrow{P}\rangle}]}. \tag{6.21}$$

Hence the logarithmic likelihood function is given as

$$-\ln \mathcal{L}(\theta) = -\Sigma_i^N \ln[1 + P_i A_{LU}(x_i;\theta)] + \mathbb{N}(\theta). \tag{6.22}$$

6.5.2 The BSA Asymmetries

The Asymmetries From Elastic BH/DVCS Process

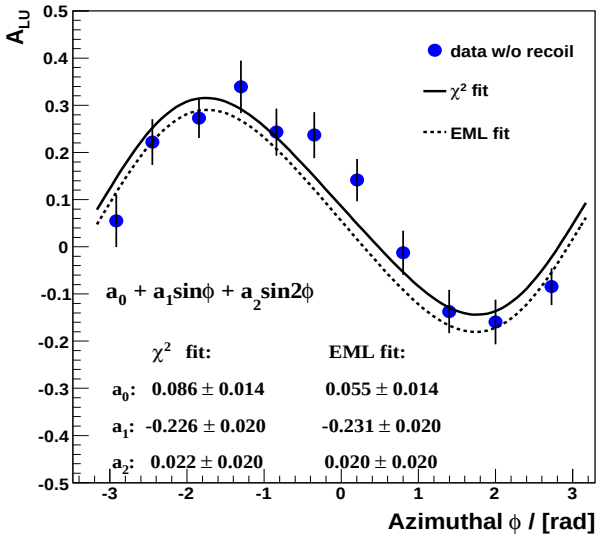

Figure 6.26: The BSA (circle points) from the 2007 positron beam data without using the information provided by the Recoil Detector, only the statistical uncertainties are shown and indicated by the length of the error bars. The data points were fitted to the function $a_0 + a_1 \sin(\phi) + a_2 \sin(2\phi)$ both by the ML (dashed line) and χ^2 fitting (solid line) methods.

In Fig. 6.26 the BSA are extracted from the elastic BH/DVCS process (circle points) based on the proton target data of 2007 via both the least squares Eq. (6.20) or the maximum likelihood fitting Eq. (6.22). No information provided by the Recoil Detector was used here, only the statistical uncertainties were shown. The data points were fitted

Table 6.1: The amplitudes of the BSA from 2007 data without using the Recoil Detector.

	a0	a1	a2
$\chi^2 fitting$	0.086± 0.014	-0.226 ± 0.020	0.022 ± 0.020
ML fitting	0.055± 0.014	-0.231 ± 0.020	0.020 ± 0.020

to the function $a_0 + a_1 \sin(\phi) + a_2 \sin(2\phi)$, the solid line indicates the result from the χ^2 fitting and the dashed line represents the results from the ML fitting. The asymmetry amplitudes from both methods can be found in Table 6.1. Within the uncertainties the results from the both methods agree to each other very well except for a small deviation in the constant term.

The leading term (the $\sin\phi$ term) of the asymmetry amplitudes extracted here is very close to the HERMES published one [24] even though the correction [26] of the background processes hasn't been performed on this analysis.

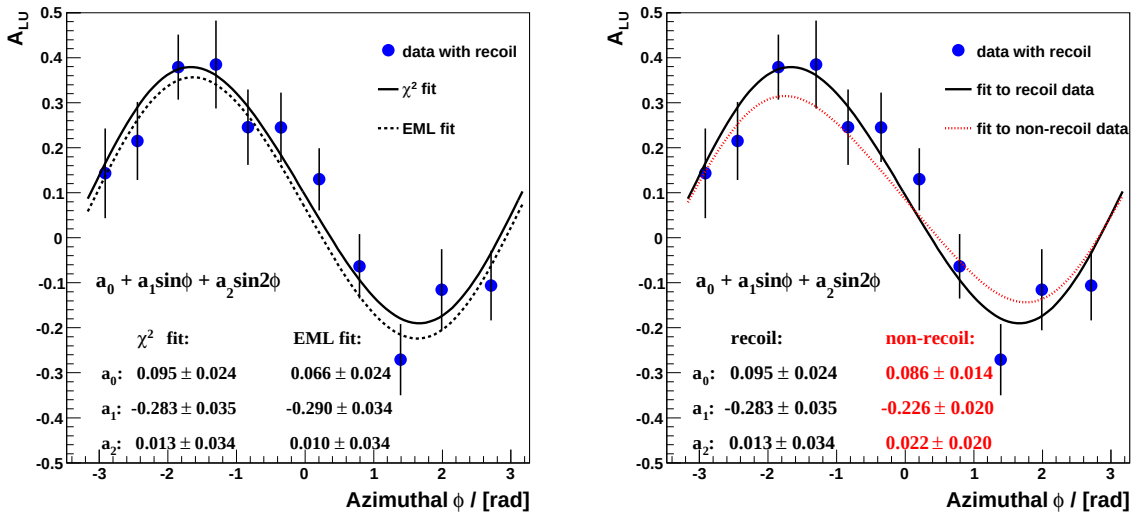

Figure 6.27: The BSA (circled points) from the exclusive events with only one recoil proton passing the coplanarity cuts from the Recoil Detector. The data points were fitted to the function $a_0 + a_1 \sin(\phi) + a_2 \sin(2\phi)$ both by the ML and χ^2 fitting methods. The solid lines in the both panels indicate the χ^2 fitting, and the dashed line in the left panel represents the ML fitting while in the right panel the dotted line denotes the χ^2 fitting from Fig. 6.26.

Fig. 6.27 shows the BSA (circle points) from the exclusive events by requiring only one recoiling proton detected by the Recoil Detector. The recoil proton here must pass the coplanarity cuts. Again only the statistical uncertainties are shown and indicated by the length of the error bars. The data points were fitted to the function $a_0 + a_1 \sin(\phi) + a_2 \sin(2\phi)$

both by the ML and χ^2 fitting methods, the solid lines in the both panels indicate the result from the χ^2 fitting and the dashed line in the left panel represents the one from the ML fitting while in the right panel the dotted line shows the result of the χ^2 fitting from Fig. 6.26. The amplitudes of the asymmetries are given in the Table 6.2.

Table 6.2: The amplitudes of the BSA from 2007 data extracted using the Recoil Detector.

	a0	a1	a2
$\chi^2 fitting$	0.095± 0.024	-0.283 ± 0.035	0.013 ± 0.034
ML fitting	0.066± 0.024	-0.290 ± 0.034	0.010 ± 0.034

The asymmetry amplitudes from Table 6.1 and Table 6.2 are close to each other within the uncertainties. However, the leading amplitude from the recoil data is approximately 25% larger than that only extracted from the forward spectrometer. A relatively small or zero asymmetry from the associated BH process may cause this according to

$$A_{ela.} = \frac{1}{f_{ela.}}(A_{meas.} - f_{ass.}A_{ass.} - f_{SIDIS}A_{SIDIS} - f^{\pi^0}_{excl.}A^{\pi^0}_{excl.}), \tag{6.23}$$

where f (A) denotes the relative contribution (asymmetry) of the individual processes.

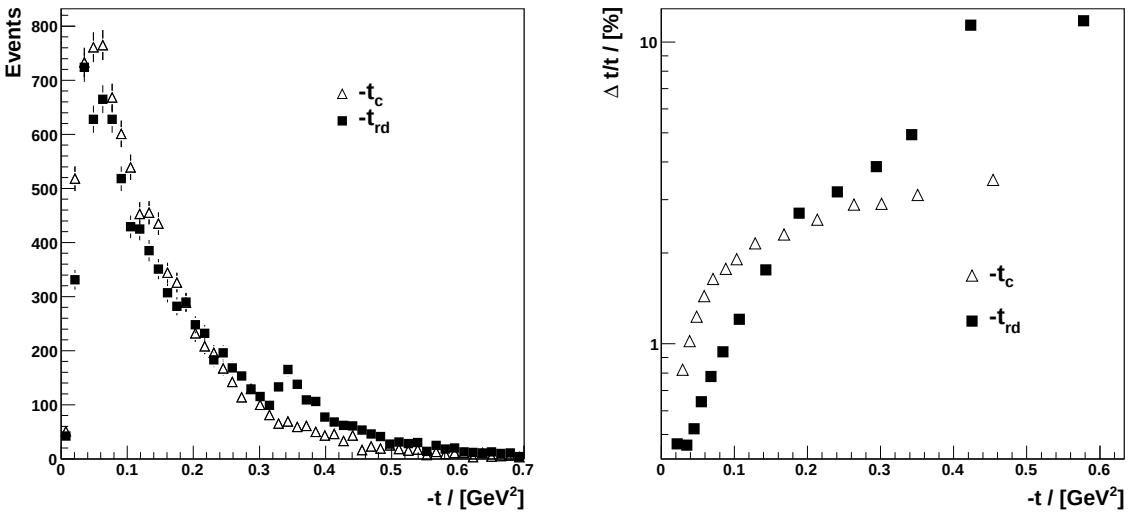

Figure 6.28: The left panel indicates the distributions of the t measured by the forward spectrometer (triangles) and the Recoil Detector (boxes) from the experimental data. Their resolutions are plotted in the right panel.

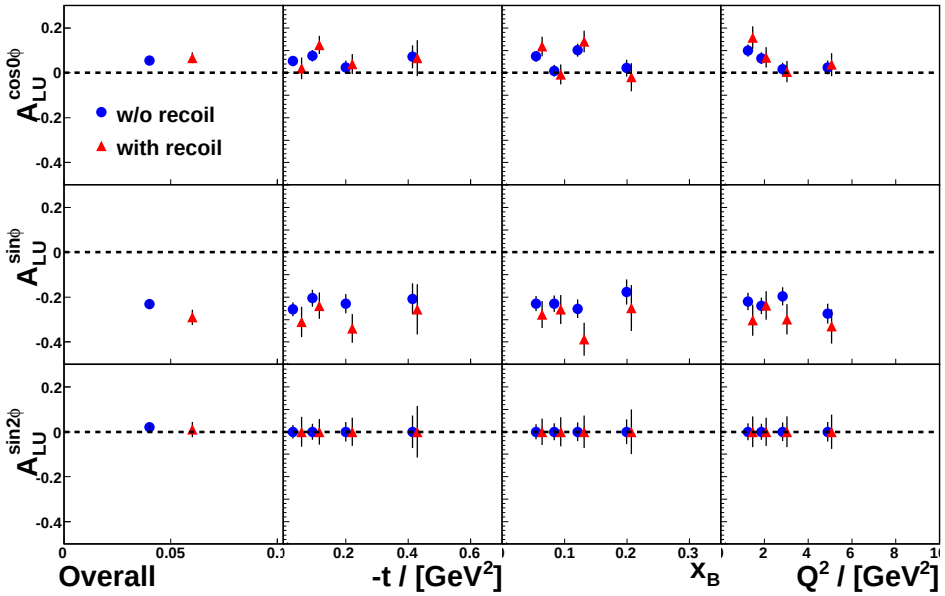

Figure 6.29: The distributions of the asymmetry amplitudes extracted by only the forward spectrometer (solid circles) and with the Recoil Detector (triangles) versus the kinematic variables -t, x_B, and Q^2. The t is the constrained t from the forward spectrometer. The error bars represent the statistical uncertainties. The two sets of points are slightly shifted in the horizontal axis for clarity.

The t Distribution

One of the important observable from the Recoil Detector is the invariant momentum transfer to the target proton t, which is an essential quantity to understand the composition of the nucleon spin as the Ji relation is only valid when t is close to zero [23]. The t resolution measured from the forward spectrometer is not so good in the low t region, hence a high resolution of the t measurement is one of the important designed purposes of the Recoil Detector [27]. Fig. 6.28 shows the distributions (left panel) of the t and its resolutions (right panel). In both distributions, the open triangles represent the results from the constraint t_c measured from the forward spectrometer and the solid boxes indicate the results measured from the Recoil Detector. The small bump in the -t_{rd} indicates the upper limit of the lookup table in the proton hypothesis tracking fitting method, this effect can also be seen the last two points from the resolution distribution. Apart from this small feature, the resolution of the t_{rd} is much better in the small region than the constrained t_c.

The distributions of the BSA amplitudes versus -t, x_B, and Q^2 can be found from Fig. 6.29 and Fig. 6.30. In Fig. 6.29 the asymmetry amplitudes are extracted by the forward spectrometer (solid circles) or with the Recoil Detector (triangles), the t is the constrained t from the forward spectrometer. In Fig. 6.30 the amplitudes are only extracted with the

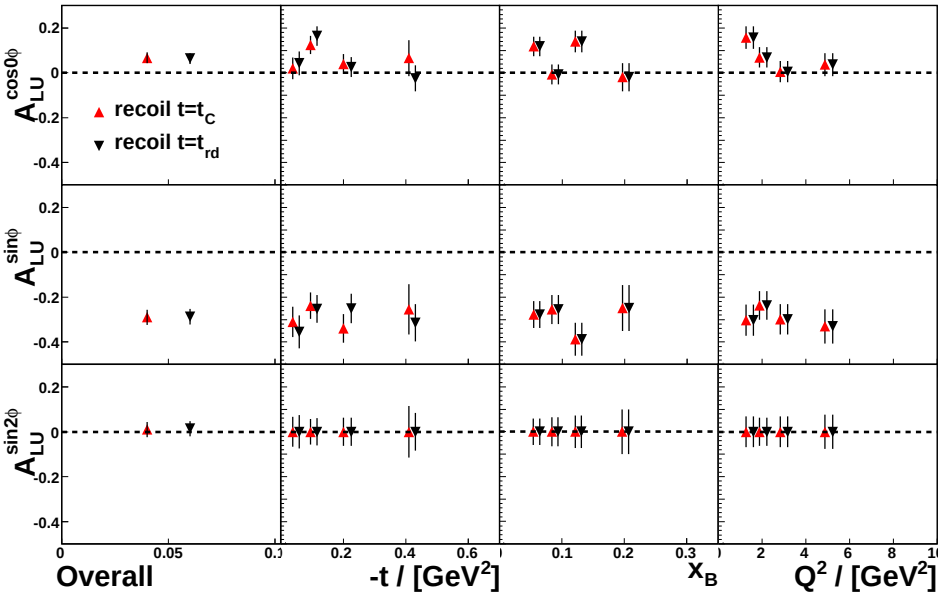

Figure 6.30: The distributions of the asymmetry amplitudes extracted with the Recoil Detector versus the kinematic variables -t, x_B, and Q^2. The t is either the constrained t (triangles) or measured by the Recoil Detector (inverted triangles). The error bars represent the statistical uncertainties. The two sets of points are slightly shifted in the horizontal axis for clarity.

Recoil Detector while the t is either the constrained t (triangles) or measured by the Recoil Detector (inverted triangles).

BSA From Associated BH Process

A precise determination of the asymmetry from the associated BH process will give a consistency check for the asymmetries extracted with the background contamination. The comparison of Fig. 6.26 and Fig. 6.27 may indicate a small or zero asymmetry from the associated process according to the Eq.(6.23). Fig. 6.31 shows the BSA extracted from the associated process as indicated in the previous sections. The solid circles represent the asymmetry amplitudes from the exclusive region in the missing mass squared distributions of the associated BH process while the open triangles indicate the ones from its sideband. The asymmetry from the process with π^- can be found as the open boxes. The open circles were fitted to the function $a_0 + a_1 \sin(\phi) + a_2 \sin(2\phi)$ both by the ML and χ^2 fitting methods. The fitting results can be found in Table 6.3. The big uncertainties appearing here are limited by the low statistics. These results may indicate a small asymmetry of the leading term from the associated BH process. Unfortunately no firm conclusions can

be reached here because of the limitation by the low statistics.

Table 6.3: The amplitudes of the BSA from the associated BH process.

	a0	a1	a2
$\chi^2 fitting$	0.105± 0.069	0.023 ± 0.094	-0.131 ± 0.096
ML fitting	0.090± 0.067	0.025 ± 0.093	-0.145 ± 0.096

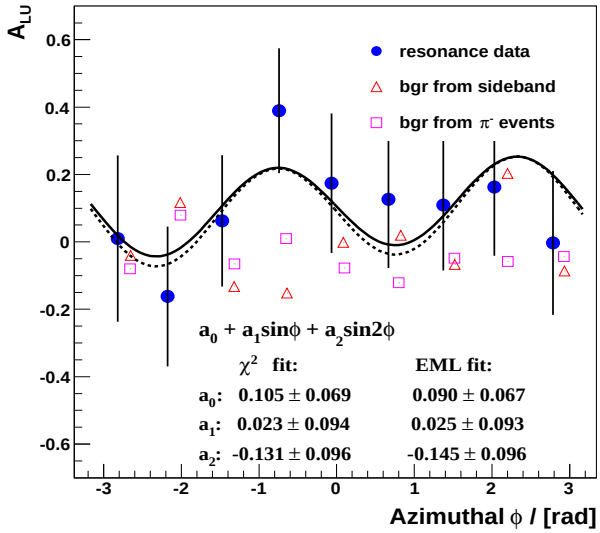

Figure 6.31: The BSA (circles) amplitudes from the exclusive region in the missing mass squared distributions of Δ^+ while the open triangles indicate the ones from its sideband and the open boxes indicate the asymmetry from the processes only with π^- in the Recoil Detector. The statistical uncertainties are indicated by the length of the error bars. The data points were fitted to the function $a_0 + a_1 \sin(\phi) + a_2 \sin(2\phi)$ both by the ML and χ^2 fitting methods.

6.6 Perspective of the Recoil Analysis

It is noted that the statistical uncertainties increase around 70 % from Table 6.1 to Table 6.2, which indicates a corresponding falling-off of the collected statistics. So far, all the cuts used for the recoil data sticked to the traditional way, where the cuts were tuned only according to the forward spectrometer. This allowed us to compare directly the data with and without using the Recoil Detector. However, there is room to tune and even

release some of these cuts for the recoil data to increase the statistics. Fig. 6.32 shows the missing mass distributions of the elastic BH/DVCS process from the events containing a recoil proton. The solid circles represent the distribution by using the standard DVCS cuts, while the dashed line indicates the additional events obtained by releasing the photon geometry cut, the pre-shower requirement of the photon, and the $\theta_{\gamma\gamma^*}$ cut. The sum of both distributions is represented by the solid line.

The releasing of the three cuts without requiring the Recoil Detector certainly would deteriorate the resolution of the missing mass squared distribution and enhance the background. While by requiring the recoil proton, we increase the statistics and keep the background in a low level as can be seen from the figure. Hence the deterioration of the resolution should not be an issue here. However, this is rather a quick look to check the possibility to increase the statistics. Careful studies will be carried out with the help of the MC simulation to finally determine the proper cuts, without effecting the extracted asymmetries.

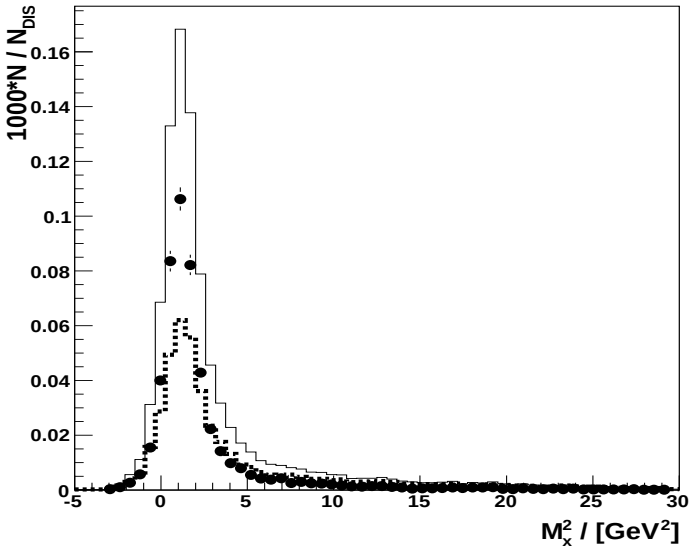

Figure 6.32: The missing mass squared distributions of the events with single recoil proton. The solid circles represent the distribution by using the standard DVCS cuts, while the dashed line illustrates the additional statistics obtained by releasing the photon geometry cut, the pre-shower requirement of the photon, and the $\theta_{\gamma\gamma^*}$ cut. The sum of the both distributions is indicated by the solid line.

The determination of systematic uncertainties is essential to the experimental measurement, and has not yet been addressed. At HERMES, this uncertainty was extracted by the MC simulation for the DVCS studies. With regard to the forward spectrometer, the

possible sources of the systematic uncertainties are the shift of the missing mass squared distributions, the alignment of the detectors and beam positions, the acceptance and smearing of the detectors. The background correction of the semi-inclusive DIS processes and the finite bin width in the certain kinematic may make the further contributions to the uncertainties. Previous studies have revealed that the overall systematic uncertainty arising from these sources to the leading BSA amplitude is around 10 % [26, 53, 96].

The usage of the Recoil Detector will certainly bring additional sources to the systematic uncertainties. For example, the detector efficiencies and the alignment of the detectors are possible candidates. Meanwhile, contributions of some of sources from the forward spectrometer may be reduced by using the Recoil Detector. However, these effects have to be determined from the finalized MC simulations with a full understanding of the detectors, including their efficiencies and the performance of the reconstruction methods.

Chapter 7

Conclusions

HERMES is the experiment using the 27.6 GeV lepton beam from the HERA storage ring to study nucleon spin structure. With its unique technique of internal unpolarized/polarized gas targets and the high polarization of the HERA lepton beam, the HERMES experiment plays a very important role in the nucleon spin community through the studies of inclusive and semi-inclusive DIS processes, and the hard exclusive processes with real photons or mesons in the final state.

The Generalized Parton Distributions (GPDs) can be studied through hard exclusive processes at HERMES. The GPDs describe the nucleon structure at a general level treating both the PDFs and Form Factors as its limited cases. Furthermore, the GPDs were found by the Ji relation to provide access to the total angular momenta of quarks. The Deeply Virtual Compton Scattering (DVCS) is one of the most promising exclusive processes to study GPDs. At HERMES the DVCS is studied via the experimental measurements of the different azimuthal cross-section asymmetries of the DVCS and Bethe-Heitler (BH) processes. Different azimuthal asymmetries have been measured with respect to the beam helicity, beam charge, and the target polarization by the HERMES spectrometer, which is a traditional forward detector system.

Due to the limited acceptance, the recoil protons from the BH/DVCS processes can not be directly detected by the forward spectrometer. Hence the missing mass method was originally used by HERMES to study DVCS. However it is limited by the kinematic resolutions and the capability to clean the backgrounds.

A Recoil Detector was built and installed at the beginning of 2006 to upgrade the HERMES spectrometer. The Recoil Detector consists of three main sub-detectors: a silicon strip detector surrounding the target cell inside the beam vacuum in a scattering chamber, a scintillating fibre tracker (SFT) and a photon detector consisting of three layers of tungsten and scintillator bars. The Recoil Detector extends the acceptance of the spectrometer to the exclusive region by directly measuring the recoil protons and thus minimizes the backgrounds. In addition, it also improves the resolution of the kinematics of the recoil proton, especially in the low momentum region which is essential to study the

Ji relation. Taking advantage of the high luminosity runs from HERA in 2006 and 2007, a large amount of data has been taken with the Recoil Detector with unpolarized proton and deuteron targets.

The SFT is the key component of the Recoil Detector, which has been successfully commissioned from the online data taking to the offline data preparation for the physics analysis. Data calibrations, detector alignments, and sophisticated offline software algorithms have been performed to cope with data including the cross talk corrections and the formulations of the clusters and spacepoints. The particle identification has also been developed and implemented into the data productions.

Together with all the sub-components of the Recoil Detector, significant developments have been achieved to polish the data. The understanding of the detector and the data production are in a good shape. However, some issues still need to be finalized for the physics analysis, such as the fully understanding of the data-MC comparisons, the finalization of the recoil tracking, and the final calibrations of the detectors.

The most advanced data production - the 07c1 μDST production has been used in this work. By using the Recoil Detector the ratio of the background to signal decreased dramatically and reached a level of 3% from the exclusive region in the missing mass squared distribution. Beam-Helicity Asymmetries from the elastic BH/DVCS process have been extracted with and without using the information provided by the Recoil Detector. The leading BSA amplitude extracted without using the Recoil Detector is consistent with the HERMES published BSA result. The corresponding amplitude extracted with the detected recoil proton indicates to be larger than the previous one, however, the difference is still inside the statistical uncertainty. The BSA from the associated BH process has also been extracted with a detected π^+ which is assumed to be the decay product from the Δ^+ resonance via the channel: $\Delta^+ \rightarrow n\pi^+$. Due to the low statistics, the extracted BSA amplitudes from this process have very large statistical uncertainties. However, inside the uncertainties the result indicates that the BSA from the associated BH process is smaller than that from the elastic process.

To conclude, the finalized data will soon be provided by the recoil group. With the help of this unique set of data, HERMES will provide new insights to understand the DVCS and the GPDs.

Bibliography

[1] D. H. Perkins, Introduction to High Energy Physics, 4th edition, (Cambridg University Press, 2000).

[2] B. Povh *et al.*, Teilchen und Kerne: eine Einführung in die physikalischen Konzepte, 6.Auflage, Springer Verlag, 2008.

[3] K.Ackerstaff *et al.*, (HERMES Collaboration), *Nucl. Instr. and Meth. A* **417** (1998) 230, hep-ex/9806008.

[4] M. Dueren, The HERMES Experiment: From the Design to the First Results, Habiliation Thesis, Universität Erlangen, 1995.

[5] J. Ashman *et al.*, (EMC Collaboration), *Phys. Lett. B* **206** (1988), 364.

[6] E. Leader and M. Anselmino, *Z. Phys. C* **41** (1988), 239.

[7] R. L. Jaffe and A. Manohar, *Nucl. Phys. B* **337**, 509 (1990).

[8] R. L. Jaffe, *Phil. Trans. Roy, Soc. Lond. A* **359**, 391 (2001), hep-ph/0008038.

[9] B. Filippone and X. Ji, *Adv. Nucl. Phys.* **26** 1 (2001), hep-ph/0101224.

[10] M. Burkardt, A. Miller and W-D. Nowak, arXiv:0812.2208v2 [hep-ph].

[11] K. Ackerstaff *et al.*, (HERMES Collaboration), *Phys. Lett. B* **404**, (1997) 383-389, hep-ex/9703005.

[12] A. Airapetian *et al.*, (HERMES Collaboration), *Phys. Lett. B* **442** (1998) 484-492, hep-ex/9807015.

[13] K. Ackerstaff *et al.*, (HERMES Collaboration), *Phys. Lett. B* **444**, (1998) 531-538, hep-ex/9809015.

[14] K. Ackerstaff *et al.*, (HERMES Collaboration), *Phys. Lett. B* **464**, (1999) 123-134, hep-ex/9906035.

[15] A. Airapetian *et al.*, (HERMES Collaboration), *Phys. Rev. Lett.* **84** (2000) 2584-2588, hep-ex/9907020.

[16] A. Airapetian *et al.*, (HERMES Collaboration), *Phys. Lett. B* **494** (2000) 1-8, hep-ex/0008037.

[17] A. Airapetian *et al.*, (HERMES Collaboration), *EPJ C* **26** (2003) 527-538, hep-ex/0210047.

[18] A. Airapetian *et al.*, (HERMES Collaboration), *Phys. Rev. Lett.* **90** (2003) 092002, hep-ex/0209018.

[19] A. Airapetian *et al.*, (HERMES Collaboration), *Phys. Rev. Lett.* **92** (2004) 012005, hep-ex/0307064.

[20] A. Airapetian *et al.*, (HERMES Collaboration), *Phys. Rev. D* **71** (2005) 012003, hep-ex/0407032.

[21] K. Rith, *Progress in Particle and Nuclear Physics* **49** (2002) 245

[22] A. Airapetian *et al.*, (HERMES Collaboration), *Phys. Rev. D* **75** (2006) 012007, hep-ex/0609039.

[23] X. Ji, *Phys. Rev. Lett.* **78**, (1997) 610; *Phys. Rev. D* **55**, (1997) 7114.

[24] A. Airapetian *et al.*, (HERMES Collaboration), *Phys. Rev. Lett.* **87**, 182001 (2001), hep-ex/0106068.

[25] A. Airapetian *et al.*, (HERMES Collaboration), *Phys. Rev. D.* **75**, 011103 (2007), hep-ex/0605108.

[26] A. Airapetian *et al.*, (HERMES Collaboration), *JHEP* **06** (2008) 066., hep-ex/0802.2499

[27] HERMES Collaboration, The HERMES Recoil Detector TDR, PRC **01-017**, April 2001.

[28] W. Yu (for the HERMES collaboration), Proceedings of the 4th International Conference on Quarks and Nuclear Physics (QNP06), Madrid, Spain, Jun 5 - 10, 2006.

[29] W. Yu (for the HERMES collaboration), Proceedings of the 14th International QCD Conference (QCD 2008), Montpellier, France, Jul 7 - 12, 2008.

[30] A. V. Radyushkin, *Phys. Rev. D* **56** (1997) 5524, hep-ph/9704207.

[31] X. Ji, *J. Phys. G.* **24**, (1998) 1181, hep-ph/9807358.

[32] K. Goeke, M. V. Polyakov and M. Vanderhaegen, *Prog. Part. Nucl. Phys.* **47** (2001) 401, hep-ph/0106012.

[33] M. Diehl, *Phys. Rept.* **388** (2003) 41, hep-ph/0307382.

[34] A. V. Belitsky, and A. V. Radyushkin, *Phys. Rept.* **418** (2005) 1, hep-ph/0504030.

[35] Collins J. C., L. L. Frankfurt, and M. Strikman, *Phys. Rev. D* **56** (1997) 2982, hep-ph/9611433.

[36] A. V. Radyushkin, *Phys. Rev. D* **58** (1998) 114008, hep-ph/9803316.

[37] Collins J. C. and A. Freund, *Phys. Rev. D* **59** (1999) 074009, hep-ph/9801262.

[38] X. Ji and J. Osborne, *Phys. Rev. D* **58** (1998) 094018, hep-ph/9801260.

[39] X.-D. Ji, W. Melnitchouk, and X. Song, *Phys. Rev. D* **56**, 5511 (1997), hep-ph/9702379.

[40] V. Y. Petrov *et al.*, *Phys. Rev. D* **57**, 4325 (1998), hep-ph/9710270.

[41] S. Scopetta and V. Vento, *Eur. Phys. J.* **A16**, 527 (2003), hep-ph/0201265.

[42] P. Hägler *et al.*, (LHPC and SESAM Collaborations), *Phys. Rev. D* **68**, 0304505 (2003), hep-lat/0304018.

[43] M. Göckeler *et al.*, (QCDSF Collaboration), *Phys. Rev. Lett.* **92**, 042002 (2004), hep-ph/0304249.

[44] M. Vanderhaeghen, P. A. M. Guichon, and M. Guidal, *Phys. Rev. D* **60**, 094017 (1999), hep-ph/9905372.

[45] N. Kivel, M. V. Polyakov, and M. Vanderhaeghen, *Phys. Rev. D* **63**, 114014 (2001), hep-ph/0012136.

[46] A. V. Radyushkin, *Phys. Lett. B* **380**, 417 (1996), hep-ph/9604317.

[47] A. V. Radyushkin, *Phys. Rev. D* **59**, 014030 (1999), hep-ph/9805342.

[48] A. V. Radyushkin, *Phys. Lett. B* **449**, 81 (1999), hep-ph/9810466.

[49] A. V. Radyushkin, hep-ph/0101225.

[50] M. V. Polyakov and C. Weiss, *Phys. Rev. D* **60** (1999) 114017, hep-ph/9902451.

[51] A. V. Belitsky, D. Müller, and A. Kirchner, *Nucl. Phys. B* **629**, 323 (2002), hep-ph/0112108.

[52] S. Stepanyan *et al.*, (CLAS Collaboration), *Phys. Rev. Lett.* **87**, 182002 (2001), hep-ex/0107043.

[53] Z. Ye, Transverse Target-Spin Asymmetry Associated with Deeply Virtual Compton Scattering on the Proton and A Resulting Model-Dependent Constraint on the Total Angular Momentum of Quarks in the Nucleon, Ph.D Thesis, Universität Hamburg, 2006.

[54] A. A. Sokolov and I. M. Ternov, *Sov. Phys. Doklady* **8** (1964) 1203.

[55] M. Beckmann *et al.*, *Nucl. Instr. and Meth. A* **479** (2002) 334.

[56] W. Wander, Rekonstruktion hochenergetischer Streuereignisse im HERMES Experiment, Ph.D Thesis, Universität Erlangen, 1996.

[57] E. C. Aschenauer *et al.*, *Nucl. Instr. and Meth. A* **440** (2000) 338.

[58] N. Akopov *et al.*, *Nucl. Instr. and Meth. A* **479** (2002) 511.

[59] R. Kaiser, Particle identification at HERMES, HERMES internal report **97-025** (1997).

[60] H. Avakian *et al.*, *Nucl. Instr. and Meth. A* **417** (1998) 69.

[61] B. Krauss, Deeply Virtual Compton Scattering and the HERMES-Recoil-Detector, Ph.D Thesis, Universität Erlangen, 2005.

[62] N. Pickert, Commissioning of the Recoil Silicon Detector for the HERMES Experiment, Ph.D Thesis, Universität Erlangen, 2008.

[63] C. Vogel, Kalibration von Siliziumdetektoren für den HERMES Rückstoßdetektor, Ph.D Thesis, Universität Erlangen, 2008.

[64] M. Hoek *et al.*, Performance of the Recoil Scintillating Fibre Tracker in a Test Beam at GSI, HERMES Internal Note, **05-013**, 2005.

[65] L. Rubáček, Search for the Pentaquark States in Lepton-Nucleon Scattering at HERMES, Ph.D Thesis, Universität Gießen, 2006.

[66] M. Hoek, Design and Construction of a Scintillating Fibre Tracker for Measuring Hard Exclusive Reactions at HERMES, Ph.D thesis, Universitäte Gießen, 2006.

[67] T. Keri, Detection of Exclusive Reactions in the HERMES Recoil Fiber Tracker, Ph.D Thesis, Universität Gießen, 2008.

[68] Catalogue, Kuraray, www.kuraray.co.jp/en/.

[69] M. Hartig, The TDC readout of the 12th dynode for the SciFi PMTs, HERMES Internal Note, **04-066**, 2004.

[70] Y. van Haarlem, The HERMES recoil photon-detector and nuclear p_t broadening at HERMES, Ph.D thesis, Universiteit Gent, 2007.

[71] A. Vandenbroucke, Exclusive π^0 productie in HERMES (Detectie-Simulatie-Analyse), Ph.D thesis, Universiteit Gent, 2006.

[72] S. Lu, The PMTs calibration for SFT of the recoil detector at HERMES, HERMES Internal Note **02-018**, 2005.

[73] E. Bellamy *et al.*, *Nucl. Instr. and Meth. A* **339** (1994) 468.

[74] I. Chirikov-Zorin *et al.*, *Nucl. Instr. and Meth. A* **456** (2001) 310.

[75] R.K.Bock *et al.*, The Particle Detector BriefBook, Springer Verlag Berlin Heidelberg New York, 1998.

[76] M. Barker *et al.*, MINOS Internal Note NuMi-L-682, October 2000.

[77] J. Stewart, Background measurements, recoil-commissioning@hermes.desy.de, 21. Jun 07.

[78] T. Keri, Special recoil noise measurement with trigger 29, recoil-commissioning@hermes.desy.de, 24. Jun 07.

[79] W. R. Leo, Techniques for Nuclear and Particle Physics Experiments, Second Revised Edition, Springer-Verlag, 1994.

[80] W.-M. Yao *et al.*, *J. Phys. G* **33**, 1 (2006).

[81] R. Perez. Benito, *in preparation*, Ph.D Thesis, Universität Gießen, 2009.

[82] J. Wendland, Polarized Parton Distributions Measured At The HERMES Experiment, Ph.D Thesis, Simon Fraser University, 1999.

[83] G. Cowan, Statistical Data Analysis, Clarendon Press· Oxford, 1998.

[84] W. Sommer, Identifikation von Pionen und Protonen mit einem Detektor aus szintillierenden Fasern, Diploma Thesis, Universität Gießen, 2003.

[85] X. Lu, *in preparation*, Master Thesis, Universität Hamburg, 2009.

[86] J. Stewart (for the HERMES collaboration), Proceedings of the Nuclear Science Symposium and Medical Imaging Conference, Honolulu, Hawaii, October 2007.

[87] HERMES website, www-hermes.desy.de.

[88] E. Avetissian, dvcs-list@hermes.desy.de.

[89] L. W. Mo and Y. S. Tsai, *Rev. Mod. Phys.* **41** (1969) 205.

[90] F. W. Brasse *et al.*, *Nucl. Phys. B***110** (1976) 413.

[91] D. Drechsel *et al.*, *Nucl. Phys. A***645** (1999) 145.

[92] G. Ingelman, A. Edin, and J. Rathsman, *Comput. Phys. Commun.* **101** (1997) 108.

[93] B. Andersson *et al.*, *Phys. Rept.* **97** (1983) 31.

[94] S. Yaschenko, Private Communication, July, 2008.

[95] A. Mussgiller (for the HERMES collaboration), Proceedings of the 17th International Workshop on Vertex detectors, Utö Island, Sweden, July 2008.

[96] H. Ye, Deeply Virtual Compton Scattering on the HERMES Nuclear Targets, Ph.D Thesis (in Chinese), Peking University, 2008.

List of Tables

List of Figures

Acknowledgements

This work could not have been finished without the help from many people. These acknowledgements are certainly far from enough to express my gratitude.

First of all, I would like to express my sincerest gratitude to my supervisor Prof. Dr. Michael Düren for providing me the opportunity to do the Ph.D in his group. He is such a great person and I have learned quite a lot from his profound thoughts on research and his way of understanding physics. He is always kind and generous and has given me freedom and various support to finish this work both in the 'Hamburg and Gießen periods'.

I'm very indebted to Avetik Airapetian who came to the group in the second half of my Ph.D and shares the office with me. As a senior person, he is never tired of answering my endless questions on the HERMES experiment and spin physics. As an officemate I enjoy pretty much his anecdotes about the experiments. I would like to also thank another senior person Björn Seitz for helping me understand the Recoil Detector in the early days of my Ph.D.

Many thanks go to the former members of the group, Matthias Hoek, Shaojun Lu, Tibor Keri, Lukas Rubáček, and Markus Ehrenfried of the discussions and instructions on our detector. To Roberto Perez, with whom I experienced the hard and happy time during the commissioning of the detector. I learned a lot how to deal with the hard work in a calm way from him. All the other members from the group have to be mentioned for their great help, especially our two secretaries, Marianne Brunotte and Anita Rühl.

I would like to thank all the colleagues in the HERMES experiment in Hamburg. Together with you, we have done such an interesting experiment which was a great time in my life. Especially I wish to thank the colleagues from the recoil group, Andreas Mussgiller, Sergey Yaschenko, Inti Lehmman, Caroline Riedl, Charlotte Van Hulse, Dietmar Zeiler and others for the numerous discussions in the recoil meetings almost every week over the last four years.

Also thanks to Elke Aschenauer and Jim Stewart for their great support to my work.

I am thankful to the Chinese colleagues Zhengyu Ye, Hongxue Ye, and Xianguo Lu for the discussions and companionship in Hamburg, especially to Hongxue, who helped me a lot with the DVCS analysis.

I would like to thank Gunnar Schnell for all the friendly and enlightening discussions and the proof reading of my German abstract.

I want to thank my girl friend Haiyan Ding for her love and support, and to my parents for all that they have given to me.